

Swelling/shrinking ability of adsorbed PNIPAM microgels: hydrophobicity, solvent quality and surface coating

vorgelegt von
Diplom-Chemiker
Marcel Richter
geb. in Stendal

Von der Fakultät II - Mathematik und Naturwissenschaften
der Technischen Universität Berlin
zur Erlangung des akademischen Grades
Doktor der Naturwissenschaften
Dr.rer.nat.

genehmigte Dissertation

Promotionsausschuss:

Vorsitzender: Prof. Dr. rer. nat. Peter Strasser

Gutachter: Prof. Dr. rer. nat. Regine von Klitzing

Gutachter: Prof. Dr. rer. nat. Alexander Böker

Tag der wissenschaftlichen Aussprache: 19.12.2014

Berlin 2015

Acknowledgement

First of all, I thank Prof. Regine von Klitzing for giving me the opportunity working on such an interesting field of research. The friendly support and discussions were always helpful, which led to interesting ideas. She also motivated me to go on when experiments failed.

I want to thank Dr. Anna Burmistrova. She introduced me to AFM measurements and helped me a lot in the beginning of my PhD thesis with fruitful discussions and support.

Dr. Cagri Üzümlü is acknowledged for helping me with the force measurements and the data treatment. Without his help I would still be working on this topic.

A special thank goes to Dr. Yuriy Zakrevskyy. The corporation was outstanding. The work, discussion and measurements were always interesting and effectual.

Dr. Kornelia Gawlitza and Gabi Hedicke were the good souls in the lab. They have always a smile on their face and so do I. This is very important to have such persons in the lab. Dr. Stefan Wellert is thank for his support in the field of DLS measurements and nice discussions.

Michael Eisele is kindly acknowledged. He is a dream for every Phd student. I thank Melanie Hunnenmörder for being a very good and ambitious bachelor student.

I want to thank my former and current lab mates in the Stranski-Lab. Especially, Carolin Ganas, Andreas Klee and Sven Riemer are acknowledged, which became very good fiends.

I want to thank my family and friends for supporting me during the studies and the PhD. I am sure it was not easy with me during this time, but thanks for the support. Especially to my **mom**.

This thesis was supported by DFG via SPP 1259 "Intelligente Hydrogels".

Contents

1	Introduction	2
2	Scientific background	6
2.1	Theory: Microgels	6
2.2	Smart materials on solid surfaces	8
2.2.1	Microgel adsorption at an interface	9
2.2.2	Thermo-responsive microgel behaviour	10
2.2.3	Ionic strength and pH depending behaviour of microgel	11
2.2.4	Co-non-solvency behaviour of microgels	11
2.2.5	Mechanical behaviour of microgels	13
2.2.6	Microgel behaviour depending on surface coatings . . .	13
2.2.7	Applications of PNIPAM particles	14
3	Methods	17
3.1	Atomic force microscopy (AFM)	17
3.1.1	AFM imaging process	17
3.1.2	AFM force measurement process	18
3.2	Dynamic light scattering (DLS)	21
3.3	Zeta potential measurements	23
3.4	Ellipsometry	24
3.5	Contact angle measurements	26
4	Experimental section	27
4.1	Materials	27
4.2	Microgel synthesis	27
4.3	DLS experiments	28
4.4	Sample preparation	29
4.5	Preparation of the polyelectrolyte multilayer	29
4.6	AFM experiments	30
4.7	Contact angle measurements	31

5	Mechanical properties of microgels	32
5.1	Introduction	32
5.2	PNIPAM based microgels	33
5.2.1	Results	33
5.2.2	Discussion	39
5.2.3	Conclusions	43
5.3	Polyethyleneglycol (PEG) based microgels	44
5.3.1	Results	44
5.3.2	Discussion	48
5.3.3	Conclusion	49
5.4	Polyglycerol (PG) based microgels	50
5.4.1	Results	50
5.4.2	Discussion	51
5.4.3	Conclusion	52
5.5	Outlook	52
6	Co-non-solvency effect of PNIPAM microgels	54
6.1	Introduction	54
6.2	Results	55
6.2.1	Co-non-solvency effect of microgel particles in bulk	55
6.2.2	Co-non-solvency of adsorbed PNIPAM microgels	57
6.2.3	Spin coating conditions on particle deswelling	61
6.2.4	Adsorbed microgel particles in ambient conditions	64
6.2.5	Swelling ability of adsorbed PNIPAM based microgels	67
6.3	Discussion	68
6.4	Conclusion	73
6.5	Outlook	74
7	The Influence of different layer systems on the particle behaviour	75
7.1	Introduction	75
7.2	Results	76
7.2.1	Layer characterisation	76
7.2.2	Thermo-responsive particle behaviour on surface coatings	77
7.2.3	Effect of polyelectrolyte multilayers of different thickness	78
7.2.4	Particle behaviour at ambient conditions	80
7.3	Discussion	82
7.3.1	Properties of different single layer coatings	82
7.3.2	Particle behaviour at different single layer coatings	83

7.3.3	Particle behaviour on multilayers	85
7.4	Conclusion	86
7.5	Outlook	87
8	Interaction between microgels and azobenzene surfactant	88
8.1	Introduction	88
8.2	Microgel/surfactant complex in pure water	89
8.2.1	Formation of the microgel/surfactant complex	89
8.2.2	Light induced particle collapse	93
8.2.3	Influence of co-monomer concentration	94
8.3	Microgel/surfactant complex in different buffer solutions	96
8.3.1	Phase diagram of AAA-50 particles in buffer solutions	96
8.3.2	Contraction process in buffer solution	97
8.4	Conclusion	99
8.5	Outlook	100
9	<i>In situ</i> particle degradation of PG-based microgels by AFM	101
9.1	Introduction	101
9.2	Results	103
9.2.1	Microgel degradation at the surface	103
9.2.2	Force measurements during particle degradation	105
9.2.3	Real time particle degradation via constant force mode	105
9.3	Discussion	106
9.4	Conclusion	108
9.5	Outlook	108
10	Conclusion and Outlook	110
10.1	Conclusion	110
10.2	Outlook	113
11	Appendix	116

Chapter 1

Introduction

Today, plastics play a crucial role in daily life. Whether in automotive industry or in packaging, such materials gain much attention due to their unique properties. One of the most interesting kind of polymers are gels^{1,2}. These three-dimensional cross-linked networks show excellent swelling behaviour in a suitable solvent as well as viscoelastic properties³⁻⁶. Microgels in particular have been in the focus of recent research^{1,7,8}. Compared to macrogels, the small size of microgels, which is in the submicron range (10 nm-1 μ m), ensure a fast response to changes in the environment.

One of the most investigated microgel is based on *N*-isopropylacrylamide (NIPAM) with its lower critical solution temperature (LCST), which is also often called volume phase transition temperature (VPTT), at 32 °C⁹⁻¹¹. Below this VPTT hydrogen bonds are favoured between the polymer network and the solvent, which leads to a swollen particle. With an increase in the temperature, the hydrogen bonds between the polymer network and the solvent break up and hydrophobic polymer-polymer interactions become dominant resulting in a shrunken particle. The ability to manipulate the particle size by an external trigger makes microgels based on PNIPAM interesting for application such as drug delivery, micro lenses, ion exchange, coatings and sensors¹²⁻²³. Size manipulation of such PNIPAM particles can not only be induced by changes in the temperature but also by further external parameters such as ionic strength, pH, light and magnetic field²⁴⁻²⁹. Since PNIPAM does not exhibit a pH responsive behaviour, co-monomers, such as acrylic acid, allyl acetic acid or methacrylic acid, can be incorporated into the polymer network to make the microgel pH responsive^{25,30-34}.

All these above mentioned studies have been mainly performed in bulk. However, the properties of PNIPAM based particles show tremendous difference between bulk particles and their adsorbed counterparts³⁵. This fact

necessitates intensive investigations for adsorbed microgels. Another important aspect for studies at an interface is the investigation of single adsorbed particles. While in bulk, only the behaviour of many microgels can be studied by e.g. dynamic light scattering (DLS) or small angle neutron scattering (SANS), surface methods such as atomic force microscopy (AFM) are able to study the behaviour of single adsorbed particles. Especially, application such as drug delivery and biological sensor applications in particular require a consolidated knowledge about the microgel properties, e.g. swelling/shrinking behaviour, at surfaces.

This PhD thesis provides detailed information about the microgel behaviour depending on various internal and external parameters. Internal parameters, such as cross-linker density or co-monomer content, will be adjusted during the microgel synthesis leading to a fixed particle behaviour, e.g. particle stiffness. The determination of particle elasticity with different cross-linker and co-monomer content was part and parcel of several publications³⁵⁻³⁷. The open question is in which way the elasticity changes with a variation of the co-monomer in terms of their hydrophobicity. Chapter 5 focuses on this open question. Here, PNIPAM particles with the co-monomers acrylic acid and the long-chained allyl acetic acid were compared in terms of their swelling ability and particle stiffness.

Another approach to influence the swelling behaviour of microgels is the solvent quality. There are various publications dealing with the microgel behaviour in different water/organic solvent mixtures, where PNIPAM based microgels show the well-known co-non-solvency effect³⁸⁻⁴². The co-non-solvency effect appears, when a mixture of two "good" solvents, e.g. water and ethanol, is used as a solvent. Such mixtures induce a particle shrinking due to the dehydration of the polymer network. However, the co-non-solvency effect of adsorbed PNIPAM particles is not fully understood so far and has to be clarified⁴³. Chapter 6 provides detailed information about the shrinking/swelling behaviour of PNIPAM particles in different water/organic solvent mixtures. The impact of the different solvent polarities as well as different particle compositions have been investigated.

A third approach to manipulate the shrinking/swelling behaviour of the PNIPAM particles lays in the surface coating itself. Such surface coatings consist of polyelectrolytes and can be build up by the layer-by-layer method, which ensure a gradually increase in the layer thickness⁴⁴. The layer thickness, the chemical nature of the used polyelectrolytes as well as the polyelectrolyte charge impacts the swelling capability of the microgel particles and is part

and parcel of chapter 7. The interplay between the microgel particles and the different layer systems is studied during several heating/cooling cycles.

The experiments of chapter 8 and chapter 9 were performed in cooperation with the Santer group at the University of Potsdam (chapter 8) and the Haag group at the Freie University Berlin (chapter 9). In chapter 8, an approach for new sensor applications is developed due to the formation of microgel/azobenzene complexes. The formation of these complexes based on electrostatic attraction between the negatively charged microgel and the positively charged surfactant. Such microgel/surfactant complexes undergo a light-induced particle collapse due to the switching ability between *trans*- and *cis*-conformation of the surfactant.

In chapter 9, an *in situ* particle degradation via AFM is presented. The particles obtained by the Haag group (Freie University Berlin) are stable in basic conditions and degrade in acid media. A precise study of the degradation process in lateral and vertical dimension is shown. Such degradable particles could garner much attention in drug delivery, due to homogeneous and long-term drug release.

Chapter 2

Scientific background

2.1 Theory: Microgels

Gels consist of a three dimensional polymer network composed of monomer units, which can be connected by different kind of bonds. They can be either physical or chemical nature. Physical bonding can be achieved by electrostatic interaction, van der Waals and H-bonds, while in case of chemical bonds new covalent connections are built⁴⁵. Gels swell in a suitable solvent resulting in an enormous mass increase. Gels are considered as hydrogels if water is used as solvent. In the swollen state, gels show a solid-like and liquid-like character⁹. Thereby, the polymer network represents the solid-like contribution, while the solvent represents the liquid-like contribution. The solid-like character is influenced by various parameters.

On the one hand, the solid-like character can be tuned by the cross-linker content, which refers to the number of chemical connections. Highly cross-linked gels leads to a considerably compact and less flexible network, which results in a reduced swelling ability^{46,47}. Consequently, less cross-linked polymer networks show a stronger swelling. The different cross-linked gels show not only different swelling properties but also differ in their viscoelastic properties.

The polymer network can exhibit a particle size scale of several nanometres up to one micrometre, which refers to a microgel. Larger scale of the polymer network is called a macrogel. One characteristic difference between this two kind of gels is determined by the reaction to external changes. Microgels react fast to changes in the environment, while macrogels require longer times to gain their equilibrium state^{25,29,36}. This PhD thesis focuses on microgels due to their fast reaction to environmental changes, which is essential to improve

or develop applications in the field of sensors and drug delivery.

An improved swelling behaviour is especially observed when charged co-monomers, such as acrylic acid and allyl acetic acid, are introduced into the polymer structure^{25,33,48}. The ionised co-monomers cause repulsive interactions within the polymer network leading to a flexible and highly swollen gel. In the case of neutral charged polymer, no repulsive interaction can occur leading to a less pronounced swelling ability²⁷.

The impact on the gel size by external parameters can be described as "smart" behaviour. Further external parameters, which can influence the gel size are temperature, ionic strength or light irradiation^{28,29,49}.

The best-known microgel, which undergoes a temperature induced volume phase transition (VPT), is based on *N*-isopropylacrylamide with its lower critical solution temperature (LSCT) at 32 °C^{5,50}. Below this temperature H-bonds between the polymer network and the solvent are favoured leading to a highly swollen gel as shown in Figure 2.1. An increase in the temperature leads to a breaking of these H-bonds and as a result from this, water is released from the network. The hydrophobic interactions (polymer-polymer bonds) dominate within the polymer network leading to a microgel collapse.

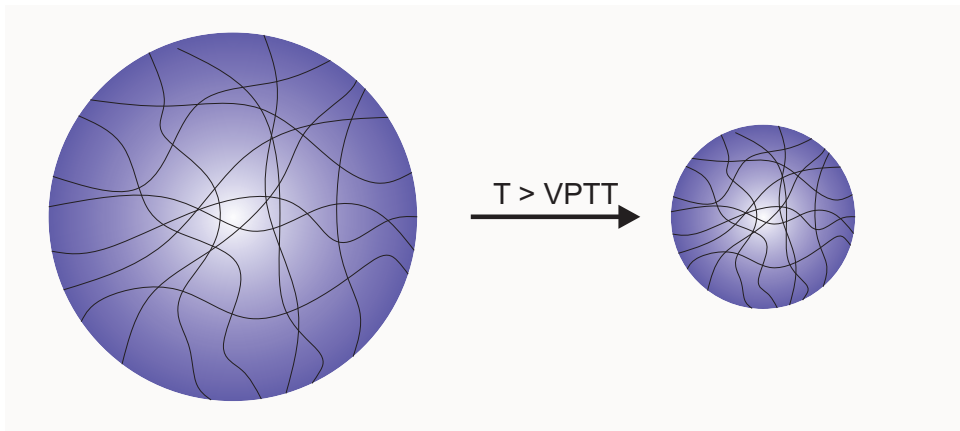


Figure 2.1: Temperature induced volume phase transition of PNIPAM particles.

To understand the VPT of such particles the Flory-Rehner theory has to be considered. The theory assumes that the free energy for the gel F_{gel} is separated into three contributions^{51,52}:

$$F_{gel} = F_{mix} + F_{el} + F_{ion} \quad (2.1)$$

Here, F_{mix} is the free energy of the gel being dissolved, F_{el} is the free energy of the polymer network elasticity and F_{ion} represents the free energy of

microgel charges. Equation 2.1 can be expressed as osmotic pressure in case of a volume change in the system as follows:

$$\Pi_{gel} = - \left(\frac{\partial F}{\partial V} \right)_T = \Pi_{mix} + \Pi_{el} + \Pi_{ion} \quad (2.2)$$

Furthermore, Π_{mix} , Π_{el} and Π_{ion} can be written as:

$$\Pi_{mix} = - \frac{N_A k_B T}{v} (\phi + \ln(1 - \phi) + \chi \phi^2) \quad (2.3)$$

$$\Pi_{el} = - \frac{N_c k_B T}{V_0} \left(\left(\frac{\phi}{2\phi_0} \right) - \left(\frac{\phi}{\phi_0} \right)^{\frac{1}{3}} \right) \quad (2.4)$$

$$\Pi_{ion} = - \frac{f N_c k_B T}{V_0} \frac{\phi}{\phi_0} \quad (2.5)$$

N_c is the Avogadro constant, k_B is the Boltzmann constant, T the temperature, v the molar volume of the used solvent, ϕ the polymer volume fraction, ϕ_0 the polymer volume fraction in initial state, N_c the chain number and f refers to the ions. χ is called the Flory-Huggins parameter and is related to the polymer solvent interactions. The Flory-Huggins parameter is defined as:

$$\chi = - \frac{\Delta F}{k_B T} = \frac{\Delta H - T \Delta S}{k_B T} \quad (2.6)$$

ΔH is the change in enthalpy and ΔS the change in entropy during the VPT. Depending on the values of ΔH and ΔS one can distinguish between lower critical solution temperature (LCST) and upper critical solution temperature (UCST).

A useful parameter for the shrinking quantity of microgels is the deswelling ratio α and can be defined as follows:

$$\alpha = \frac{(V_x)^3}{(V_{initial})^3} \quad (2.7)$$

α is the deswelling ratio, V_x represents the particle volume at a certain temperature and $V_{initial}$ is the particle volume in initial state usually at 20 °C.

2.2 Smart materials on solid surfaces

This chapter contains part of the paper: "Responsive Microgels at Surfaces and Interfaces *Z. Phys. Chem.*, DOI: 10.1515/zpch-2014-0568"

2.2.1 Microgel adsorption at an interface

Due to the "smart" behaviour of poly (*N*-isopropylacrylamide) (PNIPAM) microgels, such materials raise much attention in surface science for example as novel coatings and sensors^{15,16,53}. Such applications require homogeneous, uniform and, defect-free particle coating on the substrate. The particle deposition can be performed by two strategies⁵⁴. The first method can be described as "passive" method, where the particles sediment at the surface. The second method is the "active" method or spin coating, where the particles are deposited via centrifugation. However, the formation of homogeneous monolayers is still a challenging task and the degree of surface coverage depends on several parameters. Schmidt *et al.* used a third deposition method to form homogeneous monolayers. They used the dip coating method for surface coverage of PNIPAM-co-AAc particles (acrylic acid incorporated). It has been shown, that the surface coverage depends on two factors. On the one hand, the used dip coating method is essential for the monolayer formation. Substrates, which have been investigated immediately after the dip coating procedure, feature a closed-packed monolayer. Substrates, which have been washed with water after the dip coating procedure, exhibit a lower surface coverage. It was explained by a weak particle-to-surface interaction, that leads to particle desorption during the washing process. The second crucial factor for a homogeneous monolayer is the pH value of the particle solution. At low pH, where the PNIPAM-co-AAc particles are weakly charged, the particles arrange in high packing density. An increase in the pH leads to a decrease in the packing density. This observation is explained by the increasing repulsion interaction between the individual particles. At high pH, the AAc groups are fully deprotonated, which results in an increase in charge density and electrostatic repulsion between the particles leading to poor surface coverage. At low pH, the particles have a low charge density, due to the protonated AAc groups. This fact favours a particle monolayer. Another approach to form particle monolayers was done by Burmistrova *et al.*⁵⁵. The packing density of the particles can be controlled by the concentration of the particle solution and by the spin coating parameters. High particle concentrations favour the formation of closed-packed particle monolayers. A decrease in the particle concentration results in a lower packing density. At a few 100's of rpm spinning velocity, the particles arrange in a homogeneous monolayer. An increase in the rpm favours a lower packing density or even single adsorbed particles. The reason for a different surface coverage at low and high rpm results from

the competition between the adsorption time and the time, which is needed to centrifuge. At low rpm, the particles have more time to adsorb at the surface, while at high rpm the particles are much wider spread before adsorption.

Non-closed packed monolayer or single adsorbed particles are inappropriate for applications like sensors and coatings and therefore monolayer systems are preferable. However, to neglect interparticle interactions such as electrostatic repulsion, which have an impact on the particle properties, single adsorbed particles are particularly favourable to study the properties of the microgels. In the following, properties of adsorbed particles are described in detail in terms of temperature, ionic strength, pH and solvent quality.

2.2.2 Thermo-responsive microgel behaviour

The properties of adsorbed particles can differ significantly from those in solution. In doing so, the particle composition plays a major role. With increasing the co-monomer content within PNIPAM-co-AAc particles, an increase in the VPTT is observed and at very high co-monomer content two VPTT is determined in the bulk phase^{27,35}. The first VPT results from the collapse of the PNIPAM-rich domains, while the second VPT is attributed to the AAc-rich domains. However, the adsorbed counterparts show only one VPTT³⁵. At the surface, both domains, PNIPAM-rich and AAc-rich, interfere with each other leading to only one VPTT at higher temperatures. Höfl *et al.* observed a similar particle behaviour⁵⁶. They used PNIPAM particles with incorporated vinyl acetate. Such particles exhibit a broad VPTT at the surface. This arises from the inhomogeneity of the particles resulting in a non-uniform particle collapse. Certain applications desire a precise VPTT. This can be achieved by the use of two monomers, which exhibit a large difference in their LCST. Clarke *et al.* synthesised PNIPAM particles containing different amount of *N*-isopropylmethacrylamide (NIPMAM). The VPTT of these PNIPAM-PNIPMAM particles can be adjusted by the PNIPAM-to-PNIPMAM ratio⁵⁷. An increase in the PNIPMAM content leads to an increase in the VPTT, while a higher PNIPAM content leads to a lowering of the VPTT towards 32 °C. Not only the incorporation of co-monomers offers great potential to tune the particle properties but also the cross-linking density of PNIPAM particles plays also a crucial role to tune the particle properties⁵⁸. Particles with lower cross-linker content show a sharp VPT, while higher cross-linked particles have a broader VPT. The authors explained their observation with the inhomogeneity of the particles. Higher cross-linked

particles exhibit an irregular inner structure compared to the lower cross-linked particles. Thus, the particle collapse in a non-uniform fashion leads to a broad VPT. Furthermore, less cross-linked particles show a hysteresis in particle size during heating/cooling cycles³⁶. This hysteresis disappears for higher cross-linked particles. The hysteresis is related to the formation of intraparticle cross-links between the hydrophobic side chains, which are formed during the particle collapse. These extra cross-links remain during the particle reswelling leading to a less pronounced swelling ability and smaller particle size.

2.2.3 Ionic strength and pH depending behaviour of microgel

The above mentioned examples illustrate the modification of the particle itself. In the following, the response of the particles to the change of external parameters such as pH and ionic strength is highlighted. Nerapusri *et al.* used PNIPAM-co-AAc particles to study the responds to changes in the pH⁵⁹. The particles have been adsorbed on a positively charged surface. With increasing the pH, the particles experience a decrease in the size first and reswell at very high pH. This is explained by two counter effects. At intermediate pH, the charge density of the particles increases, due to deprotonation of the AAc groups. The increase in the charge density leads to a stronger attraction between the positively charged surface and the negatively charged particle. Hence, a decrease in the particle size occurs. At very high pH, the AAc groups are fully deprotonated leading to strong repulsive interactions within the particles and an increase in the particle size. The particle size cannot only be manipulated by changing the pH but also by the addition of salt. An increase in the ionic strength leads to screening of both microgel and surface charge. Thus, the electrostatic attraction between the particle and surface is weaker leading to an increase in the particle size.

2.2.4 Co-non-solvency behaviour of microgels

As discussed in the previous section, microgels response to changes of external parameters such as temperature, pH and ionic strength. However, the size manipulation of microgels depends also on the solvent quality. In doing so, such behaviour offers a huge potential in sensor application and has to be studied intensively.

PNIPAM microgels show an excellent swelling property in pure solvents such as water, MeOH or EtOH. However, the swelling ability decreases in

mixtures, which consist of water/organic solvent resulting in microgel shrinking. It means a mixture of two *good* solvents turns into a *poor* solvent for PNIPAM microgels. This phenomenon is called co-non-solvency effect and was first described by Winnik *et al.* in 1990³⁸.

The highly swollen microgels in pure water show a decrease in the microgel size, due to the addition of small quantity organic solvent. At the certain organic solvent content the microgel size reaches a minimum in size. Further increase in the organic solvent content leads to a microgel reswelling.

The co-non-solvency effect can be explained as follows. Water molecules and organic solvent molecules start to interact and an aqueous clathrate structure is formed around the organic solvent molecules⁶⁰. This causes a dehydration of the polymer network and the formation of hydrophobic polymer-polymer interaction is favoured, which leads to a shrinkage of the microgel. At the microgel size minimum most of the water molecules surround the organic solvent molecules. With further increase of the organic solvent content, the water molecules are unable to surround the organic solvent molecules and the clathrate structure breaks up. Consequently, the water as well as the organic solvent molecules interact directly with the polymer network leading to a microgel reswelling. Tanaka *et al.* proposed another model to explain the co-non-solvency effect, the so-called competitive adsorption⁶¹. Here, water and organic solvent molecules compete against each other to form H-bonds with the polymer. The downside of this model is the negligence of solvent-solvent interaction, which are stronger compared to the solvent-polymer interaction⁶².

Since the solvent-solvent interactions play a crucial role in the co-non-solvency behaviour of PNIPAM microgels, the shrinking ability of PNIPAM particles strongly depends on chemical nature of the used organic solvent. An increased hydrophobicity of the organic solvent influences the VPTT of the microgels tremendously, which leads to a decrease in their VPTT^{63–65}. Hydrophobic organic solvents need more water molecules for the hydration, leading to a stronger dehydration of the polymer at lower temperatures.

Even though solvent-solvent interactions might dominate the particle collapse, polymer-solvent interaction should not be neglected for the overall understanding of the shrinking/reswelling process. In fact, it has been shown, that the organic solvent content within the particle is much higher than in the surrounding mixture⁶⁶. THF, for instance, shows a higher binding ability to the polymer than water in an already collapsed particle. This is attributed to the hydrophobicity of both the collapsed particle and the THF. The complexity of the co-non-solvency effect becomes even more evident for adsorbed

PNIPAM particles. PNIPAM particles show a shift in the VPTT minimum from bulk to adsorbed particles towards higher organic solvent content⁴³.

2.2.5 Mechanical behaviour of microgels

Variation of the amount of chemical cross-linker and/or the incorporation of co-monomer into the PNIPAM network also has a direct impact onto the elasticity of the microgels. This can be defined by the stiffness of the particles as shown by Matzelle *et al.*, where AFM measurements were applied to determine the influence of different cross-linker densities in PNIPAM particles⁶⁷. Less cross-linked particles exhibit a lower particle stiffness compared to their higher cross-linked counterparts. An increase in the cross-linker density results in an increasing number of covalent bonds in the particle. Thus, the polymer network becomes less flexible leading to an increase in the particle stiffness. With increasing the temperature, the particles collapse leads to a tremendous increase in the particle stiffness compared to their swollen counterparts at low temperature. Schmidt *et al.* observed a similar mechanical particle behaviour⁶⁸. The particle stiffness increases by the factor of 7 by increasing the temperature above the VPTT. Additionally, the particle stiffness follows the particle shape. The stiffest part of the particle is located in the centre of the particle and decreases towards the particle periphery. To understand this behaviour, one has to consider the particle morphology. The particle can be classified into a higher cross-linked core and the lower cross-linked shell, due to the different consumption of the monomer and cross-linker during the synthesis. This fact results in a stiffer particle core and a softening towards the particle periphery. Briefly, one can say, that particles can be manipulated by the variation of the cross-linker density and the incorporation of co-monomer to obtain suitable properties for applications.

2.2.6 Microgel behaviour depending on surface coatings

The above mention parameters influence the microgel behaviour tremendously. For practical applications, e.g. coatings, however, one has to understand the interplay between the microgel particles and the underlying surface. The complexity is shown in various publications^{55,58,69,70}. Zavgorodnya *et al.* also showed, that the multilayer coverage has a strong impact on the particle properties⁷¹. Here, PNIPAM-co-AAc have been investigated in dependence of different PSS/PAH multilayers, with positively charged PAH as terminated layer, at two different pH values. At the chosen pH values the particles

are neutral and negatively charged. Adsorbed particles, which are neutral charged, exhibit a higher particle height compared to the negatively charged ones. The lateral dimension of the particle was also larger for charged particles as for the neutral ones. This indicates strong microgel-to-surface interactions between the charged particles and the surface, due to electrostatic interaction. The electrostatic attraction between the negatively charged particles and the positively charged surface flatten the particle leading to a large particle width and a small particle height. Islam *et al.* follows another approach⁷². PNIPAM-co-AAc particles have been deposited between two gold layers and the pH was adjusted to obtain neutral and negatively charged particles. This etalon was exposed to different polyelectrolytes solutions (PDADMAC and PSS). The addition of positively charged polyelectrolytes leads to a decrease of the particle height, while negatively charged polyelectrolytes has no influence on particle size. Neutral charged particles show no response to both, positively and negatively charged, polyelectrolytes. This indicates clearly, that the interaction between particles and polyelectrolytes, is of electrostatic nature.

2.2.7 Applications of PNIPAM particles

The ability of the particles to change the properties by small particle modifications offers a multitude of interesting applications^{73–76}.

In case of surface coating, small defects or multilayers of the particles can occur during the formation of the coverage. Such features are undesirable for surface coatings. Quinn *et al.* developed a method to obtain homogeneous and long-range monolayers⁷⁷. A small amount of ethanol was added to the particle solution before preparing the surface coating leading to a separation of the particle solution into small droplets due to the surface tension gradient. This leads to a ordered monolayer of particles during the spin coating process. The fabricated particle monolayers can be damaged by time and have to be repaired or replaced. Lyer *et al.* showed, that the ageing of the coating can be prevented by using a particle solution with a bimodal size distribution. By this approach a particle rearrangement can occur more easily than in a monomodal system, which gives the coating a self-healing feature.⁷⁸

Once a robust and defect-free monolayer is formed, one can develop effective sensors as shown by Carter *et al.*⁷⁹. In this paper, particles have been adsorbed onto a gold surface. Another gold layer has been evaporated on top of the particle monolayer. The particles have been exposed to a water-organic

solvent solution resulting in a particle collapse. The degree of the particle shrinking depends on the thickness of the overlaying gold layer. Thin layers lead to a fast diffusion of organic molecules through the gold and a fast response of the particles, while thicker gold layers leads to a slow response of the particles.

Adjusting the hydrophobicity is another interesting aspect for coatings⁸⁰. The hydrophobicity plays a crucial role for interactions between biological material and the surface⁸¹. Lin *et al.* incorporated polyurethane into the particles⁸². It turns out, that the hydrophilic/hydrophobic balance of the surface can be switched by changing the temperature.

Chapter 3

Methods

This section gives an overview of the used methods in bulk and at the surface. It is a rather short and brief description as a too detailed summary over the methods. A detailed description of each particular method can be found in the denoted literature.

3.1 Atomic force microscopy (AFM)

The method of the atomic force microscopy, which was developed in 1986 by Binnig and co-workers, is a fast and precise surface imaging method⁸³. The AFM applications are manifold. It gives the possibility to study soft as well as hard materials at an interface^{84,85}. With this powerful method, it is even possible to detect differences in the electron density resulting in an image of the chemical structure of an organic structure⁸⁶. Such study requires ultra-vacuum as well as extreme low temperatures.

The AFM setup is depicted in Figure 3.1 and operates as follows: The light source generates a Laser beam, which is focused on the back of the cantilever. From the cantilever the Laser beam goes to a two-dimensional detector. The AFM images will be generated by the cantilever movements. The piezo unit guarantees the precise movements in the x-, y- and z-direction.

3.1.1 AFM imaging process

The sample imaging can be performed in three different modes, the contact, non-contact and intermittent contact mode.

In contact mode, the tip is constantly in contact with the sample and follows the surface height profile. This mode gains the highest sample resolution. Since the tip is in direct contact to the sample, the force, which will be applied

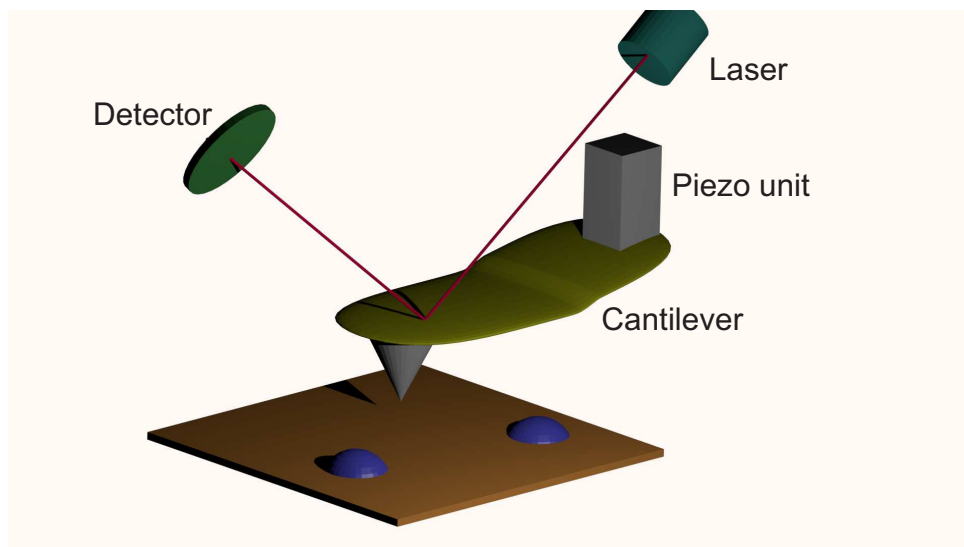


Figure 3.1: Schematic presentation of an AFM setup.

to the sample, is very high and can lead to sample damaging in case of soft matters. Hence, contact mode is usually applied to hard materials.

In non-contact mode, the tip never touches the surface. The cantilever oscillates above the surface at a frequency, which is slightly higher as the resonance frequency of the cantilever. Since there is no contact between the tip and surface, no sample damaging takes place but hence the sample resolution is less convenient.

The intermittent contact mode combines the contact mode with the non-contact mode. This mode unifies a good resolution with a minimum of damage to the sample. The cantilever is excited with a frequency, which is slightly below the resonance frequency of the cantilever. Thus, the cantilever oscillates above the surface and touches the surface at the oscillation minimum. The short tip contact on the surface avoids that damage to the sample occurs. The intermittent contact mode records the change in the amplitude as well as the phase shift of the cantilever. From the amplitude changes the height profile is calculated. The phase shift provides sample information such as mechanical properties and adhesion of sample softness. Further information about the AFM technique can be found elsewhere^{87–89}.

3.1.2 AFM force measurement process

The AFM method provides not only an imaging mode but also a force measurement mode⁸⁹. These measurements can be performed with different types of cantilever. The most common force measurements are done with a col-

loidal probe^{68,90}. But also cantilever with tips or tipless cantilever could be used^{35,36}.

Force measurements were typically performed in contact mode. The cantilever approaches the surface in z-direction. After the probe touches the sample, the penetration of the probe takes place. Due to the cantilever deformation the deflection changes. The penetration of the probe will be executed until a specified deflection is reached. Once this specified deflection was reached the cantilever is retracted to the starting z-position^{89,91}. The described process leads to force curve as shown in Figure 3.2. Such force curve shows the cantilever deflection x against the piezo position Z . To achieve a force-distance curve both parameters have to be transform into force and distance^{89,91}. The force can be achieved by multiplying the cantilever deflection with its spring constant using Hooks law as shown in Equation 3.1:

$$F = -kx \quad (3.1)$$

where k is the spring constant, x represents the cantilever deflection. The tip-sample separation d can be achieved by adding the cantilever deflection x to the piezo position Z , which gives then:

$$d = x + Z \quad (3.2)$$

However, to achieve the precise Force-distance curve the sensitivity of the cantilever has to be determine on a hard, clean surface. The sensitivity of cantilever defines the exact deflection to distance dependence. Furthermore, due to the cantilever sensitivity the spring constant can be determined by the thermal noise method. The result of this procedure is a force-distance curve of the measured sample. The slope of the curves gives an idea of the sample stiffness. A strong increase in the slope usually indicates hard samples (see red curve in Figure 3.2), while soft sample exhibit a less pronounced increase in the slope (see black curve in Figure 3.2).

For the calculation of the correct particle stiffness, the Hertzian model for a spherical cantilever tip is often used as follows:^{87,92,93}.

$$F = \frac{4E\sqrt{R}}{3(1-v^2)} \cdot \delta^{3/2} \quad (3.3)$$

where F is the force on the cantilever, R is the indenter radius, v is the Poisson ratio, E is the Young's Modulus and δ is the indentation depth. This model assumes an infinite film thickness as well as no interactions between the indenter and the sample occurs.

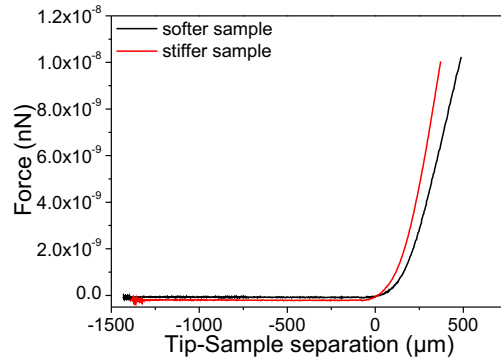


Figure 3.2: Force-distance curves of two sample with differing elasticity.

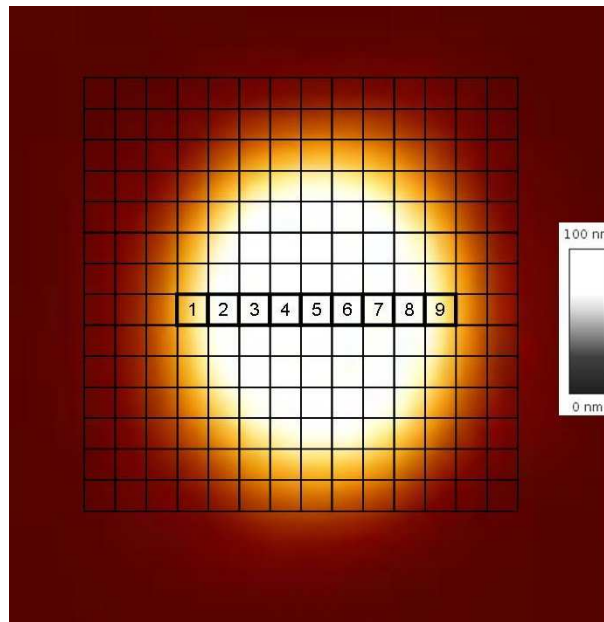


Figure 3.3: Schematic presentation of a force map.

The force curves were recorded using the force mapping tool from the JPK software as shown in Figure 3.3. Every square represents a force curve with its extended and retracted part. The bold squares are used for the calculation of the Young's modulus using a Hertz based model⁹⁴. This model suggests that the Young's model depends on the film thickness and can be described as:

$$E = \frac{9F}{16 R^{1/2} \delta^{3/2} (1 + 0.884\chi + 0.781\chi^2 + 0.386\chi^3 + 0.0048\chi^4)} \quad (3.4)$$

F represents the force, R is the indenter curvature, δ is the indentation depth and χ contains the film thickness h as $\chi = \sqrt{R\delta}/h$. The film thickness is determined by using the imaging mode of the AFM. The indenter curvature

was determined with a scanning electron microscopy (SEM) as shown in Figure 3.4. The force curves were analysed with a self-made procedure (Igor Pro software).

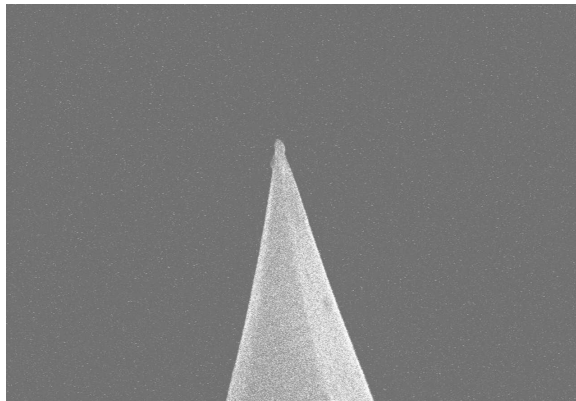


Figure 3.4: SEM image of an AFM tip. Scan size: $3 \times 3 \mu\text{m}^2$

3.2 Dynamic light scattering (DLS)

Dynamic light scattering is a method to determine the particle size of colloidal suspensions in bulk. An important magnitude in dynamic light scattering, but also in other scattering experiment, is the scattering vector \vec{q} , which is defined as:

$$|\vec{q}| = q = \frac{4\pi n}{\lambda} \sin \frac{\theta}{2} \quad (3.5)$$

π is a constant, n the refractive index, λ is the Laser wavelength and θ the scattering angle. The geometry of the \vec{q} vector is depicted in Figure 3.5.

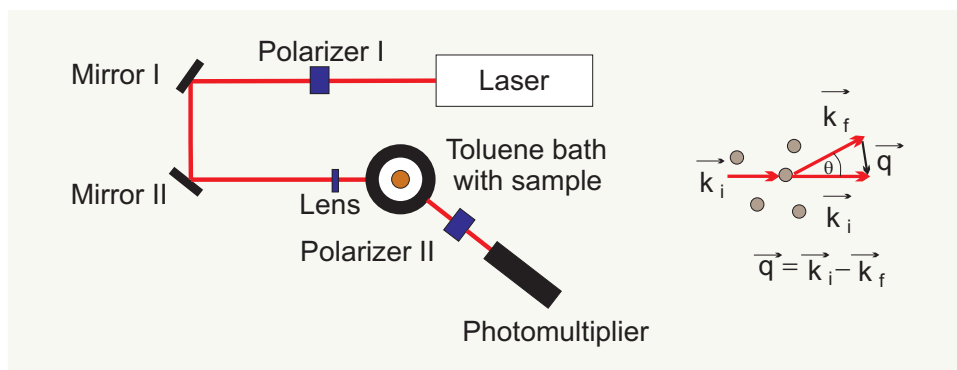


Figure 3.5: Schematic presentation of a DLS setup.

Figure 3.5 shows a typical setup of a DLS. A continuous wave Laser is guided to a lens system by two mirrors. The lens focuses the Laser on the sample in a toluene bath, which has the same refractive index of the used glass equipment and also serves for the control of the temperature. The scattered light is collected by a photomultiplier.

Due to diffusion of the particles (Brownian motion of the particle movement) the recorded scattered light intensity fluctuates. This fluctuations differ with time, which leads to the intensity time autocorrelation function $g^2(\tau)$:

$$g^2(\tau) = \frac{\langle I(t)I(t + \tau) \rangle}{\langle I(\tau) \rangle^2} \quad (3.6)$$

τ is the correlation time, $I(t)$ is the detected intensity. Such autocorrelation function can be transformed into a field autocorrelation function by the SIEGERT relation:

$$g^2(\tau) = 1 + \beta(g^1(\tau))^2 \quad (3.7)$$

β is a instrumental constant, which depends on the detector geometry.

If the studied solution consists of monodisperse particles $g^1(\tau)$ decays exponentially and can be expressed as follows:

$$g^1(\tau) = e^{-\Gamma\tau} \quad (3.8)$$

Γ is the relaxation rate.

For solution containing different particle sizes the situation changes, due to the different relaxation rates for different particle sizes. In this case, the single exponential function is not valid anymore. Furthermore, the sum of the different relaxation rate should be take into account:

$$g^1(\tau) = a_0 + a_1e^{-\Gamma^1\tau} + a_2e^{-\Gamma^2\tau} + a_3e^{-\Gamma^3\tau} \dots \quad (3.9)$$

a_0, a_1, a_2, \dots represent the amplitude, while $\Gamma^1, \Gamma^2, \Gamma^3$ are the corresponding relaxation rates.

The autocorrelation function $g^1(\tau)$ can be analysed with the cumulant method. This is performed with a function of $\ln g^1(\tau) - \ln g^1(0)$:

$$\ln g^1(\tau) = \ln A + \Gamma_1\tau + \frac{1}{2!}\Gamma_2\tau^2 + \frac{1}{3!}\Gamma_3\tau^3 + \dots \quad (3.10)$$

The diffusion coefficient can be determined as follows:

$$\Gamma_1 = Dq^2 \quad (3.11)$$

If the diffusion coefficient is known the Stokes-Einstein equation can be used for the calculation of the hydrodynamic particle radius R_h :

$$R_h = \frac{kT}{6\pi\eta D} \quad (3.12)$$

k presents the Boltzmann constant, T is the temperature, η presents the solution viscosity. Not only the particle size but also the polydispersity index (PDI) is accessible by the cumulant expansion:

$$PDI = \frac{\Gamma_2}{\Gamma_1^2} \quad (3.13)$$

Briefly, one can say that DLS is a powerful and essential tool for the investigation of the nanoparticle in bulk.

3.3 Zeta potential measurements

The surface charge of particles can be determined by the zeta potential measurements. The potential of charged particles in solution are mainly driven by ions. Counterions interact with the oppositely charge particle surface and form the so-called Stern or Helmholtz layer as shown in Figure 3.6. With increasing the distance to the charged particle the ion interaction to the particle surface weaken and loosely connected ions to the particle surface are present in a diffuse layer leading to an exponential decay of the potential. With applying an electric field, the particle starts to move and ions in the slipping plane will be dismantled and show a potential difference, which is known as zeta potential ξ .

The ξ -potential depends on the electrophoretic mobility of the particle μ_E , which is defined as:

$$v = \mu_E E \quad (3.14)$$

v is the particle velocity and E is the applied electric field.

From equation 3.14 the ξ -potential can be calculated via the Henry equation as follows:

$$\xi = \frac{3\eta\mu_E}{2\epsilon_0\epsilon_r f(\kappa R)} \quad (3.15)$$

ξ is the zeta-potential, ϵ_0 the vacuum permittivity, ϵ_r the relative permittivity, η is the dynamic viscosity of the used solution and $f(\kappa R)$ is the Henry

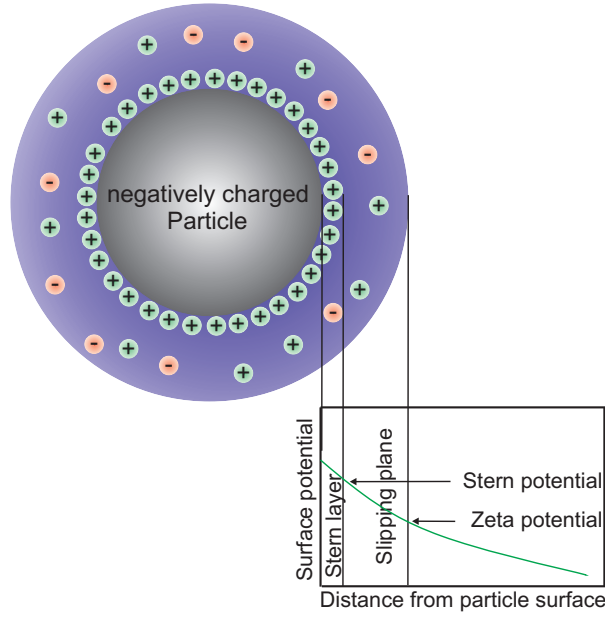


Figure 3.6: Schematic presentation of the ion distribution around the particle with the potential trend as a function of particle distance.

function, which includes the particle size and ionic strength via the Debye length κ .

Two approximations has to taken in consideration depending on the particle size. The Smoluchowski approximation with $f(\kappa R) \gg 1$ is used for large particles with the ξ -potential:

$$\xi = \frac{\eta\mu_E}{\epsilon_0\epsilon_r} \quad (3.16)$$

The Hückel approximation with $f(\kappa R) \ll 1$ is used for small particles with

$$\xi = \frac{3\eta\mu_E}{2\epsilon_0\epsilon_r} \quad (3.17)$$

3.4 Ellipsometry

Ellipsometry is based on polarised light and a suitable method for the determination of the thickness as well as the refractive index of thin films⁹⁵. An electromagnetic wave can be separated in an electric field \vec{E} and a magnetic field \vec{B} , which move perpendicular to each other and mutually perpendicular to the wave vector \vec{k} . The state of polarisation can be classified as a result of the trace of the electric field vector during one period. The possible polarisation states are linearly, circularly and elliptically. The given state of

polarisation can be described as a superposition of two linearly polarised light waves within a orthogonal coordinate system.

$$\vec{E}(\vec{r}, t) = \begin{pmatrix} |E_p| \cos(2\pi vt - \vec{k}\vec{r} + \delta_p) \\ |E_s| \cos(2\pi vt - \vec{k}\vec{r} + \delta_s) \end{pmatrix} \quad (3.18)$$

$|E_p|$ and $|E_s|$ represent the amplitudes, δ_p and δ_s are the phases, \vec{k} the wave vector and v the frequency. The state of the polarisation is represented by the amplitudes as well as the phase, while the time dependence is neglectable. The Jones vector is then defined as:

$$\vec{E} = \begin{pmatrix} |E_p| e^{i\delta_p} \\ |E_s| e^{i\delta_s} \end{pmatrix} = \begin{pmatrix} E_p \\ E_s \end{pmatrix} \quad (3.19)$$

The state of polarisation depends on the phases as follows:

1. linear, when $\delta_p - \delta_s = 0$ or $\delta_p - \delta_s = \pi$
2. elliptical, when $\delta_p \neq \delta_s$ and $|E_p| \neq |E_s|$
3. circular, when $\delta_p - \delta_s = \pi/2$ and $|E_p| = |E_s|$

The ellipsometry experiment the changes in the polarisation of the incident (\vec{E}_{inc}) and reflected light (\vec{E}_{ref}) is measured. The electric field vector for both p- and s-vectors remains linearly polarised and changes after the reflection. To quantify the changes, two parameters are introduced as follows:

$$\Delta = (\delta_p^r - \delta_s^r) - (\delta_p^i - \delta_s^i) \quad (3.20)$$

and

$$\tan \Psi = \frac{|E_p^r| / |E_p^i|}{|E_s^r| / |E_s^i|} \quad (3.21)$$

Here, Δ represents the changes in the phase, while the tangent of Ψ describes the changes in the amplitude.

The reflectivity properties of the layer is connected to the reflection coefficients r_p and r_s , respectively. This is given by:

$$r_p = \frac{|E_p^r|}{|E_p^i|} e^{i(\delta_p^r - \delta_p^i)} \quad (3.22)$$

and

$$r_s = \frac{|E_s^r|}{|E_s^i|} e^{i(\delta_s^r - \delta_s^i)} \quad (3.23)$$

From this relation the ellipsometry equation can be written as:

$$\tan \Psi e^{i\Delta} = \frac{r_p}{r_s} \quad (3.24)$$

Usually, $\tan \Psi$ and Δ is measured. With the knowledge of these two parameters and a suitable layer model the thickness and refractive index is accessible.

3.5 Contact angle measurements

Contact angle measurement is a simple and fast method to determine the surface wettability. Thus, the surface is covered by the investigated polymer film and a liquid drop is placed on the surface. The angle between the liquid and the substrate is then called the contact angle θ as shown in Figure 3.7.

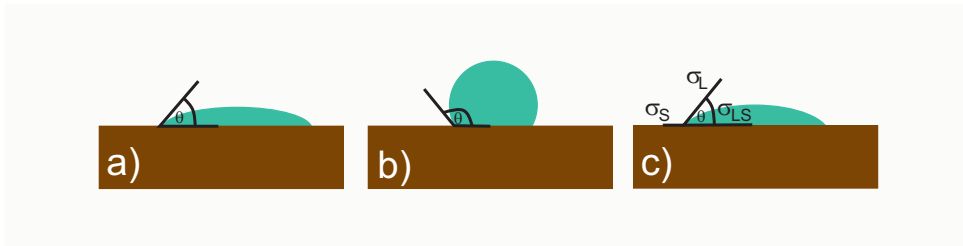


Figure 3.7: Schematic presentation of contact angle of a water droplet. a) hydrophilic surface with a contact angle lower than 90° , b) hydrophobic surface with a contact angle higher than 90° , c) contact angle with its surface tension contributions.

A surface is called hydrophilic when a water droplet exhibits a contact angle lower than 90° as shown in Figure 3.7a). A surface is hydrophobic if the water drop have a contact angle higher than 90° as shown in Figure 3.7b).

The contact angle can also be calculated with the Young's equation:

$$\cos \theta = \frac{\sigma_S - \sigma_{LS}}{\sigma_L} \quad (3.25)$$

σ_S is the surface tension of the substrate, σ_{LS} represents the surface tension between the substrate and liquid, σ_L represents the surface tension of the liquid.

Chapter 4

Experimental section

4.1 Materials

The monomer N-isopropylacrylamide (NIPAM, 97 %), the co-monomer allyl acetic acid (AAA, 97 %) as well as acrylic acid (AAc, 99 %), the cross-linker N,N'-methyleneacrylamide (BIS, 95 %) were obtained from Sigma Aldrich. The radical starter potassium persulfate (KPS, 99 %) was obtained from Fluka. For the co-non-solvency experiments, ethanol (EtOH, for synthesis, Merck), iso-propanol (iPr, p.a., Merck) and tetrahydrofuran (THF, 99.9 %, Sigma Aldrich) were used to induce the particle collapse. For the polyelectrolyte multilayer experiments, polyethylenimine (PEI, Sigma Aldrich), polyallylamine hydrochloride (PAH, Sigma Aldrich), 3-aminopropyltrimethoxysilane (AMPS, Sigma Aldrich) and polystyrene sulfonate (PSS, Sigma Aldrich) were used. The chemical structures are shown in Figure 4.1.

For AFM experiments both silicon wafer (Wacker Syntronic AG) and gold coated silicon wafer (Georg Albert PVG-Beschichtungen) were used. The used water was filtered by a Milli-Q system.

4.2 Microgel synthesis

The microgels were prepared via surfactant free precipitation polymerisation⁴⁵. The monomer NIPAM, cross-linker BIS and the desired co-monomer content (with respect to the NIPAM mass) were dissolved in Milli-Q water. The solution was heated to 70 °C under a constant nitrogen stream and allowed to equilibrate for 30 min at this temperature. To start the polymerisation, a solution of 1.5 mg KPS dissolved in 1mL Milli-Q water was added. Within 10 minutes, the colourless solution turned into a milky mixture. After a

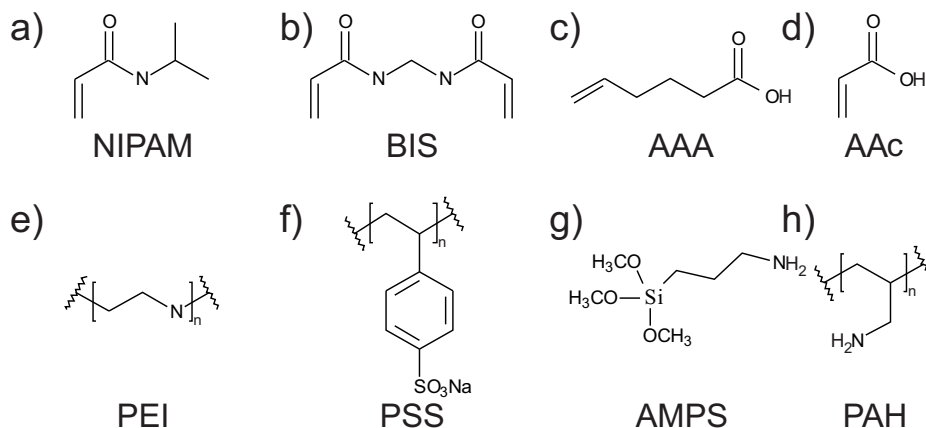


Figure 4.1: Chemical structures of a) NIPAM, b) BIS, c) AAA, d) AAc, e) PEI, f) PSS, g) AMPS and h) PAH.

reaction time of 4 hours at 70 °C, the mixtures was cooled to room temperature and stirred over night. The suspension was centrifuged for one hour at 9000 rpm and afterwards dialysed for 14 days with daily water exchange. The cleaned microgel was freeze-dried. The synthesised microgels are listed in Table 4.1. AAA-10 and P10 exhibit nominal the same AAA content, but are two different batches.

Table 4.1: The synthesised microgels. The second shows the cross linker-content with respect to the NIPAM mass. The third and fourth column specifies the co-monomer content AAc and AAA with respect to the NIPAM mass.

Microgel type	BIS, %	AAc, %	AAA, %
PNIPAM-5	5	-	-
AAc-50	5	50	-
AAA-5	5	-	5
AAA-10	5	-	10
AAA-20	5	-	20
AAA-25	5	-	25
AAA-50	5	-	50
P10	5	-	10

4.3 DLS experiments

The dynamic light scattering measurements were performed with two different setups. The particles were measured using an ALV goniometer setup with a

Nd:YAG laser at a wavelength of 532 nm. Due to the low polydispersity of the solution, the scattering angle was fixed to 60 °. The obtained data were analysed by CONTIN⁹⁶.

The change in the particle size in chapter 8 was record using a Zetasizer Nano ZS (Malvern Instruments Ltd.). In the light scattering experiments the scattering angle was fixed to 173 °.

4.4 Sample preparation

To study single adsorbed particles with the AFM, the sample preparation was as follows:

The cleaned silicon wafer were coated with PAH by dipping in aqueous PAH solution (0.1 M) for 30 min. Afterwards the coated silicon wafer was washed with Milli-Q water for one minute to remove residual polyelectrolyte. A 0.05 wt-% microgel solution was spin coated on the PAH coated silicon wafer using a SCS P6700 spin coater. The spin coating process was performed at 2000 rpm for 300 s to ensure single adsorbed microgel particles⁵⁵.

For contact angle measurements, a monolayer of the investigated particles is necessary and can be achieved as follows: a 0.5 wt-% particle solution was spin coated on a PAH coated silicon wafer. The spin coating process was performed at 500 rpm at 300 s to gain a close-packed particle layer⁵⁸.

4.5 Preparation of the polyelectrolyte multilayer

To form polyelectrolyte multilayers the well-known layer-by-layer technique developed by Decher was used⁴⁴. The procedure is shown in Figure 4.2 and can be described as follows: The cleaned silicon wafer was first coated with 0.1 M polyethylenimine (PEI) solution for 30 min. The PEI layer serves as primer for all polyelectrolyte multilayers. To remove residual polyelectrolyte the coated wafer was rinsed with Milli-Q water three times for one minute. On the PEI layer, several polyelectrolyte (PAH, PSS, AMPS) were adsorbed. The PEI coated silicon wafer were deposited in the desired polyelectrolyte solution for 30 min. Afterwards the coated wafer was rinsed with Milli-Q water three times for one minute. This procedure was also used to prepare Si/PEI/(PSS/PAH)_x with $x = 1, 3, 6$. The concentration of all used polyelectrolyte solutions was 0.1 M.

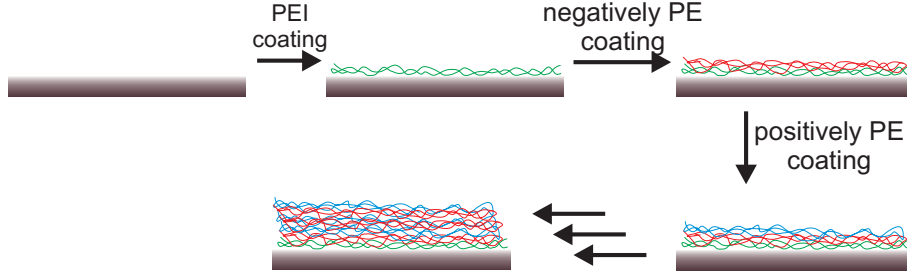


Figure 4.2: Preparation of the multilayer systems.

4.6 AFM experiments

All AFM measurements were performed with a JPK NanoWizardII from JPK Instruments. AFM images under ambient conditions were recorded with a AC 160 TC probe from Olympus in intermittent contact mode. The liquid measurements as well as the force measurements were carried out in an ECell from JPK instruments. The imaging in liquid state was performed with an uncoated CSC 37 cantilever, while for force measurements an uncoated CSC 38 probe was used. Both cantilever types were obtained from MicroMasch. In this thesis two kind of VPTT are named. $VPTT_{imaging}$ is obtained from imaging experiments, while $VPTT_{force}$ is generated from force measurements.

The particle volume from adsorbed microgels were calculated for at least three particles with equation 4.1:³⁵

$$V_{AFM} = \pi \int_0^h f^2(l) dl \quad (4.1)$$

where h is the particle height, $f(l)$ represents the cross section and l is the scan direction.

In this work, another important parameter for AFM measurements is introduced. The swelling ratio f_V depicts the swelling ability of the microgels from ambient conditions to the liquid state and is defined as:

$$f_V = \frac{V_{liquid}}{V_{ambient}} \quad (4.2)$$

V_{liquid} is the particle volume in the liquid state, while $V_{ambient}$ is the particle volume at ambient conditions. The swelling ratio f can be also written as a function of particle height f_h or particle width f_w . Due to the introduction of the swelling ratio, one obtains information about the swelling ability of the studied particle.

4.7 Contact angle measurements

The contact angle measurements were performed via the sessile drop method using an OCA system. A microgel solution with a concentration of $w=0.5$ wt-% was used to form a close-packed particle monolayer via spin coating at 500 rpm for 300 s. A water droplet was placed on the particle monolayer and the contact angle of the water droplet was determined by the direct observation of the drop shape.

Chapter 5

Mechanical properties of microgels

5.1 Introduction

Hydrogels are in the focus of a variety of research fields. One of the mostly investigated polymer is N-isopropylacrylamide (NIPAM) due to its volume phase transition temperature (VPTT) of around 32 °C, which is close to the human body temperature^{5,9–11,97}. Below this temperature, water serves as "good" solvent leading to a highly swollen polymer network. At temperatures exceeding the VPTT, the hydrogel excludes water and polymer-polymer interactions are favoured leading to a particle collapse. PNIPAM based microgels are not only sensitive to temperature changes but also to other external parameters such as solvent quality⁴², ionic strength^{25,55} and pH^{25,98,99}. Switching from swollen to the shrunken state offers applications in multiple areas like drug delivery^{100–102}, coatings^{58,69,77}, and sensors²⁹.

Especially for coating applications, various methods are accessible to study the particle behaviour^{69,103,104} at an solid interface. To determine the local mechanical stiffness of adsorbed particles atomic force microscopy is the essential method^{37,73}. The particle composition plays a crucial role for the particle stiffness. Below VPTT, particles with a lower cross-linker content exhibit a lower particle stiffness compared to particles with higher cross-linker content⁶⁷. With increasing the temperature above VPTT the polymer network collapses resulting to an tremendous increase in the particle stiffness compared to the swollen particles at low temperatures. The particle stiffness between swollen and deswollen particles can differ by a factor of 7⁶⁸. However, not only different cross-linker content affects the particle stiffness but also the incorporation of co-monomers has an impact on the particle stiffness. Burmistrova *et al.* compared the particle stiffness of pure PNIPAM and PNIPAM-co-AAc

particles³⁵. At temperatures below VPTT both particles, pure PNIPAM and PNIPAM-co-AAc, exhibit almost the same Young's modulus. With increasing the temperature across VPTT, highly charged PNIPAM-co-AAc particles show a decrease in the particle stiffness compared to pure PNIPAM particles due to electrostatic repulsion in PNIPAM-co-AAc particles.

Other groups also showed that not only electrostatic repulsion but also other interactions such as hydrophobic effects affects the particle behaviour^{105–108}. Since hydrophobic interactions result often to a counteractive effect the question arises which effect has a co-monomer with amphiphilic character on the mechanical particle properties.

This paper deals with the investigation of mechanical properties of single adsorbed particles on a surface. The impact of the various co-monomers on particle stiffness is studied. For this purpose, the more hydrophilic AAc and the amphiphilic AAA have been incorporated into the microgels. Furthermore, the shrinking behaviour for both particle types is correlated with the mechanical properties. The shrinking behaviour and the indentation experiments for adsorbed particles were followed via atomic force microscopy (AFM). Additionally, we measured the contact angle to understand the hydrophobic nature of the particle. Furthermore, we performed dynamic light scattering to study the particles in the bulk phase.

5.2 PNIPAM based microgels: Competing impact of hydrophobic and electrostatic interactions on mechanical properties

5.2.1 Results

Microgel behaviour in bulk phase

Figure 5.1 shows the particle volume (a) and swelling ratio (b) for AAA microgels as a function of temperature. The swelling ratios were calculated with respect to the particle volume at 20 °C. The particle volume increases with increasing the co-monomer content, due to the higher charge density within the particles. The incorporation of AAA affects no significant shift in the VPTT of the particles. PNIPAM-5, AAA-10 and AAA-20 particles collapse at 32 °C. At very high AAA content, however, a slight increase of the VPTT to 34 °C takes place as shown for AAA-50 particles. All AAA particles show only *one* VPTT independent of their AAA content. In contrast to AAA

Table 5.1: VPTT of the synthesised microgels in the bulk phase. Values marked with * of AAc-10 and AAc-20 were published previous by our group³⁵

Microgel name	VPTT, °C	
PNIPAM-5	32	
AAA-10	32	
AAA-20	32	
AAA-50	34	
AAc-10*	31	46
AAc-20*	33	45
AAc-50	29	46

particles, the shrinking behaviour of AAc particles (AAc-10 and AAc-20 data published before by our group³⁵ expect AAc-50 particles) strongly depends on the co-monomer content. With incorporation of AAc and increasing this AAc content, the VPTT increases towards higher temperatures. Furthermore, all AAc particles exhibit not only one but two VPTTs. The first transition of AAc particles takes places between 29 and 33 °C, which equals the collapse of pure PNIPAM. The second phase transition occurs at around 46 °C and equals the complete particle collapse as discussed below. It seems, that the second VPTT is independent of the AAc content. The VPTTs of AAA and AAc microgels are summarised in Table 5.1.

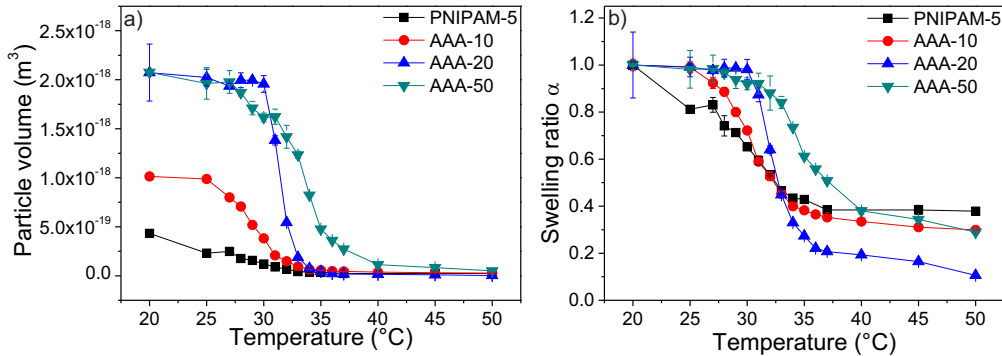


Figure 5.1: Particle volume (a) and swelling ratio (b) of AAA microgels in the bulk phase as a function of temperature.

Shrinking behaviour of adsorbed AAA- and AAc-microgels

Figure 5.2 shows exemplarily AFM images of PNIPAM (a, e), AAA-10 (b, f), AAA-20 (c, g), and AAA-50 (d, h) particles at 20 °C and 50 °C. From these

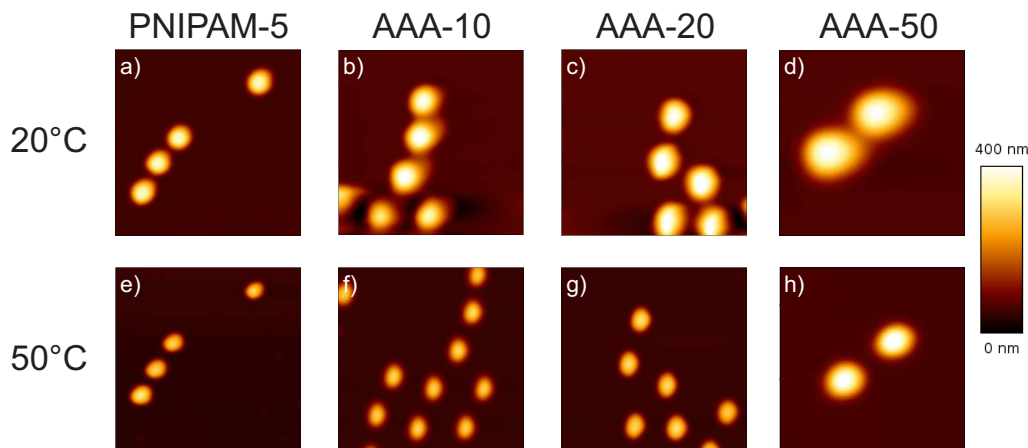


Figure 5.2: AFM images of pure PNIPAM (a, e), AAA-10 (b, f), AAA-20 (c, g) and AAA-50 (d, h) at 20 °C (a,b, c, d) and 50 °C (e, f, g, h), respectively. Scan size: 5x5 μm

AFM images, the particle cross sections were extracted as shown in Figure 5.3. Both Figures indicate a clear thermo-responsive behaviour of particles, i.e. their swollen state at low temperatures and their deswollen state at high temperatures. The particle shrinking takes place in vertical and lateral dimension. In order to determine the VPTT of the particles, the particle volume was calculated from the cross section. Figure 5.4 shows the particle volume (a) and swelling ratio (b) of AAA microgels. The swelling ratio was calculated with respect to the particle volume at 20 °C. Adsorbed particles exhibit a similar behaviour as particles in bulk phase and undergo a VPT with increasing the temperature. As shown in Table 5.2, the incorporation of AAA increases the $VPTT_{imaging}$ from 33 °C for PNIPAM-5 particles to 36 °C for AAA-10. Further increase in the AAA content results in a more pronounced $VPTT_{imaging}$ increase. AAA-20 particles shrink at 37 °C, while AAA-50 particles collapse at 40 °C. However, the VPTT of all adsorbed AAA particles increases towards higher temperatures compared to their counterparts in bulk. The swelling ratio provides further information about the particle behaviour. PNIPAM-5 and AAA-50 exhibit a swelling ratio of around 0.5, while for AAA-10 and AAA-20 the swelling ratio were determined to around 0.6. The difference between the individual swelling ratios suggest an interplay between electrostatic and hydrophobic interactions within the particles.

AAc microgels show a similar trend as AAA microgels (AAc-10 and AAc-20 data published before by our group³⁵ expect AAc-50 particles). The $VPTT_{imaging}$ shifts towards higher temperatures with increasing the co-monomer content. AAc-10 particles collapse at 40 °C. AAc-20 and AAc-50 particles

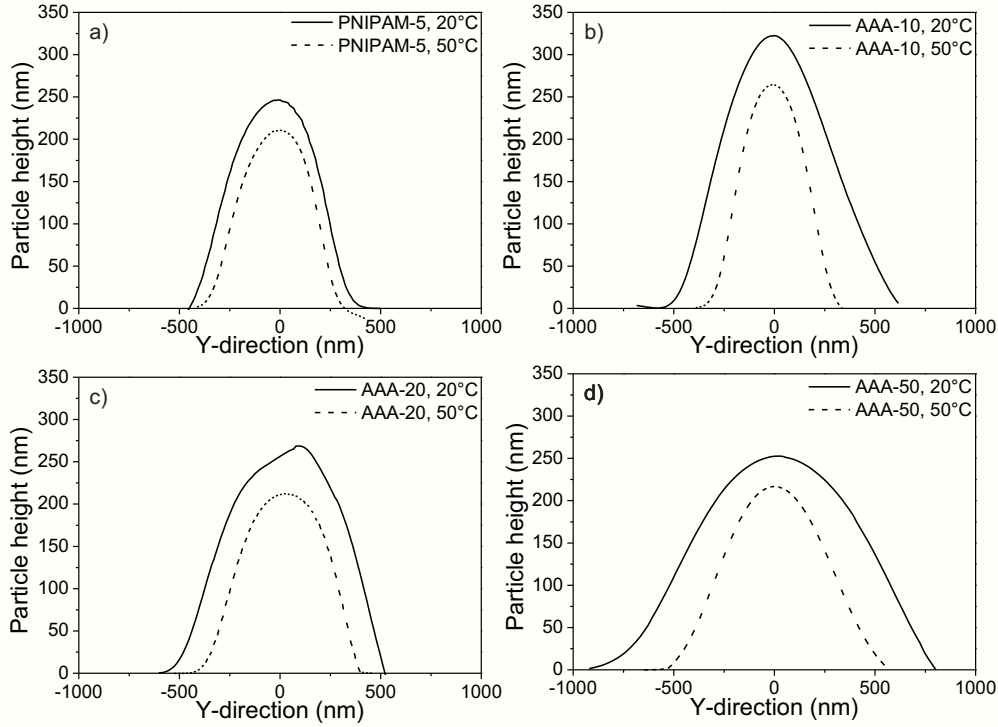


Figure 5.3: Particle cross sections of PNIPAM-5 (a), AAA-10 (b), AAA-20 (c) and AAA-50 (d) at 20 °C (straight line) and 50 °C (dashed line).

shrink at 42 °C and 45 °C, respectively. As shown in Table 5.2, AAc particles exhibit a stronger increase in the $VPTT_{imaging}$ as their corresponding AAA counterparts indicating stronger electrostatic repulsion within AAc microgels.

Young's modulus of adsorbed PNIPAM-co-AAc and PNIPAM-co-AAA microgels

Figure 5.5 shows the Young's modulus of the whole AAA-20 particle at 20 °C and 50 °C. It should be noted, that the scale bars for 20 °C and 50 °C differ from each other, due to the large difference in the particle stiffness. Below the VPTT, the highest Young's modulus is located in the particle centre and decreases to the particles periphery. With increasing temperature, two effects are observed. The particle size of AAA-20 decreases, due to the particle collapse, and the particle stiffness increases, which is a direct result from the particle collapse. In order to understand change of the particle stiffness of AAA microgels during the particle collapse, indentation measurements were performed at different temperatures. These indentation measurements were also performed for AAc microgels to understand the origin of the different shrinking behaviour between AAA and AAc microgels.

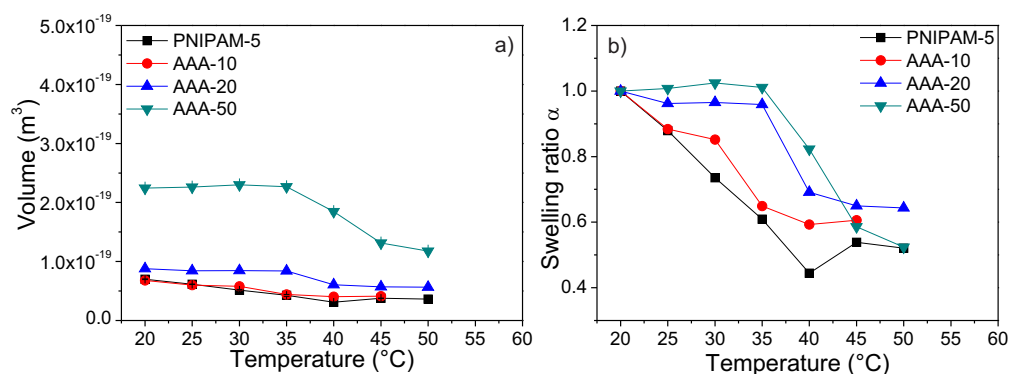


Figure 5.4: Particle volume (a), swelling ratio (b) and the surface-to-bulk ratio (c) of AAA microgels as a function of temperature. The swelling ratio was calculated with respect to the particle volume at 20 °C. The surface-to-bulk ratio is a ratio between the volume of the particles at the surface and from the bulk phase. Error bars are within the symbols.

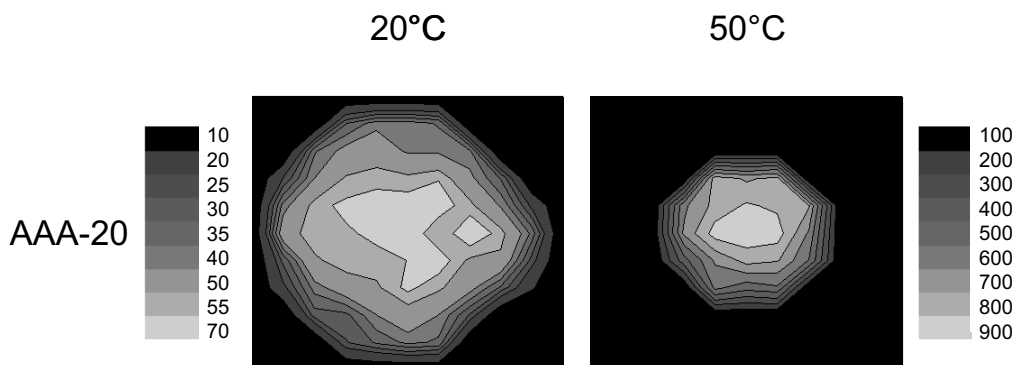


Figure 5.5: Young's modulus of the whole particle for AAc and AAA-20 at 20 °C and 50 °C, respectively. The bright colour indicate a large Young's modulus, while the darker parts exhibit a low Young's modulus. Scan size: $1 \times 1 \mu m$

Figure 5.6 shows the Young's modulus for AAc (a) and AAA microgels (b) as a function of temperature (AAc-20 data published before by our group³⁵ expect AAc-10 and AAc-50 particles). It should be noted, that all data points shown in Figure 5.6 are taken from the particle centre. AAc and AAA particles show the same qualitative trend and exhibit their lowest Young's modulus at temperatures below 30 °C. However, it should be noted, that pure PNIPAM particles are stiffer than AAc and AAA microgels. Above VPTT, the stiffness of all particles increases, due to particle shrinking.

It is obvious, that both co-monomers have a different impact on the particle stiffness at high temperatures. The incorporation of AAA leads to a decrease in the particle stiffness leading to softer AAA-10 particles compared to pure

Table 5.2: VPTT and the contact angle of the synthesised microgels. The second column shows VPTT obtained from imaging experiments, while the third shows the VPTT obtained from indentation experiments. The fourth column represents the contact angle of a water droplet on a microgel monolayer. Values marked with * of AAc-10 and AAc-20 were published previous by our group³⁵

Microgel name	$VPTT_{imaging}, ^\circ\text{C}$	$VPTT_{force}, ^\circ\text{C}$	contact angle, $^\circ$
PNIPAM-5	33	37	25.7 ± 4.3
AAA-10	36	40	38.6 ± 0.9
AAA-20	37	42	76.5 ± 4.9
AAA-50	40	55	93.2 ± 6.4
AAc-10	36*	45	63.4 ± 3.7
AAc-20	46*	55*	68.4 ± 3.4
AAc-50	45	-	69.8 ± 11.5

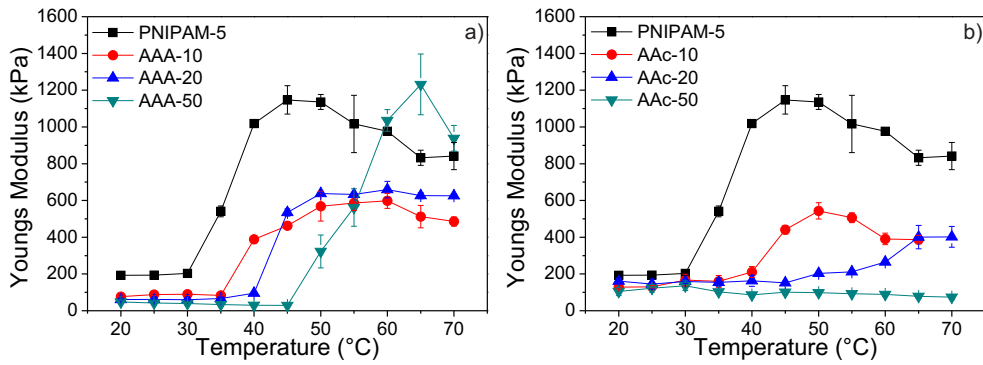


Figure 5.6: The Young's modulus of AAc (a) and AAA particles (b) as a function of temperature. Data points for AAc-20 were published previous by our group³⁵

PNIPAM particles, due to the electrostatic repulsion within AAA-10. Further increase in the AAA content results in a steady increase of the Young's modulus as observed for AAA-20 particles compared to AAA-10 particles. The Young's modulus increases from around 590 kPa for AAA-10 particles to 630 kPa for AAA-20 particles. The particle stiffness of AAA-50 is 1200 kPa and therefore higher than for pure PNIPAM particles with 1070 kPa. The steady increase of the particle stiffness in the AAA microgel series indicates extra interaction within the particles. To understand the nature of this behaviour, contact angle measurements were performed at a closed packed AAA microgel monolayer at room temperature. The results are shown in Table 5.2. An increase in AAA content leads to a more hydrophobic particle resulting in larger contact angle.

The incorporation of AAc leads again to a decrease in particle stiffness compared to pure PNIPAM particles. In contrast to AAA particles, a further increase in the AAc content results in a steady decreases in the particle stiffness. AAc-10 particles exhibit a Young's modulus of around 560 kPa, while AAc-20 particles has a Young's modulus of around 400 kPa. However, AAc-50 does not show a change in the particle stiffness over the whole temperature range. The monotonously decreases in the particle stiffness indicates an increased charge density within the microgels. It should be noted, that the particle stiffness decreases again at very high temperatures. This could be related to the relaxation of the polymer network and is still under investigation of further experiments. Contact angle measurements were also performed at a closed packed AAc microgel monolayer at room temperature, which remains more or less constant and therefore independent of the AAc content.

The incorporation of different co-monomers affects not only the particle stiffness but also also the VPTT of the particles. As observed in imaging experiments, an increase in the co-monomer content leads to an increase in the VPTT towards higher temperature. However, the $VPTT_{force}$ of AAc microgels exhibits a stronger shift as their AAA counterparts. Furthermore, Table 5.2 compares $VPTT_{imaging}$ and $VPTT_{force}$, of the particles. Interestingly, the VPTT of the particle increases from imaging ($VPTT_{imaging}$) to indentation ($VPTT_{force}$) experiments.

5.2.2 Discussion

In order to understand the competition between electrostatic and hydrophobic interaction, two types of microgels have been studied; particles with the more

hydrophilic co-monomer AAc and particles with the amphiphilic AAA. The behaviour of AAA microgels show a strong interplay between electrostatic and additional hydrophobic interaction, while the behaviour of AAc microgels is clearly driven by electrostatic repulsion.

The impact of electrostatic interaction on microgel behaviour

Microgels with various AAc and AAA contents have been investigated to study the impact of charge density, and therefore enhanced electrostatic interaction within the particles. Compared to pure PNIPAM particles, the incorporation of AAc results in an increasing particle size and an increased VPTT towards higher temperatures in the bulk phase. This is related to the repulsive interaction between the co-monomer charges and an increased osmotic pressure^{27,35,55}. Interestingly, AAA microgels exhibit only *one* VPTT, while two VPTTs can be observed for AAc microgels. This behaviour will be discussed below.

Both, AAc and AAA, particles show compression during the spin coating process. Hence, the particle volume of adsorbed particles is smaller compared the particle volume in bulk below the VPTT. Additionally, the interaction between the particle and surface cannot neglected and exhibit an impact on the particle volume⁷¹. The pH values of AAc and AAA particles are well above their pKa resulting in electrostatic attraction between the positively charged PAH layer and the negatively charged particles. Hence, strong particle-to-surface interaction takes place leading to a smaller particle volume. With increasing the temperature above VPTT, the particle-to-surface attraction becomes more pronounced leading to a decreased deswelling ability of the particles. The decreased deswelling ability assumes a large charge density, which consequently results in strong electrostatic repulsion within the particles and larger adsorbed particles compared to their collapsed bulk counterparts. This behaviour was observed before⁵⁶.

The increased repulsive interaction within the particles prevent not only a complete particle collapse, but results also in an increase in the VPTT of the particles. This effect becomes more apparent with increasing the co-monomer content. The VPTT of adsorbed AAA and AAc particles increases from 32 °C for PNIPAM-5 particles to 40 °C for AAA-50 and 45 °C for AAc-50 particles, respectively. To understand the VPTT shift, the particle morphology has to be considered³⁵. It is assumed that microgels consist of PNIPAM-rich and co-monomer-rich domains, which are formed during the synthesis due to the differing reactivity of the components. In adsorbed particles, these

both domains, PNIPAM-rich and co-monomer-rich, interdigitate leading to only one average VPTT. The interdigitation of the domains has also a direct impact on the elasticity of the particles below the VPTT. The incorporation of co-monomer into the particles leads to particle softening compared to pure PNIPAM particles due to the more flexible polymer network.

The impact of electrostatic and hydrophobic interaction on microgel behaviour

As mentioned above, the remarkable difference between bulk AAA and AAc microgel is the one step VPT of AAA and the two VPT of AAc microgels. This observation assumes a competition between electrostatic repulsion and hydrophobic attraction within AAA microgel, while the behaviour of AAc microgels is clearly driven by electrostatic nature.

The extra hydrophobic attraction within the particles counteract the electrostatic repulsion leading to only *one* VPTT of the AAA particles, both in bulk and at the surface. The decrease in the VPTT of AAA microgels, in comparison to AAc microgels, is consistent with the literature. An increase in the hydrophobicity leads to a decrease in the VPTT¹⁰⁵. During the particle collapse, the highly swollen and hydrophilic PNIPAM particles turn into more hydrophobic particles. The increased hydrophobicity of the particle favours bonds with hydrophobic parts of the incorporated co-monomers. In case of AAA microgels, the hydrophobic tail of the AAA and the PNIPAM backbone form additional hydrophobic bonds during the particle collapse (shown in Figure 5.7) and influence the particle behaviour. Fan *et al.* have shown the incubation of organic salt into microgels^{106,109}. The incubation of organic salt is driven by hydrophobic interaction between the isopropyl group and the alkyl tail of the organic salt. The same effect leads to an enhanced attraction between the hydrophobic tail of the AAA and the PNIPAM backbone resulting in a compact polymer network.

If additional hydrophobic attraction within AAA particles take place, a particle stiffening should be observed. Indentation measurements of AAA microgels confirm this assumption. Measurements in the particle centre show competition between electrostatic repulsion and hydrophobic attraction. AAA-10 particles experience a particle softening compared to pure PNIPAM particles. This indicates, that electrostatic repulsion dominates the hydrophobic attraction at low AAA co-monomer content as for AAc particles. Increasing the AAA content results in stronger hydrophobic attraction within the particle, which overcome the electrostatic repulsion leading to a particle stiffening at high temperatures. AAc microgels, which are clearly dominated by electro-

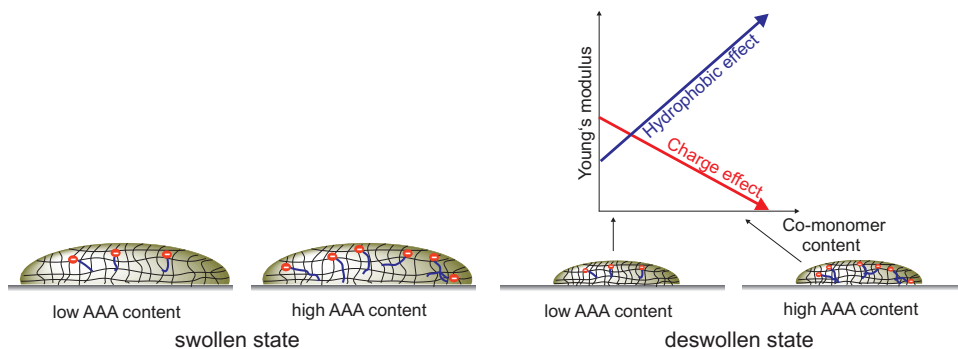


Figure 5.7: Counter acting effect of electrostatic and hydrophobic interactions within the particle. At low AAA content electrostatic repulsion dominates, while hydrophobic attraction dominates at higher AAA content.

static repulsion, show a monotonously decrease in the particle stiffness due to the less compact polymer network. Certainly, the behaviour of adsorbed AAA microgel indicates the complexity of these particles. Adsorbed AAA microgels show an increase in the VPTT with increasing the AAA content. The increase in the VPTT can be attributed to the compressed nature of the particles leading to a strong overlapping of the PNIPAM-rich and AAA-rich domains³⁵. Hence, the charge density within the AAA particles increases and, in comparison to bulk AAA microgels, compensates the additional hydrophobic attraction leading to an increase in the VPTT of adsorbed AAA microgels. This is in contrast to the findings in indentation experiments, where the particle stiffness increases due to the hydrophobic attraction. But it should be noted, that scanning experiments takes place on the particle periphery, while the particle stiffness is measured in the particle interior (indentation depth around 128 nm). The co-monomer units are located in the particle shell⁹⁸. The hydrophobic alkyl chain, however, is more directed towards the particle interior.

Another indication for the interplay between electrostatic repulsion and hydrophobic attraction is concluded from contact angle measurements. With increasing AAA content, a steady increase in contact angle takes place. The lowest contact angle was observed for AAA-10, while AAA-50 particles exhibit the largest contact angle. Thus, it is concluded, that the hydrophobicity increases with incorporation of AAA. In contrast to that, the contact angle of the AAc microgels remains more or less constant with increasing the AAc content. This assumes that the behaviour of AAc microgels is not influenced by additional hydrophobic interaction.

Differences in $VPTT_{imaging}$ and $VPTT_{force}$

Both microgels show the same trend between $VPTT_{imaging}$ and $VPTT_{force}$. All particles show a lower VPTT in imaging measurements ($VPTT_{imaging}$), while force measurements ($VPTT_{force}$) reveal a particle collapse at higher temperatures. The differences between the two VPTT might arise from the core-shell-like character of the particles^{35,110}. The particle interior is highly cross-linked, due to faster cross-linker consumption at the beginning of the synthesis¹¹¹. The cross-linking decreases towards the particle periphery, which forms the particle shell. Furthermore, most of the co-monomer charges are located in the lower cross-linked particle shell⁹⁸. With increasing temperature, the particle core collapses first, while the particle shell remains swollen due to the electrostatic repulsion. Hence, the particle volume decreases, while the Young's modulus remains low, since particle stiffness is mainly measured in the particle periphery. A further temperature increase allows a collapse of the particle shell. Consequently, the further decrease in the particle volume takes place, while an increasing Young's modulus is observed, since the particle stiffness is determined in the collapsed particle shell. This two-step particle shrinking, separated into particle core and shell collapse, is assumed to result in differences of the $VPTT_{imaging}$ and $VPTT_{force}$. Furthermore, the shift from $VPTT_{imaging}$ to $VPTT_{force}$ becomes larger with increasing the co-monomer content indicating an enhanced co-monomer content within the particle shell and a larger particle shell for microgels with higher co-monomer incorporated.

5.2.3 Conclusions

The chapter addresses the competition between hydrophilic and hydrophobic interaction of PNIPAM microgels, which differ in type and concentration of the co-monomer. The used co-monomers are the well known acrylic acid (AAc) and the amphiphilic allyl acetic acid (AAA). The Young's modulus was determined for AAc and AAA microgel and correlated to the shrinking behaviour at the surface as well as in bulk. Furthermore, the contact angle was determined for adsorbed particles.

AAc microgels show an increase in their particle size and VPTT for both, bulk and adsorbed, particles and a particle softening with increasing the AAc content. The behaviour of AAc microgels is clearly dominated by electrostatic repulsion within the particles. In contrast, AAA microgels exhibit only *one* VPTT in bulk phase and show an increase in the particle stiffness with increasing the AAA content. The increase in the VPTT of adsorbed AAA particles

displays the complexity of the interplay between electrostatic repulsion and hydrophobic attraction within the AAA particles.

Due to a long-chained co-monomer, two features for PNIPAM-co-AAA microgels are accessible. The particle properties below the VPTT are mainly dominated by electrostatic repulsion, while the hydrophobic attraction between the co-monomer and the polymer backbone influences the particle behaviour above the VPTT. This makes it possible to develop new and innovative sensor and coating applications.

5.3 Polyethyleneglycol (PEG) based microgels

5.3.1 Results

The studied microgels were synthesised by Nathalie Pinkerton from Princeton University. The microgels are composed of 1k PEG polymerised into microgel particles using a Micheal addition reaction. The difference between the individual samples is the PEG concentration at the time of polymerisation. The concentrations were 30, 40, 50 and 60 % PEG. Another approach was the incorporation of polystyrene nanoparticles. Therefore, the used PEG concentration was fix to 30 % and different concentration of nanoparticles (2.5, 5, 7.5 and 10 wt-%) were incorporated. The eight microgels are listed in Table 5.3.

Table 5.3: The particles obtained from the Prud’homme group at Princeton University. The second column represents the PEG concentration, while the third column specifies the polystyrene content.

Sample name	PEG content wt-%	Polystyrene content wt-%
PEG-30-NP-2.5	30	2.5
PEG-30-NP-5.0	30	5.0
PEG-30-NP-7.5	30	7.5
PEG-30-NP-10	30	10
PEG-30	30	-
PEG-40	40	-
PEG-50	50	-
PEG-60	60	-

For AFM measurements, the samples were spin coated for 300 s at 2000 rpm onto gold coated silicon wafers. Figure 5.8 shows the AFM height images as

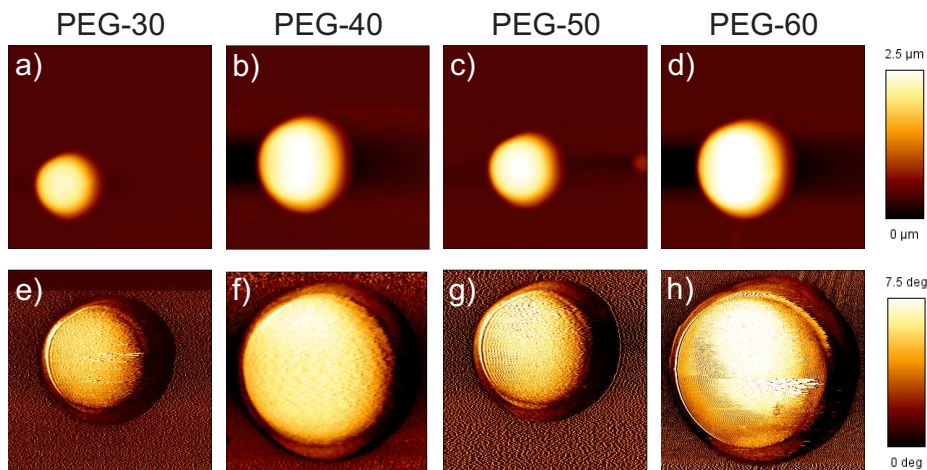


Figure 5.8: PEG particles with different PEG content. The numbers indicate the PEG content in the particle. Top row: AFM height images Scan size: $10 \times 10 \mu\text{m}^2$. Bottom row: AFM phase images Scan size: $4.5 \times 4.5 \mu\text{m}^2$.

well as the AFM phase images for particles with 30 wt-% PEG (PEG-30), 40 wt-% PEG (PEG-40), 50 wt-% PEG (PEG-50) and 60 wt-% PEG (PEG-60), respectively. The particle size is independent on the PEG content of the particles and no trend can be observed. PEG-30 and PEG-50 particles exhibit the smallest particle size, while PEG-40 and PEG-60 particles are the largest ones. Furthermore, all PEG particles show no difference in the phase images and display a smooth particle shape.

In order to study the impact of PEG content on the particle stiffness, indentation measurements have been performed. Figure 5.9 shows the particle cross section and the Young's modulus of the particular PEG particles. PEG-30 and PEG-40 particles exhibit the lowest particle stiffness, while an increase in the PEG content causes an increase in the particle stiffness as shown for PEG-50 as well as PEG-60 particles. Furthermore, the highest Young's modulus is centrally located and decreases towards the particle periphery.

Additionally, four samples with a fixed PEG content of 30 % and different polystyrene content have been synthesised to study the impact of nanoparticles content on the particle stiffness. Figure 5.10 shows the AFM height (a-d) as well as phase image (e-h) for PEG-30 particles with different polystyrene content incorporated. The particle height differs for all particles and shows no significant trend. The smallest particles were obtained with 5 wt-% as well as 7.5 wt-% NP incorporated. The largest particle size can be observed for PEG-30-NP-10 particles. The AFM phase images show an interesting particle feature. While the AFM height image shows a uniform

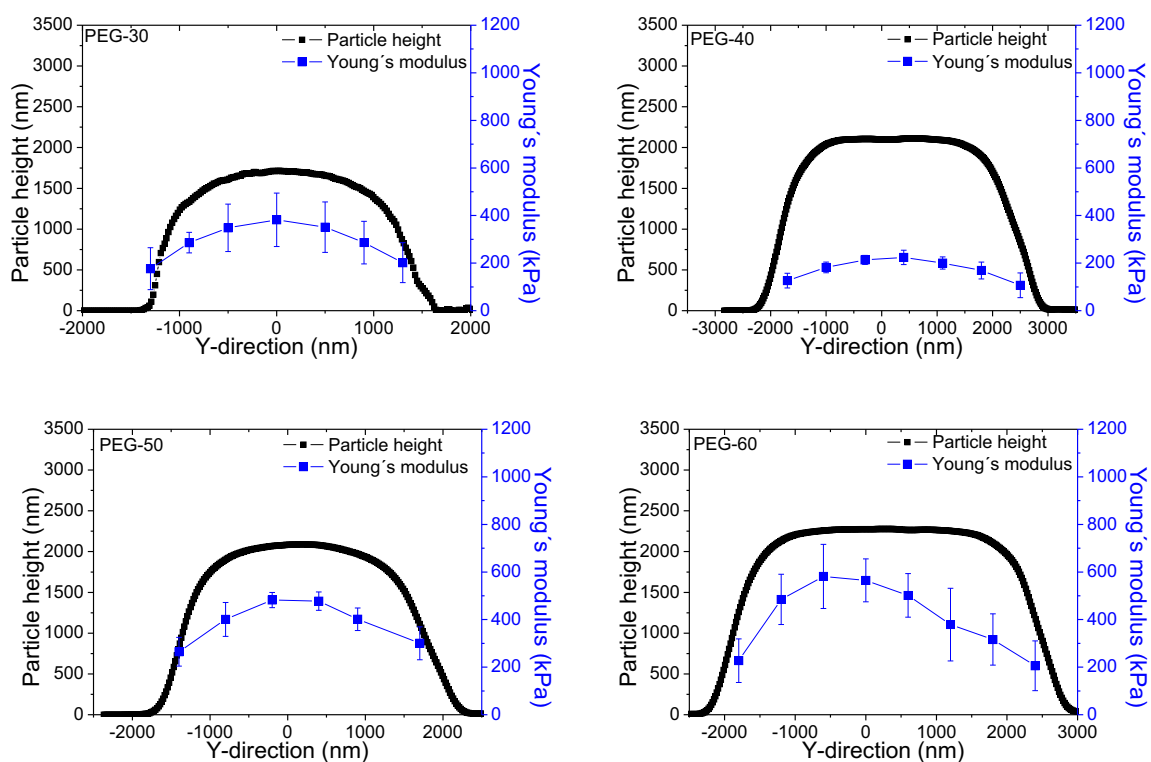


Figure 5.9: Young's modulus vs the particle cross section for the PEG particles, which differ in the PEG content.

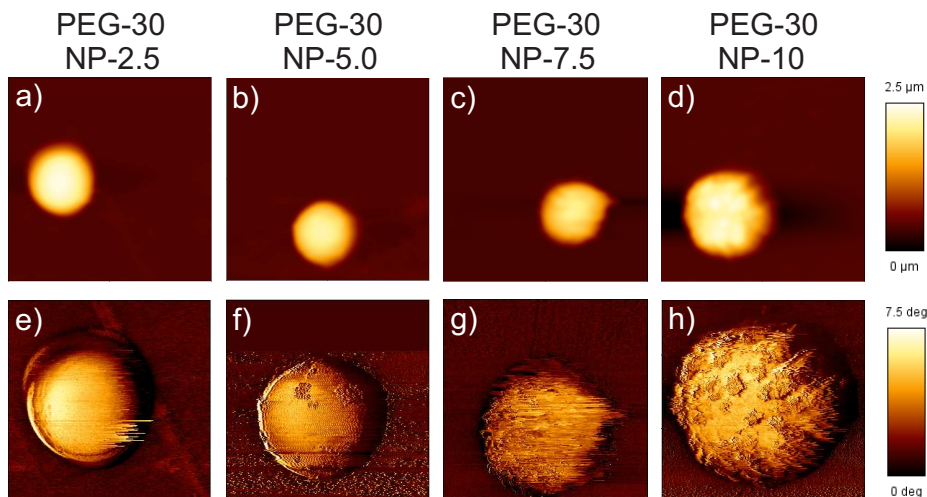


Figure 5.10: PEG-30 particles with different polystyrene content. Top row: AFM height images Scan size: $10 \times 10 \mu\text{m}^2$. Bottom row: AFM phase images Scan size: $4.5 \times 4.5 \mu\text{m}^2$.

particle shape, the AFM phase images offer additional information about the incorporated nanoparticles.

PEG-30-NP-2.5 particles show a homogeneous particle shape in the height and phase images. An increase in the polystyrene content in the particles leads to a change in the particle shape, which becomes more inhomogeneous. Phase images of PEG-30-NP-5.0 particles (Figure 5.10f) as well as PEG-30-NP-7.5 particles (Figure 5.10g) exhibit particle domains, which differ from the remaining particle softness. The inhomogeneous particle shape becomes more pronounced at higher polystyrene nanoparticles as shown for PEG-30-NP-10 particles (Figure 5.10h). The observed domains in the phase images indicate cluster formation of the polystyrene nanoparticles, which are stiffer compared to the surrounding polymer network.

To study the influence of polystyrene nanoparticles on the particle stiffness, force measurements were performed across the particle. Both the particle cross section as well as the force curves was extracted from the particle centre perpendicular to the scan direction to avoid any scan effects. Figure 5.11 shows the particles cross section and the Young's modulus of the particular particles. PEG-30-NP-2.5 particles show an uniform particle stiffness along the particle cross section. The same trend can be observed for PEG-30-NP-5 particles. The Young's modulus does not change with the particle shape. Both particle types, PEG-30-NP-2.5 and PEG-30-NP-5, exhibit the same particle stiffness of around 200 kPa, which equals the particle stiffness of PNIPAM particles. An increase in the nanoparticle content results in a increase in the particle stiffness as well as heterogeneous particle stiffness as shown for PEG-30-NP-

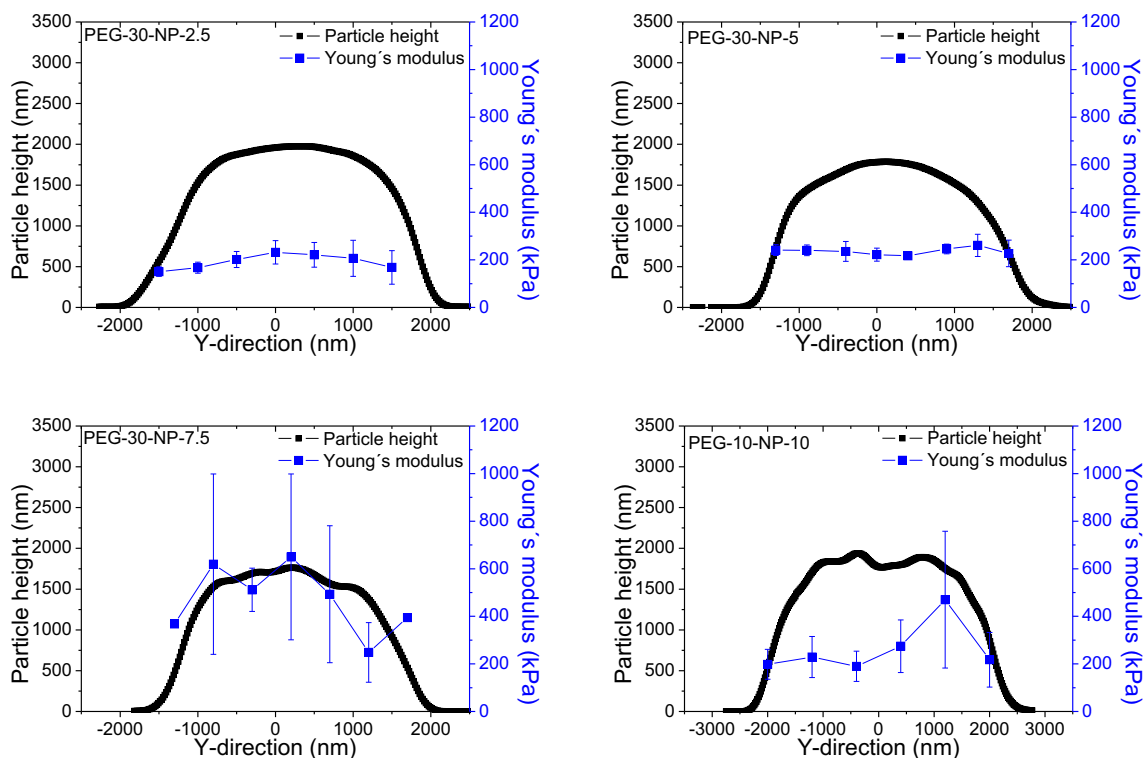


Figure 5.11: Young's modulus vs. the particle cross section for the PEG-30 particles with different polystyrene content.

7.5 particles. A further increase in polystyrene content to 10 wt-% leads again to a uniformly distributed Young's modulus.

5.3.2 Discussion

All PEG particles, pure PEG and PEG with nanoparticles, do not follow a specific trend in particle size. Neither a higher PEG content nor varying polystyrene content influences the particle size leading to random size distribution. However, an increase in the PEG content leads to an increase in the particle stiffness from around 400 kPa for PEG-30 particles to around 600 kPa for PEG-60 particles. An increase in the PEG content leads to a more cross-linked and compact particle resulting in particle stiffening¹¹². Furthermore, the possibility arises to form intramolecular cross-links between the polymer chains due to H-bonds, which would also lead to particle stiffening¹¹³. It seems that such intramolecular connections are more pronounced at high PEG concentrations than for low ones. For all PEG particles the same trend can be observed, that the highest Young's modulus is located in the particle centre and decreases towards the particle periphery. Such behaviour can be related

to the cross-linker density of the PEG particles as observed for PNIPAM microgels¹¹⁰. The particles display a particle core and shell region. The particle core can be more cross-linked as the particle shell, which would lead to a stiffer particle centre. The less cross-linked particle shell instead would be softer leading to a Young's modulus reduction.

The obtained results for PEG-30-NP-X (X=2.5, 5, 7.5 and 10) can be traced back to the incorporated polystyrene nanoparticles. At low polystyrene content, the incorporated nanoparticles, which are randomly distributed, within the particles play a minor role in the particles stiffness. The particle stiffness for PEG-30-NP-2.5 and PEG-30-NP-5 particles is in the same order of magnitude. Furthermore, no decrease in the particle stiffness towards the particle periphery can be observed. It seems, that the nanoparticles serve as an extra cross-linker within the particles. Hence, the polymer network becomes more homogeneous leading to an uniform stiffness along the particles. The situation changes with increasing the polystyrene content. At a content of 7.5 wt-%, a strong polystyrene cluster formation can be observed in the phase images. Furthermore, the particle stiffness increases tremendously indicating a strong impact of the polystyrene particles on the particle behaviour. In case of PEG-30-NP-10, again the phase images show cluster formation. However, a decrease in the stiffness takes places assuming that higher polystyrene content leads a restricted but soft polymer network.

5.3.3 Conclusion

In this section, a series of polyethyleneglycol particles (PEG) obtained from Princeton university have been studied. The mechanical properties of these particles were determined via AFM indentation experiments.

The particle stiffness of PEG particles can be controlled by either the PEG content or the incorporation of polystyrene particles. An increase in the PEG content leads to an increase in the particle stiffness due to the formation of H-bonds between the PEG segments. The increase in the PEG leads also to a stiffer particle centre and a decrease in the stiffness towards the periphery assuming a stronger core-shell like structure at higher PEG contents. The incorporation of polystyrene particles leads to a decrease in the particle stiffness compared to the one without polystyrene particles. Furthermore, the particle stiffness keeps constant along the particle cross section. This indicates a homogeneous distribution of polystyrene particles within the particles. However, PEG-30-NP-7.5 show larger particle stiffness compared to the other PEG-

30-NP particles. This gives a hint that the incorporation of the polystyrene nanoparticles was more effective for PEG-30-NP-7.5 than for the other ones. But this behaviour is not fully understood and is still under investigation. The nanoparticles apparently confine the polymer network due to extra cross-links between polymer and nanoparticles. With increasing the polystyrene concentration, small cluster of these polystyrene particles have been observed in the phase image, which confirms the assumption that these cluster formation leads to homogeneous particle stiffness.

5.4 Polyglycerol (PG) based microgels

5.4.1 Results

This section deals with polyglycerol particles (PG) synthesised by Dirk Steinhilber from the Haag group at the Freie Universität Berlin. The focus on these samples is the tuning of the particle stiffness. The aim was to synthesis soft particles for medical applications since it is assumed that softer particles are more efficient for anti-cancer drug delivery systems^{114,115}.

Two samples were synthesised for this purpose. Both samples consist of dendritic polyglycerol dPG sub-compartments. These dPG sub-compartments were cross-linked in different ways. In case of the first sample, called PG-1, these dPG sub-compartments were cross-linked with steric sophisticated ether groups as cross-linker, while in the second sample, called PG-2, dPG sub-compartments are connected with a linearly cross-linker containing an acetal group.

Figure 5.12 shows the AFM images for PG-1 and PG-2 particles. It should be noted that the scale bars differ for both images, due to the large difference in the particle size of PG-1 and PG-2. PG-1 particles show a larger particle size compared the PG-2 particles. It seems, that PG-1 particles exhibit a stiff polymer network resulting in larger particles. In contrast to PG-1, PG-2 particles, which mainly consist of more linear cross-linked polymer segments, are more flexible. Thus, PG-2 particles trend to flatten on the surface leading to a smaller particle size.

To confirm the softening of the particles stiffness, force measurements were performed for both particle types. Figure 5.13 shows the Young's modulus against the particle cross section for PG-1 and PG-2 particles, respectively. The largest Young's modulus for both particle types is located in the particle centre and decreases towards the particle periphery as observed before for

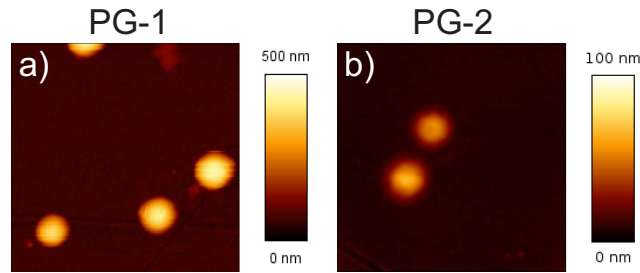


Figure 5.12: AFM images for PG-1 (left) and PG-2 particles (right). The scale bar differ for both images, due to the large size differences between the particles. Scan size: $5 \times 5 \mu\text{m}^2$.

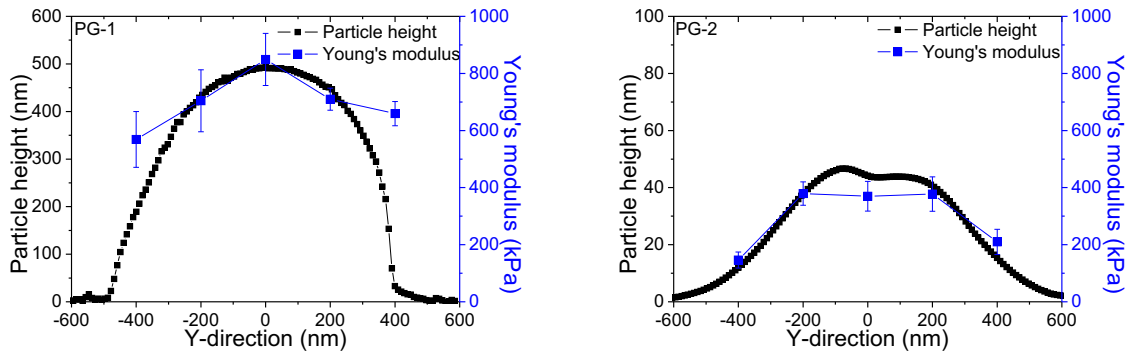


Figure 5.13: Young's modulus vs the particle cross section for the PG-1 particles (left) and PG-2 (right).

PNIPAM particles in the first part of the chapter and literature³⁶. PG-2 particles exhibit only half the particle stiffness of PG-1 particles.

5.4.2 Discussion

The obtained results are remarkable but expected. PG-1 particles have the largest particle size and particles stiffness, due to the inflexible nature of the polymer network. Such compact nature of the particles is a direct result of the particle stiffening. The stiff nature of the particles apparently arises from the steric cross-linker. Hence, the particle is unable to flatten. Furthermore, the polymer segments might more restricted and less mobile. However, PG-

2 particles exhibit a more flexible polymer network, which is able to flatten on the surface leading to small particles in the adsorbed state. The flexible nature of the PG-2 particles leads also to a particle softening. The decrease of the particle stiffness towards the particle periphery for both PG-1 and PG-2 particles indicates a core-shell-like particle structure with a higher cross-linked particle interior and the less dense particle periphery.

5.4.3 Conclusion

In this section, a series of polyglycerol particles (PG) obtained from Freie Universität Berlin have been studied. The mechanical properties of these particles were determined via AFM indentation experiments.

Two types of polyglycerol particle with different chemical bonds were studied. In first batch, particles consist of subparticles cross-linked with ether units have been studied. The second batch, particles consisting of subparticles connected with a more linearly acetal cross-linker. The ether connected particle leads to larger and stiffer particles due to the steric nature of the cross-linker. Particles with the more linearly cross-linker results in smaller but softer particles due to the flexible nature of the acetal cross-linker, which is able to flatten at the surface.

5.5 Outlook

The PNIPAM particles provide a great potential for further investigations. On the one hand, the salt effect on the mechanical properties for such PNIPAM particles can be studied. The question arises what will happen if the particle charges are screened by counterions. This leads directly to another question. The size of AAc as well as AAA containing microgels can be tuned by varying the pH. The particle stiffness should be investigated at various pH. Here, the particle should be uncharged (low pH), moderate charged (pH around 7) and highly charged (high pH). The stiffness should decrease with increasing the pH, due to the increased electrostatic repulsion within the particles. The third aim would be the investigation of co-monomers with even longer alkyl chains to get a better understanding of the interplay between electrostatic repulsion and the hydrophobic attraction. With the focus on applicable relevance in terms of coatings, it is important to understand the mechanical properties of particle monolayers. This needs information about the particle stiffness of two overlapping particles.

Chapter 6

The impact of co-non-solvency effect on PNIPAM based microgels at an interface

This chapter contains parts of the publication: The impact of the co-non-solvency effect on PNIPAM microgels at interfaces *Colloid and Polymer Science*, (2014), 292, 2439-2452.

6.1 Introduction

Microgels based on PNIPAM serve as excellent enzyme carrier or sensor systems^{8,102}. For such applications it is fundamental to understand the microgel behaviour in water/organic solvent mixture as well as in pure organic solvents.

PNIPAM based microgels exhibit an excellent swelling ability in pure ethanol or pure water^{39,41,64}. The microgels are highly swollen in pure water or pure organic solvent, due to the hydrogen bonds between the solvent and the polymer backbone. Therefore, pure water or pure organic solvent serve as good solvents for microgels. However, a solution of two "good" solvents, water and organic solvent (EtOH, iPr and THF) turns into a "poor" solvent resulting in a miscibility gap^{116,117}. At low organic solvent concentration, water molecules form a clathrate structure around the organic solvent molecules⁶⁰. This leads to a less hydrated polymer network and stronger polymer-polymer bonds (hydrophobic interactions between the isopropylgroups) in the particle interior leading to particle collapse^{63,118}. At higher organic solvent concentration, water molecules are not able to surround the organic solvent and the clathrate structure breaks up⁶⁰. Thus, free and more movable organic solvent

molecules are able to interact with the polymer network leading to a reswelling of the particle^{66,119}. Beside the clathrate model, the assumption of the competitive absorption seems also to be a reasonable explanation of the the co-non-solvency effect^{42,61}. In this model, both solvents (water and organic solvent) compete to form H-bonds with the polymer network. However, this model neglects the solvent-solvent interaction.

For applications e.g. as sensors it is not only important to understand the bulk behaviour but also to understand the microgel properties at surfaces. So far the understand about the co-non-solvency effect at surfaces is limited and the explanations, which are given, are poor. Heppner *et al.* described the co-non-solvency behaviour of adsorbed PNIPAM particles via the VPTT at different water/methanol mixtures⁴³. The particles have been placed between two gold layers like in an etalon. They used reflectance spectroscopy to follow the VPT. The VPT of the adsorbed particles was compared to the VPT in solution. It turned out, that the VPTT of the particles shifts to lower temperatures with increasing organic solvent content and that the minimum in VPTT was at 65 % methanol for both in solution and in the etalon. Also the values of the VPTT were the same. In this context, Heppner *et al.* did not detect any effect of the geometrical confinement on the co-non-solvency behaviour.

This chapter deals with the co-non-solvency phenomenon of microgels. It clarifies the property differences between bulk and surface behaviour. Microgels containing allyl acetic acid as co-monomer were synthesized. The co-monomer concentration was fixed to 0 % (PNIPAM-5) and 5 % (AAA-5), respectively. Ethanol (EtOH), iso-propanol (iPr) and tetrahydrofuran (THF) were used as organic solvents to induce the co-non-solvency effect. These organic solvents differ in their polarity and molecular size, which allows studying the swelling/shrinking behaviour of the microgels depending on the chemical nature of the used organic solvents. Furthermore, the swelling ability of the synthesized particles was studied at the surface.

6.2 Results

6.2.1 Co-non-solvency effect of microgel particles in bulk

Figure 6.1a) shows the hydrodynamic radius and Figure 6.1c) shows the particle volume (calculated from the hydrodynamic radius) of PNIPAM-5 as a function of the organic solvent composition at 20 °C. The particle radius

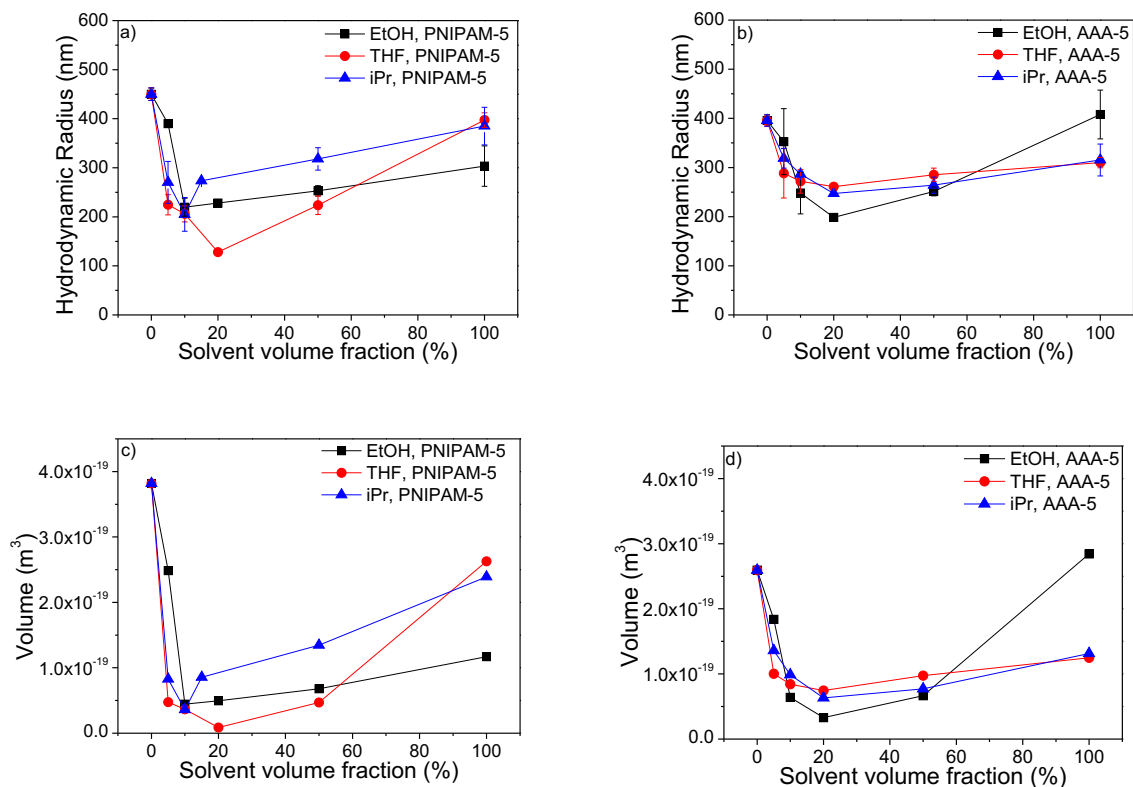


Figure 6.1: Hydrodynamic radius for PNIPAM-5 (a) and AAA-5 (b) measured with DLS and the calculated particle volume for PNIPAM-5 (c) and AAA-5 (d) as a function of different water-organic solvent composition.

in the swollen state (pure water) is about 450 nm. The addition of organic solvent leads to a decrease in the particle size. A minimum appears at a volume fraction of 10 % EtOH ($R_h = 230$ nm) and of 10 % iPr ($R_h = 210$ nm), while the minimum shifts to 20 % for THF ($R_h = 125$ nm). A further increase in the solvent content results in a reswelling of the particles.

In general, AAA-5 particles show a similar behaviour as PNIPAM-5 particles in the hydrodynamic radius (Figure 6.1b) and calculated particle volume (Figure 6.1d). Again, the particles are largest in pure water with a particle size of about 400 nm. With increasing the organic solvent content a decrease in the particle size occurs but AAA-5 particles reach their minimum in size at a solvent content of 20 % for all three solvents. Further increase in solvent content leads to a particle reswelling. As observed for PNIPAM particles, AAA-5 offers smaller particle sizes in pure organic solvent than in pure water. Consequently, a co-non-solvency effect can be observed for PNIPAM-5 and AAA-5, respectively.

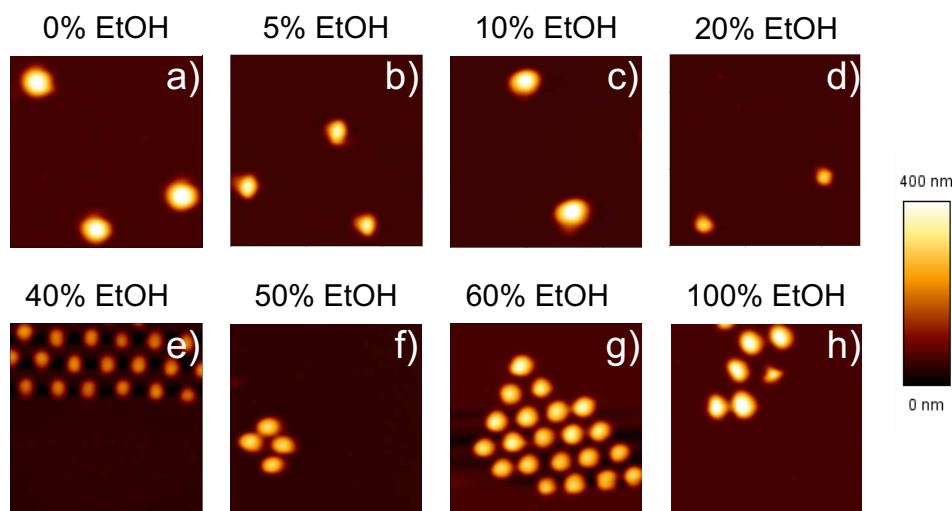


Figure 6.2: AFM-images for PNIPAM-5 in liquid state at the surface for different water-EtOH composition. Scan area: $5 \times 5 \mu\text{m}^2$.

6.2.2 Co-non-solvency effect of microgel particles after adsorption

In order to study the co-non-solvency effect at the surface, the AFM-images of the particles were recorded in the liquid state. All particles were spin coated from the corresponding water-organic solvent mixtures. Figure 6.2 represents the AFM-images of PNIPAM-5 as a function of different water-EtOH solutions. PNIPAM-5 microgels exhibit its most extended dimension in pure water, due to the formation of hydrogen bonds between the solvent and the polymer network. The addition of ethanol leads to a particle shrinking with its particle minimum at 40 % EtOH. Further increase in the EtOH content results in a particle reswelling. The same behaviour for PNIPAM-5 particles can be observed in water-iPr solutions (Figure A.3) and water-THF solutions (Figure A.4), respectively.

To get a better understanding of the particle behaviour at the surface, the PNIPAM-5 particle cross sections from AFM-images were extracted for all three water-organic solvent mixtures (Figure A.5). As observed in the AFM images, particles in pure water exhibit the largest dimension. The addition of organic solvent causes a decrease in lateral as well as in vertical direction for all water-organic solvent mixtures. The strongest lateral particle shrinking appears from in pure water to a organic solvent content of 5 %. Further increase in the organic solvent has less impact in the lateral shrinking. On the other hand the decrease in the particle height takes place at higher organic solvent content. At a certain mixture composition is reached a particle reswelling

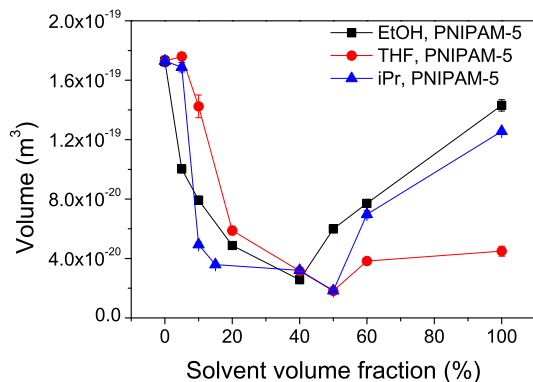


Figure 6.3: Particle volume for PNIPAM-5 in liquid state at the surface as a function of different water-organic solvent composition. For data points with invisible error bars, the error bars are smaller than the symbol size.

takes places. The particle reswelling occurs mainly in vertical direction, while the lateral reswelling plays a minor role.

The particle volume was calculated from the particle cross sections to determine the exact particle minimum. Figure 6.3 shows the particle volume of PNIPAM-5 particles as a function of the three water-organic solvent mixtures. PNIPAM-5 particles have the largest particle volume in pure water. The addition of organic solvent causes a decrease in particle volume until a minimum in the particle volume is reached. The impact of EtOH and iPr on the particle volume of PNIPAM-5 particles is more pronounced than for THF. At small EtOH and iPr concentration the particle deswells stronger than for low THF concentrations. The smallest volume for PNIPAM-5 particles in water-EtOH appears at a solvent content of 40 % and at 50 % in both water-iPr and water-THF solutions. Furthermore, particle reswelling occurs at higher solvent concentrations. The particle volume in the corresponding organic solvents is smaller than in pure water.

To understand the particle collapse, the changes in lateral and vertical direction were extracted from the particle cross sections. Figure 6.4 shows the swelling ratio of the particle height and particle width for PNIPAM-5 particle at different water-organic solvent mixture with respect to the particle height and width taken in pure water. At low organic solvent content, the particle shrinking is mainly affected by a strong decrease in the particle width for all water-organic solvent mixtures. Further increase in the organic solvent leads to a pronounced decrease in the particle height, while the particle width has less impact on the particle shrinking. The particle reswelling process

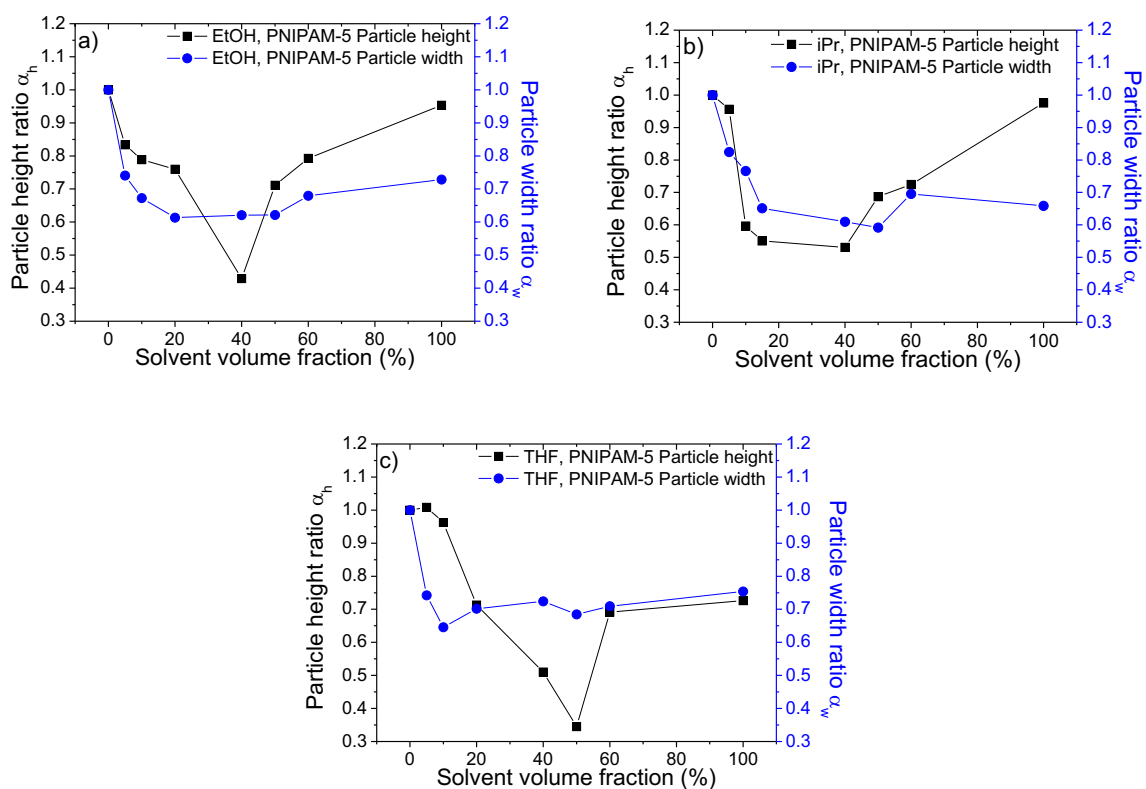


Figure 6.4: Particle height and particle width ratio (with respect to the corresponding values spin coated from pure water) of PNIPAM-5 spin coated from different a) water-EtOH b) water-iPr and c) water-THF mixtures, respectively.

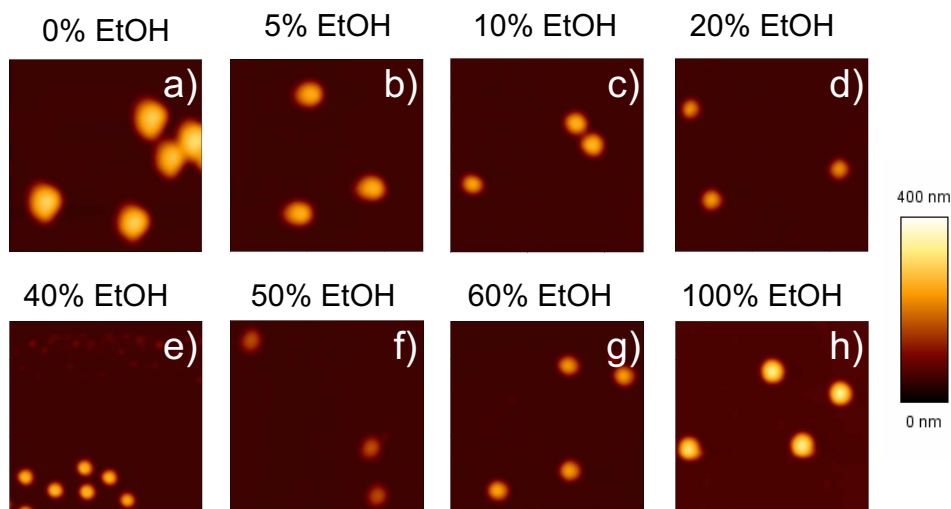


Figure 6.5: AFM-images for AAA-5 in liquid state at the surface for different water-EtOH composition. Scan area: $5 \times 5 \mu\text{m}^2$.

mainly occurs in vertical direction. The particle width in contrast exhibits a small contribution in the particle reswelling.

For AAA-5 particles qualitatively the same behaviour can be observed at the surface. Figure 6.5 represents the AFM-images of AAA-5 particles against different water-EtOH mixtures, while the AFM-images for water-iPr (Figure A.6) and water-THF solutions (Figure A.7) can be found in the Appendix. For all three water-organic solvent solutions a co-non-solvency effect for AAA-5 particle can be observed. The particles are highly swollen in pure water and shrink after the addition of organic solvent. The smallest particle dimension occurs at a solvent content of 50 % for EtOH and THF, respectively. It shifts to a organic solvent content of 40 % for water-iPr mixtures. At higher solvent contents the particles start to reswell. As for PNIPAM-5 particles, the AAA-5 particles are smaller in pure solvents than in pure water.

The AAA-5 particle cross sections (Figure A.8) show the impact of the organic solvents on the particle height and particle width. AAA-5 particles exhibit the largest particles in pure water. The addition of organic solvent leads to a decrease in the particle height and particle width for all water-organic solvent mixtures. At a certain organic solvent content the AAA-5 particles start to reswell, which mainly takes places in vertical direction as observed for PNIPAM-5 particles. The particle cross sections were used to calculate the particle volume for the exact determination of the particle minimum.

Figure 6.6 shows the particle volume for AAA-5 as a function of the dif-

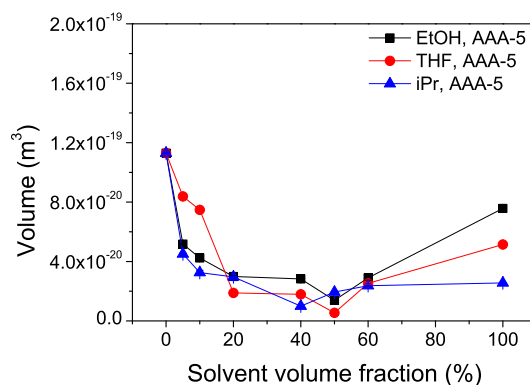


Figure 6.6: Particle volume for AAA-5 in liquid state at the surface as a function of different water-organic solvent composition. For data points with invisible error bars, the error bars are smaller than the symbol size.

ferent water-organic solvent compositions. Again, the particles show their largest particle volume in pure water as observed before for the particle cross sections. The addition of organic solvent leads to a decrease in the particle volume. EtOH and iPr have high impact in the particle volume decrease. In contrast, low THF concentration causes a less pronounced decrease in the particle volume. The smallest particle volume for AAA-5 in water-EtOH and water-THF solution is determined at a solvent content of 50 %. It is 40 % for water-iPr mixtures. Further increase in the solvent concentration leads to a particle reswelling as observed before for PNIPAM-5 particles. Again, AAA-5 particles are smaller in the pure organic solvents as in pure water.

Figure 6.7 shows the contribution of the particle height ratio and particle width ratio (with respect to the particle height and width in pure water) on the shrinking process of the AAA-5 particles as a function of the different water-organic solvent mixtures. Again at low organic solvent content (5 %), the particle width shows a strong decrease for all water-organic solvent solutions, while the particle height plays a minor role in the particle shrinking. The decrease in the particle height dominates the particle shrinking at higher organic solvent content. The particle reswelling process is strongly influenced by the particle height, while the lateral swelling is less pronounced. This behaviour can be observed for all three water-organic solvent compositions.

6.2.3 Effect of spin coating conditions on the particle deswelling

As shown in the bulk measurements, the particles experience a co-non-solvency effect in water-organic solvent mixtures. So far, the particles have been spin

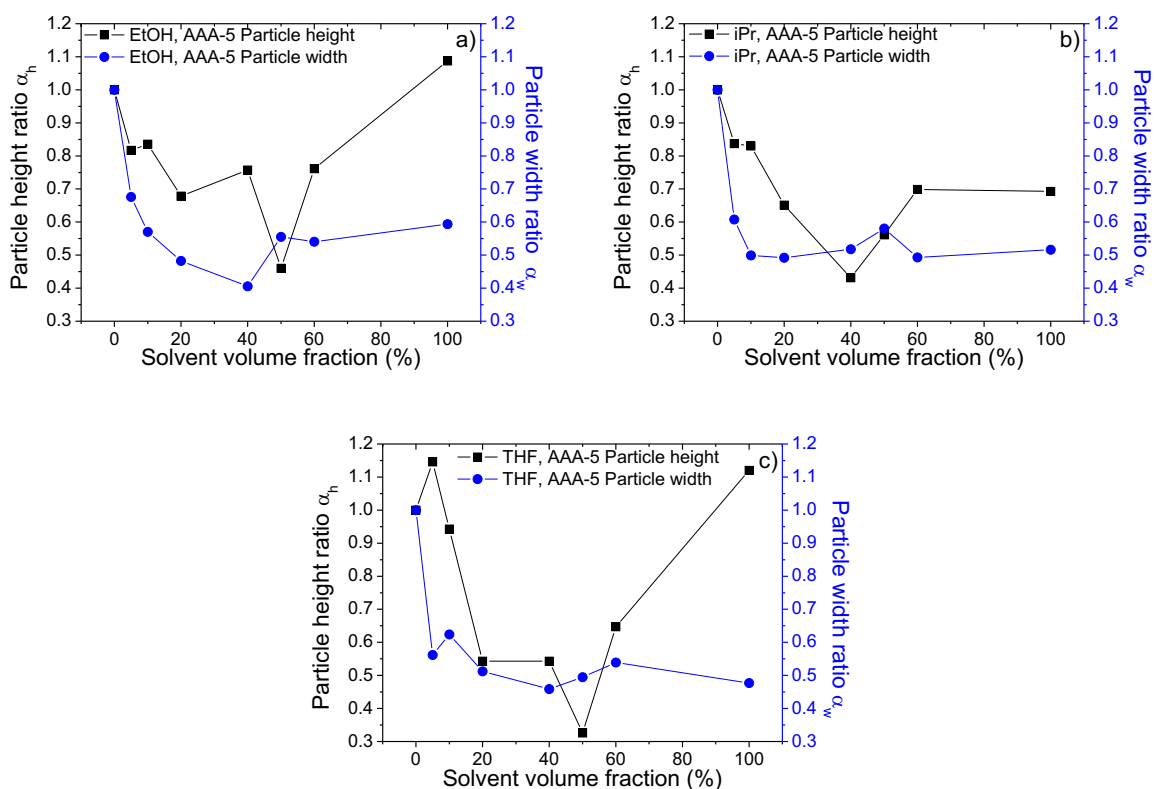


Figure 6.7: Particle height and particle width ratio (with respect to the corresponding values spin coated from pure water) of AAA-5 spin coated from different a) water-EtOH b) water-iPr and c) water-THF mixtures, respectively.

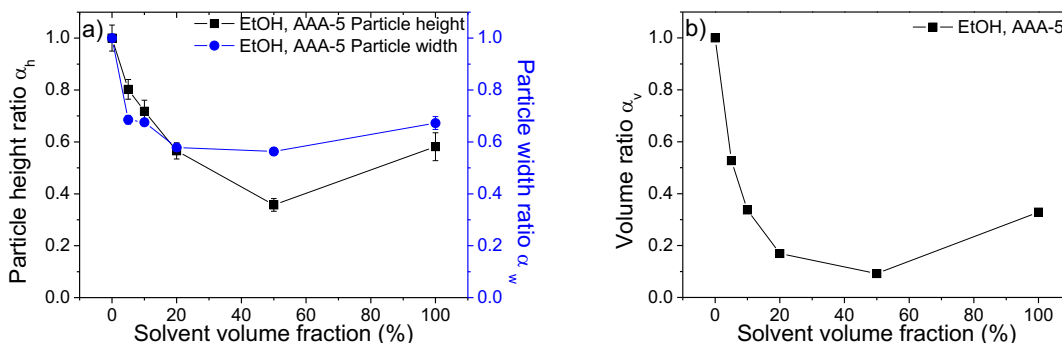


Figure 6.8: AAA-5 particles in different water-EtOH mixtures: a) Particle height as well as particle width, b) particle volume. For data points with invisible error bars, the error bars are smaller than the symbol size.

coated from the corresponding water-organic solvent mixtures leading to different pre-conditions of the particles before reimmerse for AFM studies. In order to fix the pre-conditions, the particles were spin coated from pure water and measured in different water-EtOH mixtures.

The AFM-images for AAA-5 as a function of water-EtOH solutions are shown in Figure A.9. AAA-5 particles are highly swollen in pure water and exhibit their largest size. The particle size decreases with increasing the EtOH content in the mixture. The minimum is located at an EtOH concentration of 50 %. Further increase in the solvent concentration leads to a particle reswelling. It is worth to note, that the particle pattern does not change and that particle desorption does not take place.

To understand the shrinking process the particle height as well as the particle width were extracted from the AFM-images. Figure 6.8a) shows the difference in the particle height and width in pure water and different water-EtOH mixtures of AAA-5 particles spin coated from water normalized with respect to the particle height and width measured in pure water. The particles shrink in lateral and vertical direction. At low EtOH concentrations (5 %) the particle width changes from $\alpha_w=1$ to $\alpha_w=0.7$, while the particle height decreases from $\alpha_h=1$ to $\alpha_h=0.8$. Further increase in the ethanol concentration leads to a marginal change in the particle width. On the other hand, the particle height shrinks tremendously. In pure ethanol the particles reswell mainly occurs in vertical direction, while a marginal reswelling in lateral direction takes place.

Figure 6.8b) shows the calculated particle volume ratio (normalized with respect to the particle volume in pure water) of AAA-5 particles. As observed

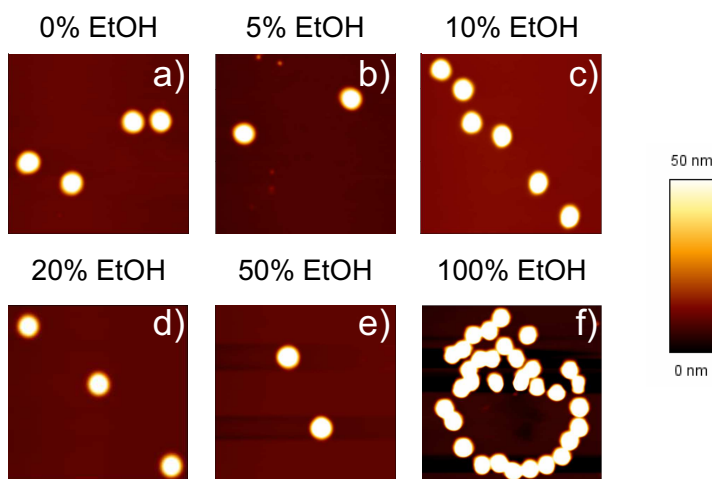


Figure 6.9: AFM-images of PNIPAM-5 in ambient conditions spin coated from different water-EtOH compositions. Scan area: $5 \times 5 \mu\text{m}^2$.

for the AFM-images, the particles offer the largest particle volume in pure water and decreases to a minimum of 50 % EtOH. In pure ethanol the particles start to reswell. Thus, the particles clearly show a co-non-solvency effect.

6.2.4 Adsorbed microgel particles in ambient conditions

After the spin coating process, the particles are in ambient conditions. For AFM studies in liquid the particle have been reswelled in the respective solvent. However, to study the impact of the drying process during spin coating on the particle behaviour, the particles were investigated under ambient conditions. In addition, the swelling ability of the particles from ambient conditions to the liquid state will be quantified.

PNIPAM microgel particles

In order to understand the swelling ability of these microgel at surfaces it is essential to study the particle behaviour in ambient condition. The particles have been spin coated from the particular water-organic solvent composition. Figure 6.9 shows AFM-images of PNIPAM-5 particle in ambient conditions spin coated from different water-EtOH compositions. The particles are smallest after spin coating from pure water and increases with increasing the organic solvent content during spin coating. The same particle behaviour can be observed for water-iPr (Figure A.10) and water-THF (Figure A.11) mixtures.

Cross sections were extracted from the corresponding AFM-images to clarify the changes in lateral and vertical direction. Figure A.12 shows the

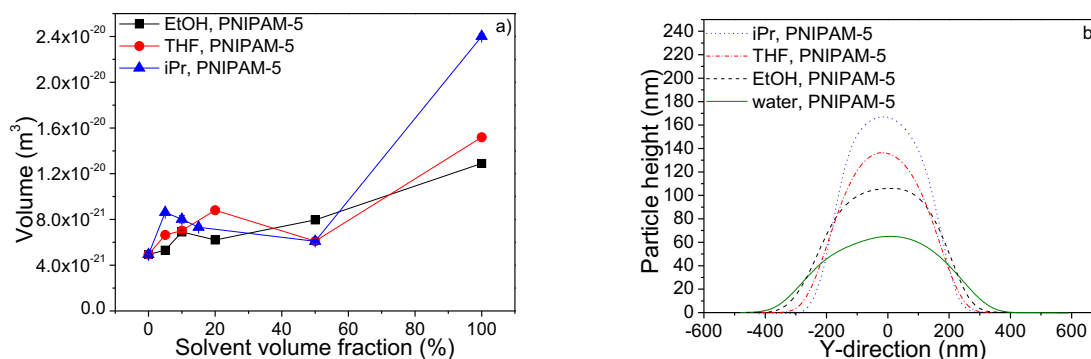


Figure 6.10: PNIPAM-5 in ambient conditions after spin coating: a) Particle volume for different water-organic solvent compositions. b) Particle cross sections spin coated from pure solvent. The error bars are within the symbols.

particle cross sections for PNIPAM-5 particles as a function of the different water-organic solvent mixtures. For all three water-organic solvent mixtures, the particle height of PNIPAM-5 increases with increasing the organic solvent content. The particle width in contrast increases at low organic solvent content and show a decrease with further addition of organic solvent.

The particle volume was calculated and is shown in Figure 6.10a). PNIPAM-5 particles show their smallest particle volume after spin coated from pure water. The particle volume increases dramatically for microgels spin coated from the pure solvents (water, EtOH, iPr and THF, respectively). The largest particle volume is obtained in iPr. It is smaller in pure THF and pure EtOH.

Figure 6.10b) represents the cross sections for the PNIPAM-5 spin coated from pure water and the pure organic solvents in ambient conditions. Particles, which were spin coated from pure water, offers the smallest particle height. The particle height increases for pure solvents in the order of $\text{EtOH} < \text{THF} < \text{iPr}$. Furthermore, the particles show differences in the lateral dimension. Particles spin coated from iPr and THF show a stronger decrease in the lateral direction as particles, which were spin coated from pure water or EtOH.

PNIPAM-co-AAA microgel particles

Figure 6.11 shows the AFM-images of AAA-5 particles in ambient conditions in dependence of the water-EtOH composition. Thereby, AAA-5 particles show the same behaviour as PNIPAM-5 particles. Particles, spin coated from pure water, offer the smallest particle size. With increasing the EtOH content, the particle size increases in vertical direction. AAA-5 particles show no

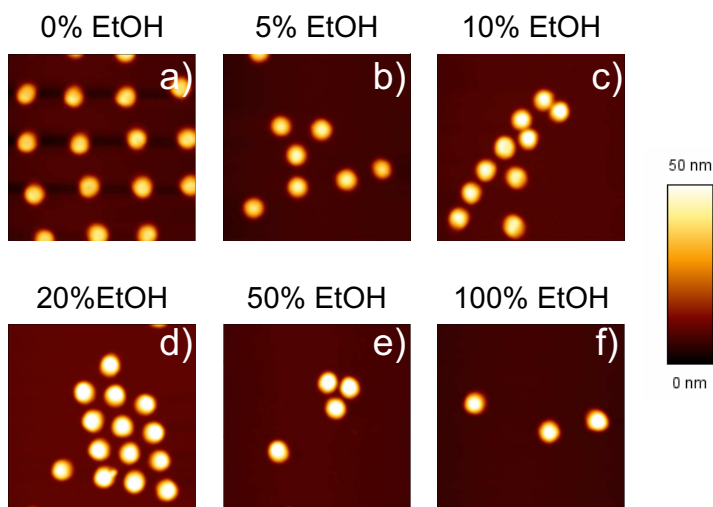


Figure 6.11: AFM-images for AAA-5 in ambient conditions spin coated from different water-EtOH composition. Scan area: $5 \times 5 \mu\text{m}^2$.

minimum in particle size. Consequently, no co-non-solvency effect can be observed in ambient conditions. The same behaviour can be observed for AAA-5 particles spin coated from water-iPr and water-THF solutions as shown in Figure A.13 and Figure A.14.

Figure A.15 shows the particle cross sections of AAA-5 particles for the three water-organic solvent mixtures. In all three water-organic solvent mixtures, the particle cross sections show an increase in the particle height with increasing the organic solvent content. The particle width in contrast increases not as pronounced as for the particle height with increasing the organic solvent content.

Figure 6.12a) depicts the volume for particles spin coated from the particular water-solvent compositions. AAA-5 exhibits its smallest particle volume in pure water. With increasing the solvent content the particle volume increases. The change in the particle volume occurs in the order of $\text{EtOH} < \text{iPr} < \text{THF}$.

Figure 6.12b) compares the cross sections for AAA-5 particle spin coated from the pure solvents (water, EtOH, iPr and THF) and shows the increase in the particle volume. The change in the particle volume mainly takes place in vertical direction. The particle width in contrast plays a minor role in the volume increase.

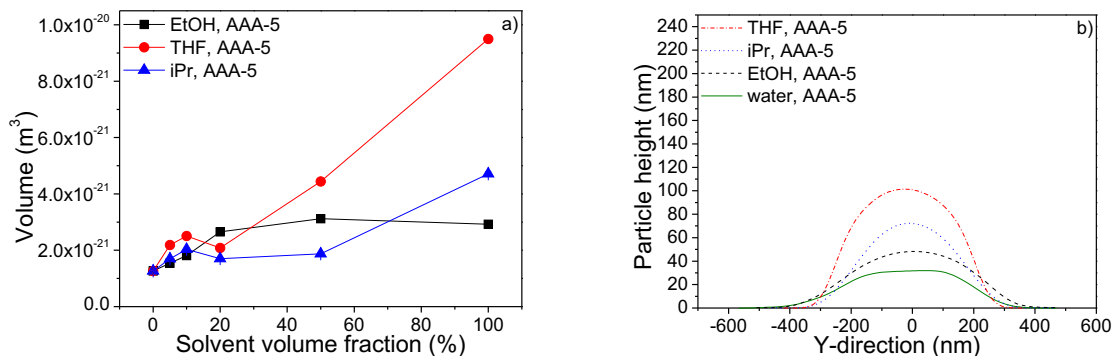


Figure 6.12: AAA-5 in ambient conditions: a) Particle volume different water-organic solvent compositions. b) particle cross sections spin coated from pure solvent. The error bars are within the symbols.

6.2.5 Swelling ability of adsorbed PNIPAM-5 and AAA-5 particles

The swelling ability can be tuned by parameters such as cross-linker content as well as co-monomer content. The particle swelling ratio f_w from ambient conditions to liquid state serves as an important parameter to understand the impact of these parameters on the microgel-to-surface interaction.

The particle width in the corresponding water-organic solvent mixture was normalized to the particle width in ambient conditions as follows:

$$f_w = \frac{w(\text{liquid})}{w(\text{ambient})} \quad (6.1)$$

where $w(\text{liquid})$ is the particle width in liquid state, $w(\text{ambient})$ represents the particle width in ambient conditions, while f_w is the particle width ratio between the liquid and ambient state. In case of a large f_w , the microgel-to-surface interaction is weak, while small f_w indicates less particle swelling and consequently strong microgel-to-surface interaction.

Figure 6.13a) shows the particle width ratio for PNIPAM-5 in different water-organic solvent mixtures. PNIPAM-5 particles exhibit a good swelling ability in pure water ($f_w=1.3$). The swelling ratio decreases with the addition of organic solvent and reaches a minimum at 50 % organic solvent content in all three water-organic solvent mixtures. The particles show an increase in the swelling ability in all pure organic solvents.

The swelling ratios of AAA-5 particles in the three water-organic solvent mixtures is shown in Figure 6.13b). AAA-5 particles shows a stronger swelling ability ($f_w=1.8$) as PNIPAM-5 particles ($f_w=1.3$) in pure water. Again, the addition of organic solvent leads to a decrease in the swelling ability for AAA-

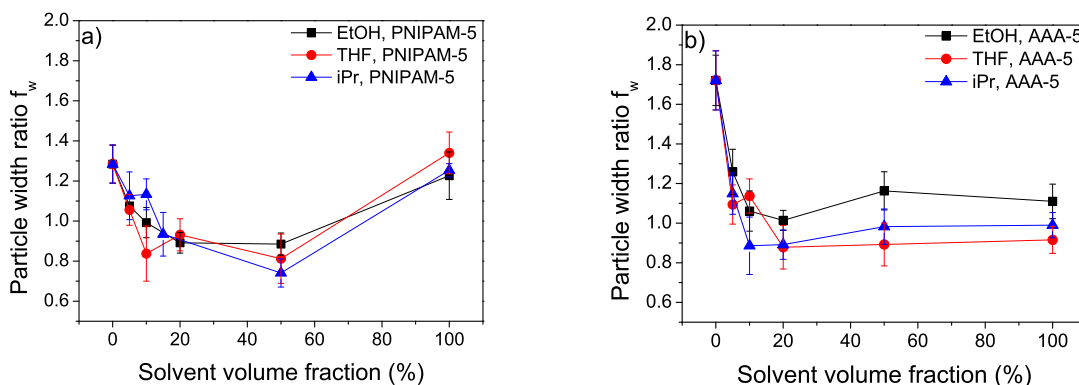


Figure 6.13: Swelling ratio of microgel particles in lateral direction spin coated from different water-organic solvent mixtures for: (a) PNIPAM-5 and (b) AAA-5.

5 particles from $f_w=1.8$ to about $f_w=1.0$ at 20% solvent content. The particle width ratio does not change significant with further increase in the organic solvent content.

6.3 Discussion

Table 6.1: Column two to four show the solvent content at which the particle minimum appears for bulk measurements, while column five to seven show the solvent content at which the particle minimum takes place at the surface.

Microgel type	Bulk			Surface		
	EtOH	iPr	THF	EtOH	iPr	THF
PNIPAM-5	10 %	10 %	20 %	40 %	50 %	50 %
AAA-5	20 %	20 %	20 %	50 %	40 %	50 %

The discussion will be divided into two parts. The first part of the paper compares the co-non-solvency effect for particles in bulk and at the surface, while the second part highlights the shrinking/reswelling behaviour of the particles in detail at the surface.

Shift in the particle size minimum from bulk to adsorbed particles

Particles at the surface have been spin coated from and reimmersed in the corresponding water-organic solvent mixtures, while particles for DLS measurements have been dissolved in the corresponding water-organic solvent mixtures. Table 6.1 summarizes the obtained results for the particles in bulk as

well as at the surface. Both particle types, PNIPAM-5 and AAA-5, show a clear co-non-solvency effect in bulk and at the surface. The size minimum as well as the increase in the correlation length for particles in bulk takes place at a solvent content of 10-20 %. This behaviour is consistent with the literature^{38,41,65}. On the other hand, the size minimum for adsorbed particles shifts tremendously from 10-20 % organic solvent content to an organic solvent content of 40-50 %. Both co-non-solvency effects, in bulk and at the surface, can be explained by the formation of clathrate structures⁶⁰. Such clathrate structure arises due to the formation of a hydration shell around the organic solvent. This leads to a dehydration of the particles resulting in polymer-polymer interactions within the polymer network and the particle shrinking. With increasing organic solvent content, the water molecules are not able to hydrate the organic solvent anymore, whereby the clathrate structure breaks up and both solvents, water and organic solvent, interact with the particle resulting in the particle reswelling.

The shift in the size minimum from 10-20 % in bulk to 40-50 % for adsorbed particles might arise due to a shift in the distribution equilibrium between water and the organic solvent within the particles. For the bulk phase it is known that the polymer density is higher in the microgel interior and decreases towards the particle periphery. In the literature, this is often called core-shell like structure^{36,110}. DLS measurements show a stronger PNIPAM microgel swelling in pure water than in pure organic solvent, indicating a higher affinity for water. This might lead to a preferential water uptake of PNIPAM-rich phases. Therefore, it is assumed that the water/organic solvent ratio is higher in the PNIPAM rich core than within the less cross-linked shell. In addition at the surface, the particles are compressed and become a denser polymer network. According to the argument that PNIPAM-rich phases attract water stronger than organic solvent, the water to organic solvent ratio is higher in adsorbed microgels with respect to the bulk phase.

The fact that the water to organic solvent ratio is higher in the particle interior was observed before. Gawlitza *et al.* reported that the particles still exhibit a water content of 46 % in the interior after transferring the particle from water to isopropanol. Their interpretation is the formation of a water cage within the particles, which is formed during the solvent exchange¹²⁰. Wang *et al.*⁶⁶ reported a similar behaviour. They showed that the organic solvent content within the particles decreases with increasing the organic solvent content in the mixture, while the water content increases in the particle interior. It is worth to notice that in both papers the microgel was not dried between

the solvent exchange. This is different to the present paper, where the *dried* particles have been dissolved in the corresponding water-organic solvent mixtures for both, DLS and AFM experiments. In order to get information about the effect of intermediate drying after spin coating on co-non-solvency effect, the microgels have been studied by AFM under ambient conditions after spin coating from different water-organic mixtures.

The co-non-solvency effect disappears under ambient conditions. This means that no liquid and therefore no clathrate structures are formed in the gas phase. The particle volume depends tremendously on the solvent mixture from which the microgels were spin coated and increases monotonously with increasing ratio of organic solvent. This leads to the conclusion that after spin-coating organic solvent molecules are stronger entrapped than water within the microgels. During spin coating the microgels dry from the outer layer to the interior. This creates a shrunken and dense outer shell, which can be easier penetrated by the water molecules than by the organic solvent molecules (EtOH, iPr and THF). It leads to a strong enrichment of organic solvent molecules within the gels. Obviously, the size of the solvent molecules is more dominating than the vapour pressure, and the particle volume increases with increasing organic solvent/water ratio. Spin-coating from pure water instead of water-organic solvent mixtures has no qualitative impact on the co-non-solvency (size minimum at 50 % organic solvent). Consequently, the entrapment of organic solvent during the spin coating process has no influence on the shift of the size minimum.

In this case there was no enrichment of organic solvent during drying (after spin coating), but the result is qualitatively the same as after spin coating from water-organic solvent mixtures.

Particle behaviour of adsorbed particles under ambient conditions and in liquid state

In the following, the particle behaviour at the surface in liquid state and under ambient conditions is discussed in detail. During the particle collapse in liquid state, two features can be observed. First, the shrinking/swelling behaviour in vertical as well as in lateral direction differs for both PNIPAM-5 (Figure A.5 and Figure 6.4) and AAA-5 particles (Figure A.8 and Figure 6.7). Both particle types show a strong lateral shrinking at low organic solvent content (5-20 %), while the vertical shrinking is less pronounced. In contrast, particles at intermediate organic solvent content (20-50 %) show a reverse behaviour. The lateral particle shrinking plays a minor role and the particle shrinking in

vertical direction dominates, which is significantly involved in the size minimum of the particles. An important factor for the differences in the lateral and vertical shrinking behaviour of the particles arises from the PAH prelayer. Such hydrophilic layer exhibits excellent swelling properties in pure water¹²¹. The swelling of the PAH layer is affected by the water uptake resulting in flexible polyelectrolyte chains, which provide a smooth and homogeneous PAH prelayer^{122–124}. Thus, particles spin coated from pure water tend to broaden in lateral direction, which increases the particle to surface interaction between the positively charged PAH and the negatively charged microgel particles. On the other hand, such PAH layer tend to coil in water-organic solvent mixtures, due to the unfavourable interaction between the PAH layer and the organic solvent. This increases the layer roughness resulting in an inhomogeneous charge distribution within the PAH layer¹²⁵. Due to the less smooth charge distribution in the PAH prelayer, the attraction between the particles and the PAH prelayer is weakened leading to a pronounced lateral shrinking until the electrostatic interaction between the positively charged PAH prelayer and the negatively charged particle overcome the lateral shrinking. This behaviour can be observed at higher organic solvent content given that the lateral shrinking plays a minor role. The fact that strong electrostatic interactions hinder a further lateral particle shrinking can be concluded from the particle reswelling. The reswelling in lateral direction is negligible, which means that the particle is highly restricted due to the strong microgel-to-surface interaction. In contrast to the particle width, the particle height is less hindered by electrostatic attraction between the positively charged particle and the negatively charged surface. Consequently, the particle shrinking (at low organic solvent content) as well as the particle reswelling (at high organic solvent content) is unrestricted and therefore more pronounced as in lateral direction. It is concluded, that the shrinking/reswelling behaviour of the particles is mainly affected by the changes in particle height.

The chemical nature has a strong impact on the particle shrinking. Water-EtOH as well as water-iPr mixtures exhibit a stronger impact on the shrinking behaviour than water-THF mixtures (PNIPAM-5: Figure 6.3, AAA-5: Figure 6.6). The ability to form H-bonds between the corresponding solvents plays a crucial role. The H-bonds between water and THF molecules are weaker than between two water molecules¹²⁶. Thus, the clathrate formation between water and THF molecules could be less pronounced than for water-EtOH and water-iPr mixtures. Consequently, the dehydration of the polymer network by THF molecules is weaker leading to a smaller particle shrinking.

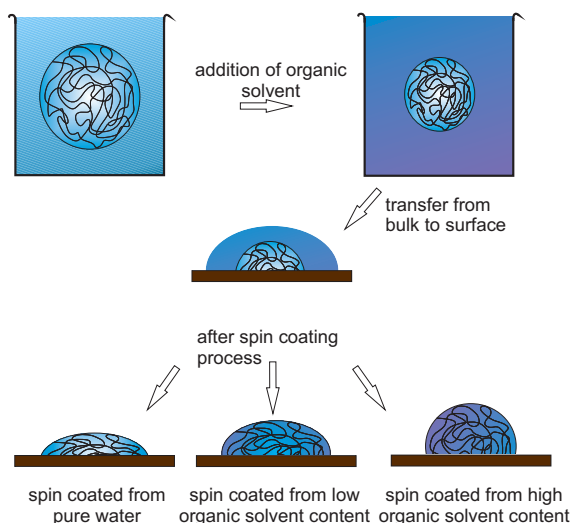


Figure 6.14: Schematic diagram of the solvent entrapment: First, the particles are dissolved in pure water. The addition of organic solvent causes a particle shrinking (co-non-solvency effect). At the surface the particles still experience the co-non-solvency effect as well as the solvent molecules can penetrate through the polymer network. During the spin coating process the surrounding water-organic solvent mixture will be removed leading to solvent entrapment. The more organic solvent in the water-organic solvent mixture is the more organic solvent is entrapped resulting in a pronounced increase of the particle volume.

The influence of different organic solvents on the co-non-solvency behaviour of microgel particles has been reported before⁶⁵.

The above mentioned organic solvent entrapment within the microgels during spin coating is basically influenced by the particle composition. Particles with a higher charge density show a strong volume increase when spin coated from pure THF, while particles with lower charge density show their largest particle volume spin coated from pure iPr. The solvent-particle interaction cannot be responsible for the volume change, since the volume for particles spin coated from pure water and pure EtOH is small compared to the particles spin coated from pure THF and pure iPr. Moreover, the size of the solvent molecules plays a crucial role for the volume increase. The significantly larger THF and iPr molecules are not able to leave the particle during the drying process.

The solvent entrapment results not only in an increase in the particle volume but also changes the particle flexibility. Burmistrova *et al.* have shown, that particles spin coated from pure water are soft leading to a flexible polymer network³⁵. Such soft and flexible particles tend to broaden at the surface. In contrast, particles spin coated from water-organic solvent mixture show a decrease in lateral dimension (PNIPAM-5: Figure A.12 and AAA-5:

Figure A.15). Consequently, the restricted and entrapped organic molecules freeze the polymer network resulting in an inflexible and stiff particle, which is not able to flatten at the surface as shown in Figure 6.14.

To investigate the swelling ability of the particles, the particle width ratio (Figure 6.13) in liquid state and in ambient conditions for the corresponding water-organic solvent mixtures have been calculated. Compared to the previous results, PNIPAM-5 and AAA-5 particles show different swelling abilities. AAA-5 particles exhibit a stronger swelling behaviour in pure water as PNIPAM-5 particles. This result was expected, due to the electrostatic contribution in the AAA-5 particles compared to the PNIPAM-5 particles. During the swelling process the co-monomer charges dominate leading to electrostatic repulsion to each other and a larger polymer network. The particle shrinking set in, due to the addition of organic solvent causes a decrease in the particle width as intensively discussed above. PNIPAM-5 particles show a strong reswelling ability, while AAA-5 particles exhibit no lateral reswelling. This behaviour arises from the particle-surface interaction. The reswelling of AAA-5 particles is strongly hindered, due to the interactions between the negatively charged particles and the positively charged surface. This electrostatic interaction leads to a particle-surface interaction and restricts a reswelling in lateral direction. The particle-surface interaction of PNIPAM-5 particles is weaker, due to the lack of charges in the particles, resulting in a stronger reswelling ability.

6.4 Conclusion

The co-non-solvency effect of particles based on PNIPAM was studied intensively at the surface and compared with results obtained from measurements in bulk phase. The impact of co-monomer as well as the cross-linker density were investigated in dependence of three different water-organic solvent (EtOH, iPr and THF, respectively) mixtures. The particles were investigated in bulk via dynamic light scattering (DLS), while for studies at the surface were performed with atomic force microscopy (AFM).

Particles in bulk show the well-known co-non-solvency effect with a particle size minimum at a solvent fraction of 10-20 %. The size minimum shifts to an organic solvent content of 40-50 % for adsorbed particles. The shift in the particle minimum to higher organic solvent fractions is attributed to the higher water/organic solvent ratio within the particle, which occurs during the particle reimmersion in solvent mixtures after the spin coating process. This

results from the strong compression of the particles at the surface compared to the particles in bulk phase. Therefore, a higher organic solvent content is needed to remove the water in the particle interior and to initialize the particle shrinking, due to co-non-solvency.

The particle shrinking at the surface can be separated in lateral and vertical shrinking, in which the shrinking in vertical direction is mainly responsible for the particle size minimum. The lateral shrinking plays a minor role and is strongly influenced by solid surface. Particles with a higher charge density form stronger microgel-to-surface attraction than the ones with lower charge density leading to a restricted particle shrinking in lateral dimension.

6.5 Outlook

The next step in this field of research would be the study of the temperature induced co-non-solvency effect. The question arises, if the particle collapse can be enhanced at high temperatures. It is also important to gather information about the change in particle stiffness during the organic solvent induced collapse. Furthermore, the SANS experiments should be performed for more water/organic solvent concentrations as well as other organic solvents such as EtOH or iPr to acquire a detailed insight into internal particle structure during the particle collapse.

Chapter 7

The Influence of different layer systems on the particle behaviour

7.1 Introduction

The increasing numbers of publications for the investigation of nanoparticles at the surface depicts the importance of research in this field^{76,127–130}. Such studies are fundamental and required for applications in e.g. biosensors^{131,132}.

Polyelectrolytes are also in the focus of current research and raise attention in several applications¹³³. Such polyelectrolyte multilayers can be built up with the layer by layer technique and can be tuned employing external parameters^{44,134,135}. Beside the number of the deposited layers, ionic strength and type of ions have a strong effect on the film thickness^{136,137}. The impact of the anions on the film thickness is much higher than for the cation. Also the mobility of the polyelectrolyte chains within the multilayer films can be controlled¹³⁸. The charge screening of the cationic polyelectrolytes within the films results in flexible polymer chains, which are more mobile within the films.

Serpe *et al.* investigated PNIPAM microgels with acrylic acid incorporated at polyelectrolyte multilayers⁷¹. The impact of pH on the surface coverage was studied. PSS coated surfaces revealed that higher surface coverage was achieved at low pH, while with increasing pH the surface coverage became poor. This was explained by the electrostatic interaction between the particles and the surface.

This chapter combines the properties of the microgel particles as well as the polyelectrolyte multilayers. It focuses on the shrinking/swelling behaviour of particles based on PNIPAM at different surface coverage. The fundamental

question arises: How does the shrinking/swelling behaviour of the particles depends on the layer composition? Furthermore, what impact has the penetration depth of the particle and the surface charge on the thermo-responsive behaviour of the particles? The materials employed for layer formation are gold, PAH, AMPS, and different double layers composed of PSS-PAH. Several heating/cooling cycles have been performed to understand the shrinking/swelling ability of the microgels.

7.2 Results

7.2.1 Layer characterisation

Table 7.1: Prepared layer systems. The first column illustrates the layer composition. The second column shows the layer thickness under ambient conditions has been determined by ellipsometry. Column 3 to 4 depict the layer roughness against water at 20 °C (column 3) and at 50 °C (column 4), respectively. The layer roughness has been determined by AFM.

Layer composition	Thickness (nm)	Roughness at 20°C (nm)	Roughness at 50°C (nm)
Gold	100	0.47 \pm 0.03	0.5 \pm 0.05
AMPS	4.2 \pm 1.2	0.34 \pm 0.13	0.31 \pm 0.07
PAH	6.9 \pm 1.4	0.69 \pm 0.11	0.41 \pm 0.13
PSS-PAH-1	4.1 \pm 2.4	0.50 \pm 0.13	0.65 \pm 0.05
PSS-PAH-3	9.9 \pm 1.9	2.00 \pm 0.26	1.94 \pm 0.38
PSS-PAH-6	21.5 \pm 1.2	4.46 \pm 1.10	5.31 \pm 0.93

The layer properties are essential for the adsorbed particles. The layer thickness and roughness are important parameters, which influence the particle behaviour.

The all layers have been prepared following the procedure described in the experimental chapter (chapter 4). Table 7.1 shows the layer thickness and layer roughness of positively charged coatings at different temperatures. The layer thickness under ambient conditions has been determined by ellipsometry, while the layer roughness has been determined by AFM. The thickness for AMPS and PAH systems are similar to one another, being in the same order of magnitude. AMPS layers exhibit a thickness of about 4 nm, while the layer thickness of PAH yield a value of 6 nm. The roughness, which was determined by the AFM, differs between these two layer systems. AMPS layers provide

a smoother surface against water with a roughness of 0.34 nm compared to PAH layers with a roughness of 0.69 nm. The film roughness for both layer systems shows no temperature dependence.

PSS-PAH layer systems show a similar behaviour. PSS-PAH-1 multilayers display a film thickness of 4.1 nm. An increase in the layer number causes an increase in the layer thickness. The thickness for PSS-PAH-3 layer was determined to 9.9 nm, while PSS-PAH-6 layer exhibit a thickness of 21.5 nm.

7.2.2 Thermo-responsive particle behaviour on surface coatings

P10 particles, which are similar to AAA-10 particles in chapter 5 but a different synthesis batch, were measured against water to study the influence of different layer systems on the particle behaviour during different heating/cooling cycles. Figure 7.1 and Figure 7.2 show the AFM images and the particle volume for P10 particles spin coated on gold, PAH and AMPS layers during heating/cooling cycles. The particles retain their thermo-responsive behaviour on the different layer systems. The particle volume for particles spin coated on AMPS decreases with increasing the heating/cooling cycles, while the particle volume spin coated on gold and PAH remains more or less constant. To gain more insight into the shrinking/swelling behaviour of the P10 particles during the several heating/cooling cycles, cross section (Figure A.16), particle height (Figure 7.3a) and particle width (Figure 7.3b) were plotted as a function of the heating/cooling cycles. Particles spin coated on AMPS exhibit the largest particle height with 400 nm, while particles spin coated on PAH and gold have smaller vertical dimension with around 340 nm. During the heating/cooling cycles, the shrinking/swelling ability of P10 particles spin coated on AMPS layers differs strongly from the shrinking/swelling ability of particles spin coated on PAH and gold layers. As shown in Figure 7.4a), the particle height ratio of particles spin coated on AMPS decreases from $\alpha = 1$ to $\alpha = 0.25$ during the heating process and increases back to $\alpha = 1$. The particle height ratio of particles spin coated on PAH and gold decreases only to $\alpha = 0.6$ and $\alpha = 0.5$ and reswells back to $\alpha = 1$ during the heating/cooling process. Interestingly, no hysteresis in the particle height can be observed for all layer systems during the heating/cooling cycles.

The particle width of P10 particles spin coated on PAH and gold shows the similar behaviour as the particle height and remain constant during the heating/cooling cycles. However, the particle width of particles spin coated on AMPS decreases from 1500 nm to 1400 nm during the first and from

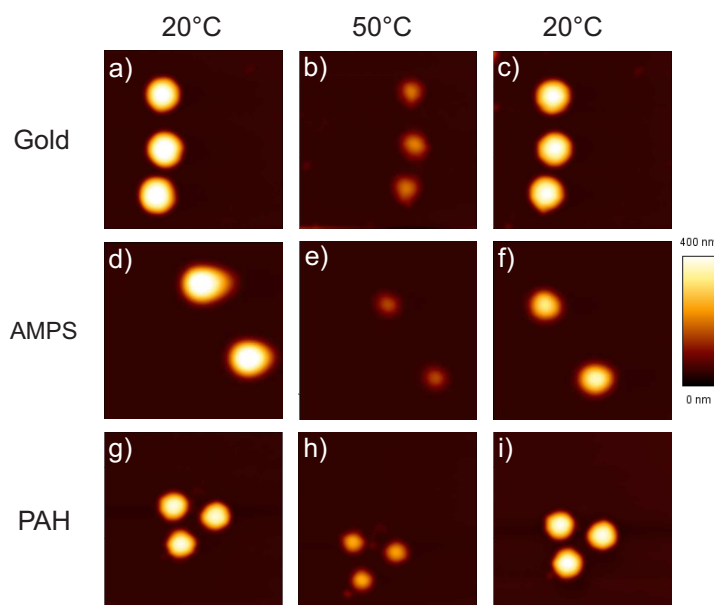


Figure 7.1: AFM images of P10 particles in liquid state spin coated on different single layer coatings during the first heating/cooling cycle. Scan size: $5 \times 5 \mu\text{m}^2$.

1400 nm to around 1300 nm during the second heating/cooling cycle. This means particles spin coated on AMPS shows a strong hysteresis behaviour in lateral dimension, while no hysteresis in lateral dimension is detected for particles spin coated on PAH and gold.

7.2.3 Effect of polyelectrolyte multilayers of different thickness

In order to study the effect of surface softness on the VPT, particles spin coated on PSS-PAH multilayer with different layer thickness were investigated. Figure 7.5 and Figure 7.6 show the AFM images and the calculated particle volume of P10 particles spin coated on different PSS-PAH multilayers against water during the heating/cooling cycles. Again, the particles retain their thermo-responsive behaviour but the volume of particles depends on the coating system. The volume of particles spin coated on PSS-PAH-1 and PSS-PAH-3 are in the same order of magnitude. However, with increasing the layer number to six, the particle volume decreases tremendously. The effect of the different multilayers becomes obviously during the heating/cooling cycles. All particles show a hysteresis behaviour during the individual heating/cooling cycles. Particles spin coated on PSS-PAH-1 and PSS-PAH-3 layers exhibit a similar hysteresis effect during the first two heating/cooling cycles. Afterwards, no further decrease in the particle volume can be observed. In

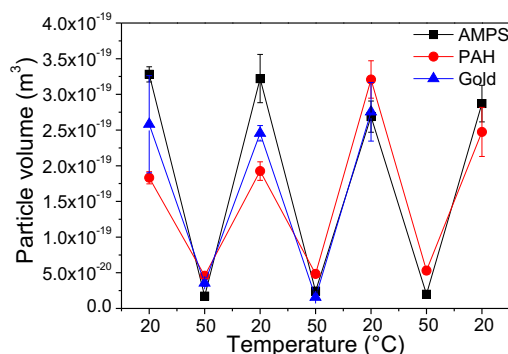


Figure 7.2: Particle volume calculated from the particle cross section of P10 particles during the two heating/cooling cycles.

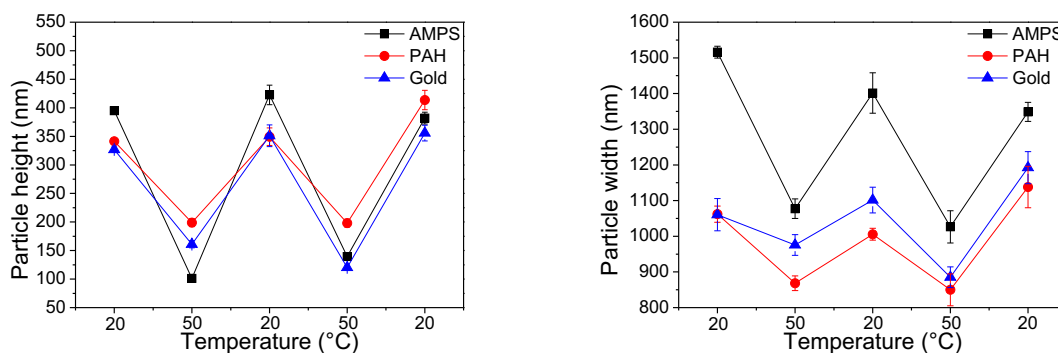


Figure 7.3: Particle height (a) and particle width (b) of P10 particles spin coated on different single layer coatings.

contrast, particles spin coated on PSS-PAH-6 show the strongest hysteresis during the heating/cooling cycles. After two cycles, the particles exhibit only half of its initial particle volume.

The particle cross section (Figure A.17), height(Figure 7.7a)) and width (Figure 7.7b)) provide information to understand the shrinking/swelling behaviour of the particles spin coated on different multilayers. The particle cross sections confirm the hysteresis behaviour in vertical and lateral dimension. The particle height for particles spin coated on PSS-PAH-1 and PSS-PAH-3 are in the same order of magnitude, while particles spin coated on PSS-PAH-6 exhibit the smallest vertical dimension. The difference in the particle height for particles spin coated on PSS-PAH-1 and PSS-PAH-3 are insignificant during the heating/cooling cycles. However, particles spin coated on PSS-PAH-6 show a large hysteresis in their shrinking/swelling behaviour. The particle height ratio (with respect to the initial particle height), shown in Figure 7.8a),

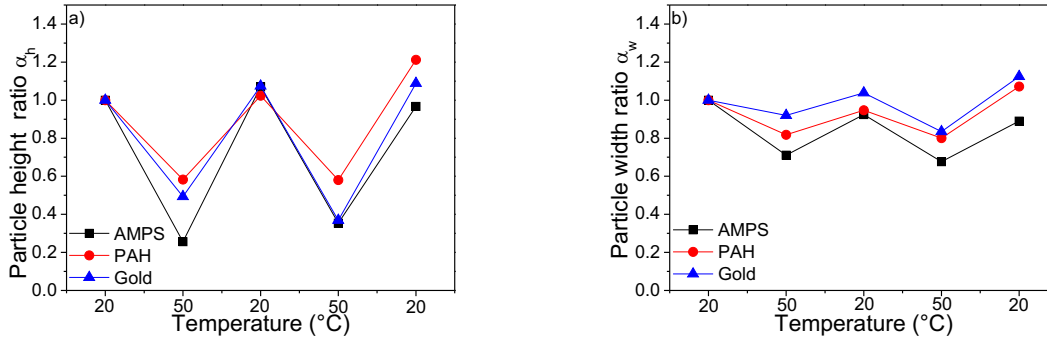


Figure 7.4: Particle height ratio (a) and particle width ratio (b) of P10 particles spin coated on different monolayer systems during the two heating/cooling cycles. The values are normalised with respect to the initial particle height and particle width, respectively.

confirms this impression. The particle height ratio for particles spin coated on PSS-PAH-1 and PSS-PAH-3 decreases from $\alpha = 1$ to $\alpha = 0.9$ for both particles spin coated on PSS-PAH-1 and PSS-PAH-3 during two heating/cooling cycles. In contrast, the particle height ratio for particles spin coated on PSS-PAH-6 decreases from $\alpha = 1$ to around $\alpha = 0.75$ during two heating/cooling cycles. The impact of the different layer thickness on the shrinking/swelling behaviour can be clearly seen in the particle width. As shown in Figure 7.7b), the initial particle width for particles spin coated on PSS-PAH-1 decreases from 1300 nm to 1200 nm in the first and from 1200 nm to 1150 nm in the second heating/cooling cycle. The particle width for particles spin coated on PSS-PAH-3 and PSS-PAH-6 decreases about 150 nm and 250 nm during the two heating/cooling cycles. Figure 7.8b) shows the particle width ratios (with respect to the initial particle width) of all particles. Indeed, the particles spin coated on PSS-PAH-1 and PSS-PAH-3 exhibit a similar particle width ratio, while particles spin coated on PSS-PAH-6 show the strongest hysteresis effect.

7.2.4 Particle behaviour at ambient conditions

Information about the particles at ambient conditions are essential to understand the complete particle behaviour at the surface. Figure 7.9 shows the AFM images for P10 at ambient conditions as a function of different layers. As shown in chapter 6, all P10 particles spin coated on the different layer systems exhibit a smaller particle size in vertical, as well as lateral direction compared to their counterparts in water.

For a better understanding of this, the particle cross sections were extrac-

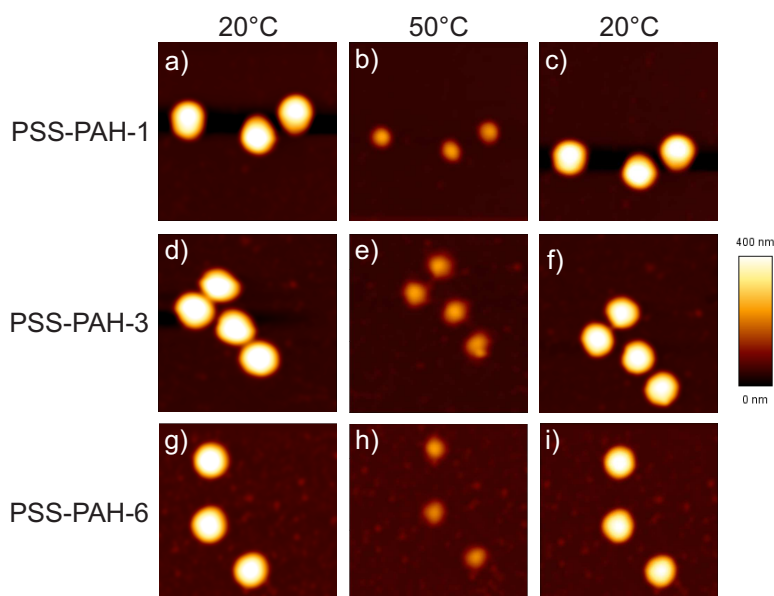


Figure 7.5: AFM images of P10 particles in liquid state spin coated on PSS-PAH multilayers of different layer numbers during the first heating/cooling cycle. Scan size: $5 \times 5 \mu\text{m}^2$.

ted to clarify the lateral and vertical particle size at the layer systems. Figure 7.10a) shows the cross section of one particle spin coated on gold, AMPS and PAH layers. An average of three different particles yield a particle height of 98 nm on AMPS, 135 nm on PAH and 130 nm on gold. The average width is 949 nm on AMPS, 849 nm on PAH and 932 nm on gold. Particles spin coated on AMPS and gold show a larger lateral dimension, while particles spin coated on PAH exhibit a smaller particle width. In contrast, the particle height for particles spin coated on gold and PAH is larger compared to particles spin coated on AMPS layer. Particles spin coated on PSS-PAH multilayers show a different behaviour as shown in Figure 7.10b). An increase in the layer number leads to a decrease in the particle height for particles spin coated on PSS-PAH-3 and PSS-PAH-6 layers. The average particle height on PSS-PAH-1 is 182 nm, for PSS-PAH-3 97 nm and for PSS-PAH-6 105 nm. Not only the particle height changes but also the particle width changes with increasing the number of layers. The average particle width is for particles spin coated on PSS-PAH-1 798 nm, for PSS-PAH-3 957 nm and for PSS-PAH-6 791 nm. Particles spin coated on PSS-PAH-1 and PSS-PAH-6 layers exhibit the same particle width. Particles spin coated on PSS-PAH-3 layers, in contrast, experience an increase in particle width.

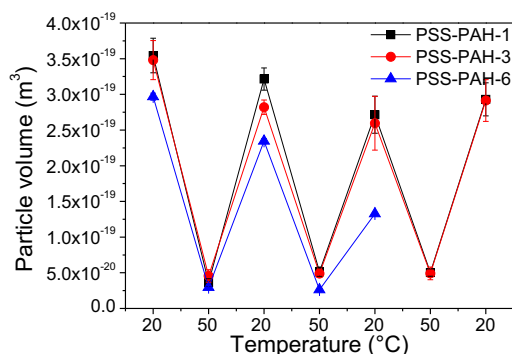


Figure 7.6: Particle volume calculated from particle cross sections of P10 particles during two heating/cooling cycles.

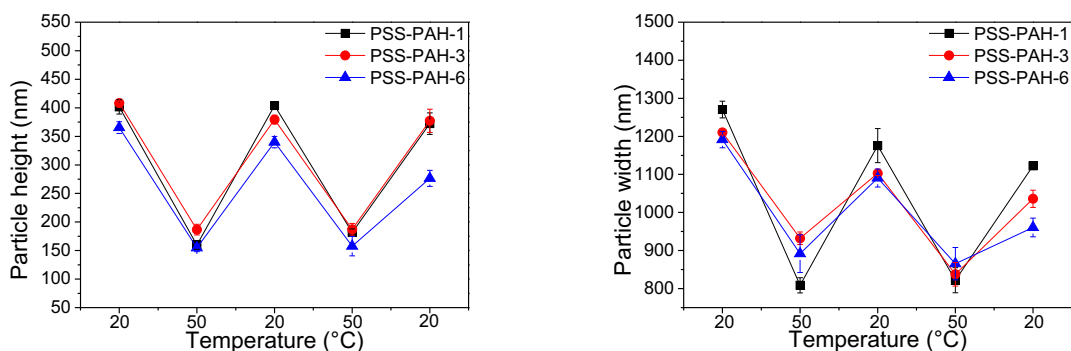


Figure 7.7: Particle height (a) and particle width (b) of P10 particles spin coated on multilayer with different film thickness.

7.3 Discussion

7.3.1 Properties of different single layer coatings

The results for the single layer coatings are consistent to one another. On the one hand both layer systems, PAH and AMPS, exhibit a film thickness, which is in the same order of magnitude. On the other hand, the surface roughness of PAH layers is larger than that of AMPS layers. This fact has its origin potentially in the poor surface coverage of PAH compared to AMPS layer. In case of multilayer systems, here namely the PSS-PAH system, an increase in the film thickness takes place with increasing layer number. This is in good agreement with the literature and is explained by the overcompensation of the charges and the entropy driven adsorption^{121,139,140}. The charges of the adsorbing polyelectrolyte overcompensate the charges of the end-terminated polyelectrolyte layer leading to a charge reversal. Secondly, the entropically

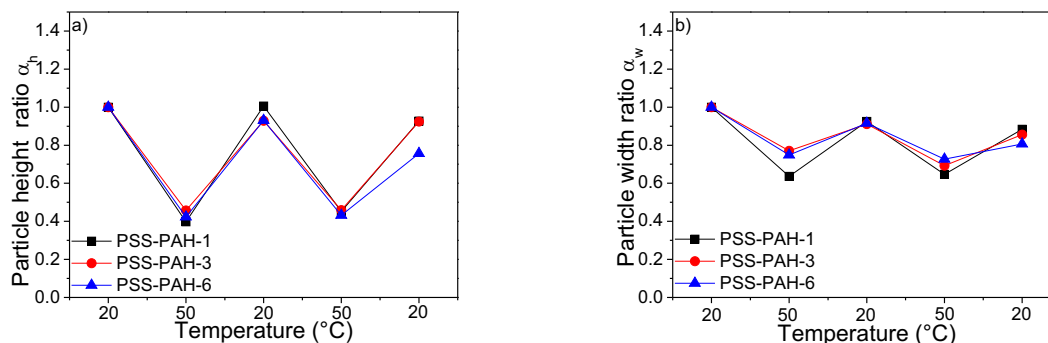


Figure 7.8: Particle height ratio (a) and particle width ratio (b) of P10 particles as a function of different PSS-PAH multilayers during the two heating/cooling cycles. The values are normalised with respect to the initial particle height and particle width, respectively.

favoured ion release between end-terminated polyelectrolyte layer and the free polyelectrolyte leads to adsorption and thus an increase in film thickness. The polyelectrolyte adsorption not only leads to an increase in the film thickness but also to an increase in the film roughness. This can be explained by the internal roughness between the single PAH layer and the PSS layer¹⁴¹. The higher the number of deposited layers the rougher the multilayer surface. All polyelectrolyte layers, monolayers and multilayers, smoothen in their liquid state. Here, the interaction between the polyelectrolytes and water molecules are favoured leading to a flexible and smooth film^{121,123}.

7.3.2 Particle behaviour at different single layer coatings

PNIPAM-co-AAA particles were spin coated on different single layer coatings. The layer coatings were two positively charged coatings (PAH and AMPS layers) and gold. All particles remain their thermo-responsive behaviour during several heating/cooling cycles. However, particles spin coated on AMPS show a hysteresis, while particles spin coated on PAH and gold layers exhibit no hysteresis. This is an interesting, since both layers, PAH and AMPS, are positively charged, which should lead to electrostatic attraction between the negatively charged particles. However, particles spin coated on AMPS exhibit a smaller particle height as well as a larger particle width under ambient condition and a larger lateral dimension against water compared to particles spin coated on PAH. These facts assume a stronger electrostatic attraction between the particles and AMPS layers compared to the particle/PAH system. A similar observation was shown before for other particle/polyelectrolyte

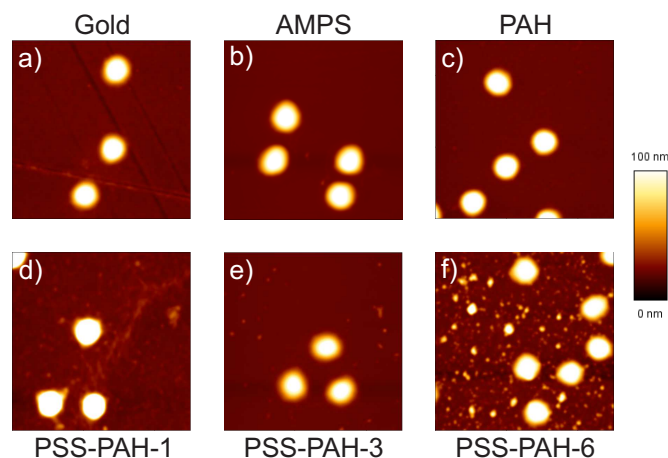


Figure 7.9: AFM images of P10 particles as function of different layer systems under ambient conditions. Scan size: $5 \times 5 \mu\text{m}^2$.

systems⁷¹. Thereby, the surface coverage of the AMPS and PAH layers plays an important role. As mentioned above, the higher roughness of PAH layers suggests a poor surface coverage. Hence, the electrostatic attraction between the negatively charged particle and the positively charged PAH layers is less pronounced as compared to the more homogeneous AMPS layers and particle. These stronger electrostatic attraction affects the hysteresis in lateral dimension for particles spin coated on AMPS compared to particles spin coated on PAH. Particles spin coated on AMPS not only show a hysteresis but also exhibit a larger shrinking/swelling ability in lateral dimension compared to particles on PAH. The particle width decreases about 400 nm during the heat-

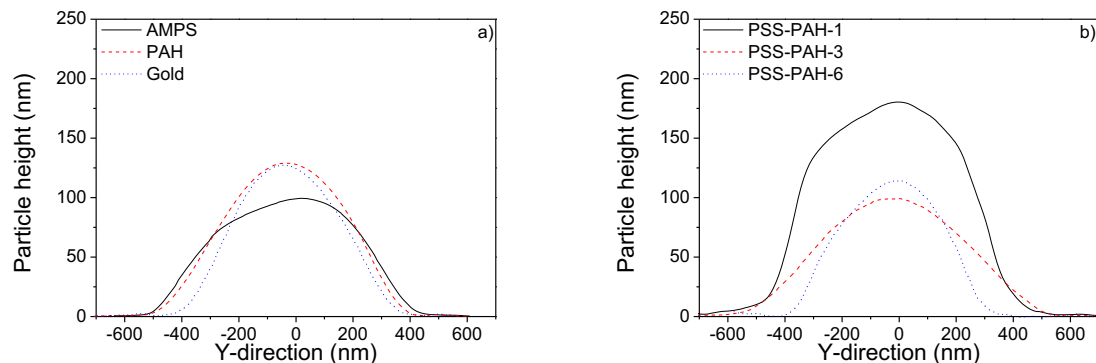


Figure 7.10: Particle cross sections of P10 particles at ambient conditions spin coated on (a) different monolayer systems and (b) different PSS-PAH multilayers.

ing process, while the width of the particles spin coated on PAH decreases 200 nm during the heating process. This indicates a better sliding ability for particles on AMPS compared to particles on PAH due to the hydrophobic effect of AMPS layer. The hydrophobic effect of the AMPS has its origin in the longer alkyl tail of the surfactant. Therefore, the AMPS surface and the particle do not integrate strongly due to the hydrophobic differences (AMPS: hydrophobic, particle: hydrophilic) resulting a better sliding and consequently a better shrinking ability. In contrast, PAH layer exhibit dangling ends, which interfere with the particles leading to restricted shrinking process.

7.3.3 Particle behaviour on multilayers with different film thickness

PNIPAM-co-AAA (P10 particles) have been spin coated on different PSS-PAH-X (X=1,3,6) multilayers and have been studied during several heating/cooling cycles. As observed for single layer coatings, the particles remain their thermo-responsive behaviour during several heating/cooling cycles. The initial volume of particles spin coated on PSS-PAH-1 and PSS-PAH-3 is more or less in the same order of magnitude, while particles spin coated on PSS-PAH-6 experience a reduction in the volume compared to particles spin coated on PSS-PAH-1 and PSS-PAH-3. The same trend can be also observed for the particle height. Particles on PSS-PAH-1 and PSS-PAH-3 exhibit similar particle height, while a decrease in the height takes place for particles on PSS-PAH-6. However, the main reason for the differences in the particle volume has its origin in the particle width decreasing in the order of PSS-PAH-1 > PSS-PAH-3 > PSS-PAH-6. These observations are a combined interplay between electrostatic attraction, hydrophobic effects and the multilayer thickness. The electrostatic attraction between the negatively particles and positively charged multilayers should be the same for PSS-PAH-1, PSS-PAH-3 and PSS-PAH-6, since PAH is the outer layers for all prepared multilayers. It is known from literature that the surface potential remains constant irrespective of the number of deposited double layers¹⁴². Hence, the electrostatic attraction plays a minor role in the decrease of the initial particle volume. However, an increase in the layer thickness has a tremendous impact on the particle volume. The thickness of the multilayers increases in the order of PSS-PAH-1 > PSS-PAH-3 > PSS-PAH-6 leading to a strong particle penetrate into the multilayer and a smaller particle volume. Measurements under ambient conditions support this. The particle penetration into PSS-PAH-1

layers is rather weak compared to particles spin coated PSS-PAH-6 leading to a large particle height.

With starting the heating/cooling cycles the effects of particle penetration into the multilayer thickness becomes more pronounced leading to a continuous decrease in the volume of all particles. Particles on PSS-PAH-1 and PSS-PAH-3 show less reduced particle volume during the heating/cooling cycles, while the strongest decrease in the particle volume is observed for particles on PSS-PAH-6. Interestingly, the height of particles on PSS-PAH-1 and PSS-PAH-3 decreases marginal. In contrast, particle on PSS-PAH-6 show a strong decrease in the particle height. However, the largest contribution of the volume decrease is attributed to the particle width, which decreases for all particle during the heating/cooling cycles. Furthermore, the particle reswelling ability decreases from the first to the second heating/cooling cycle. The change of the volume for particles on PSS-PAH-1 and PSS-PAH-3 is mainly affected by the decrease in the particle width, while the decrease in particle height less pronounced. Lateral shrinking/swelling behaviour is mainly affected by electrostatic interaction, while the shrinking/swelling behaviour in vertical dimension is influenced by the particle penetration into the multilayers. Since the particle width decreases stronger compared the particle height, it can be concluded that electrostatic interactions dominate over particle penetration. Not only electrostatic interaction affects the shrinking/swelling behaviour of particles on PSS-PAH-6 but also the penetration depth of the particles. Particles spin coated on PSS-PAH-6 penetrate deeper into the multilayers. Hence, a strong interpenetration between particle and multilayers takes place. This interpenetration leads to a restricted shrinking/swelling ability during the individual heating/cooling cycles and a hysteresis behaviour in lateral as well as vertical dimension. Additionally, the roughness within such multilayers increases with increasing the layer number¹²¹. This effect could enhance the particle hysteresis, since the particles are not able to slide freely.

7.4 Conclusion

The shrinking/swelling behaviour of particles spin coated on different single layer coatings (AMPS, PAH and gold) and multilayers (PSS-PAH-X, X=1, 3 and 6) have been studied intensively during several heating/cooling cycles. Particles spin coated on thinner layers show mainly a decrease in their lateral dimension, while with increasing the layer thickness the particle shrinks in both, lateral and vertical, dimension.

The shrinking/swelling behaviour of particles spin coated on thinner layers is mainly affected by electrostatic attraction since the penetration of these particles is less pronounced. Thus, no additional interaction takes place between the particles and layer coatings. With increasing the layer thickness, the particles penetrate deeper into the layer coatings. Hence, the shrinking/swelling ability is restricted due to the interpenetration of the multilayers into the particles and the internal roughness of the multilayer.

7.5 Outlook

Further experiments would focus on multilayers with more PSS-PAH multilayers to afford a better understanding of the correlation between film thickness and particle behaviour. The investigation of different single layers on the particle behaviour needs to be studied. Here, the focus should lay on more biocompatible polyelectrolytes. The salt and pH dependence on such particle/multilayer systems are other parameters, which are interesting and useful for application. On the one hand, particles at high ionic strength show a decrease in size. On the other hand, the size of the multilayers increases with increasing the ionic strength. This is an interesting effect, which has to be studied.

Chapter 8

Interaction between microgel particles and azobenzene containing surfactant

This chapter was a cooperation with Dr. Yuriy Zakrevskyy from AK Svetlana Santer from the University Potsdam and contains parts of the paper: "Light-Controlled Reversible Manipulation of Microgel Particle Size Using Azobenzene-Containing Surfactant, *Adv. Funct. Mater.*, (2012), 22, 5000-5009" as well as "Effect of pH and co-monomer content on the swelling behaviour of microgel-azobenzene containing surfactant complex", accepted for publication in *Polymer*.

8.1 Introduction

The challenge in the sensor applications demand fast and precise response towards external parameters¹⁴³⁻¹⁴⁵. Such application requires a matrix, which is sensitive to external parameters. Microgels based on PNIPAM fulfill such specifications, due to their thermo-responsive behaviour^{146,147}. The incorporation of pH responsive co-monomers in microgels results not only in thermo-responsive but also in pH responsive microgel^{99,148}. The change in the salt concentration also causes a change in the particle size, due to the charge screening in the polymer network²⁵.

A more convenient method to induce the particle collapse arises from the incorporation of small molecules^{120,149}. The change in the particle size can be easily achieved by irradiation to generate heat in the particle¹⁵⁰. The heat generated allows a partial PNIPAM collapse. Such remote controlled systems play an increasing role in applications¹⁵¹.

A more gentle way to realize the particle collapse is the incorporation of

azobenzene containing surfactants in the polymer matrix^{106,109}. Such azobenzene can switch between their *trans*- and *cis*-state depending on the irradiation wavelength. The driving force for the surfactant uptake arises from electrostatic as well as hydrophobic interactions between the particle and the surfactant. The hydrophobic *trans*-conformation binds to the microgel, while the hydrophilic *cis*-conformation shows a lower affinity to interact with the microgel.

This chapter discusses the interaction between PNIPAM particles, which contain the co-monomer AAA, and an azobenzene containing surfactant. The microgel concentration was fixed during the experiments, while the surfactant concentration was steadily increased. Another aim is the particle size manipulation via UV-VIS irradiation. Furthermore, the behaviour of the microgel/surfactant complex in different buffer solutions at a fixed pH is investigated. The experiments in bulk are done using DLS and zeta potential measurements.

8.2 Microgel/surfactant complex in pure water

8.2.1 Formation of the microgel/surfactant complex

The formation of the microgel/surfactant complexes can be performed by mixing a negatively charged microgel and positively charged surfactant, which is shown in Figure 8.1, in pure water. The effective microgel charge was determined via titration with a 2.5 mM NaOH. The titration yields a effective AAA incorporation of 9 %. For the microgel/surfactant complex preparation, the surfactant in *trans*-conformation was used. All presented measurements were performed at 20 °C.

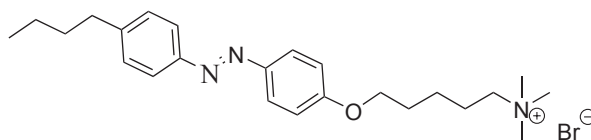


Figure 8.1: Chemical structure of the used surfactant synthesised by Nino Lomadze from University Potsdam.

The understanding of the microgel/surfactant complex formation necessitates the construction of a phase diagram of the microgel and the surfactant as shown in Figure 8.2. The microgel concentration is plotted on the ordinate, while the charge ratio Z (the molar ratio of surfactant divided by the

molar ratio of the co-monomer units AAA within the microgels) is plotted on the abscissa. Both, the ordinate and the abscissa, are plotted in log scale to observe a change in the order of two or more magnitudes. Surfactants, like the azobenzene containing surfactant, are able to form micelles at a certain concentration. This concentration is the so-called critical micelle concentration (CMC) as is shown by the blue line in Figure 8.2. To avoid influences arising from the formation of micelles, all experiments were performed below the CMC.

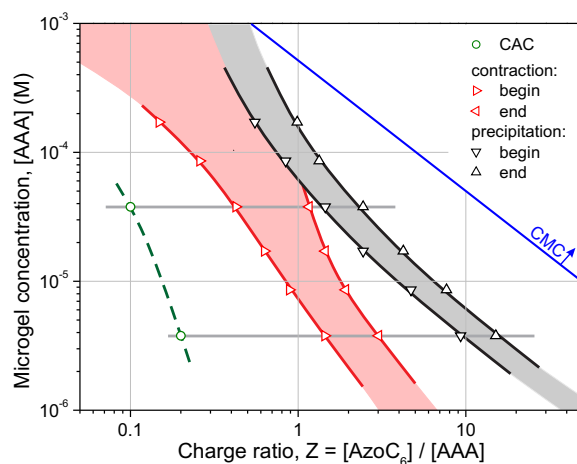


Figure 8.2: Phase diagram of AAA-50 particles and the azobenzene surfactant constructed via turbidity measurements²⁹. The measurements were performed at 20 °C.

In the following, the interaction between the microgel and the surfactant will be discussed. The microgel concentration is fixed exemplary to $3.8 \cdot 10^{-5}$ M and $3.8 \cdot 10^{-6}$ M (horizontal grey lines in Figure 8.2), while a steady increase in the surfactant concentration, which also means an increase in the charge ratio Z , takes place. The microgel undergoes several transition steps during the increase of the surfactant concentration. At low charge ratios the positively charged surfactant starts to bind to the negatively charged microgel. Further increase in the surfactant concentration initiates the particle contraction. The red area in Figure 8.2 indicates the contraction range of the microgel/surfactant complex. Again further increase in the surfactant concentration leads to a complete charge compensation in the microgel resulting in the precipitation of the microgel/surfactant complex. The grey area in Figure 8.2 shows the precipitation range of the microgel/surfactant complex. At higher Z ratio the microgel/surfactant complex regains its colloidal stability due to charge reversal of the microgel/surfactant complex.

To study the interaction between microgel and the surfactant during the

formation of the microgel/surfactant complex, dynamic light scattering and zeta potential measurements at two fixed microgel concentrations were performed. The microgel concentrations are $3.8 \cdot 10^{-5}$ M and $3.8 \cdot 10^{-6}$ M, which are marked with the horizontal grey lines in Figure 8.2. The surfactant was in *trans*-conformation during the complex formation and therefore also during the measurements.

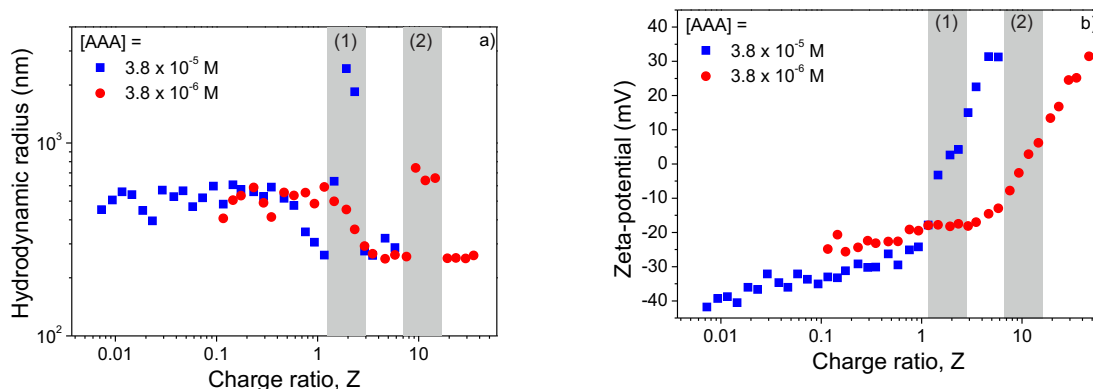


Figure 8.3: The hydrodynamic radius (a) and zeta potential (b) of AAA-50 particles as a function of charge ratio Z at two different AAA concentrations. The surfactant was in *trans*-conformation during measurements. The grey lines represent the precipitation range of the microgels at different concentrations (1: $3.8 \cdot 10^{-5}$ M, 2: $3.8 \cdot 10^{-6}$ M). The measurements were performed at 20 °C.

Figure 8.3a) shows the hydrodynamic radius of AAA-50 particles as a function of the charge ratio Z at the two different AAA concentrations. At low Z ratio, the particle radius does not change significantly. The large scattering of the obtained radii in this region is related to the flexible polymer network in the swollen state. The particles start to contract at a certain Z ratio. Further increase in the surfactant concentration leads to low net charge of the particles. The precipitation range starts at $Z=1.8$ and ends at $Z=2.5$ for a microgel concentration of $3.8 \cdot 10^{-5}$ M, while for a particle concentration of $3.8 \cdot 10^{-6}$ M it starts at $Z=10$ and ends at $Z=18$. The microgel/surfactant complex restores its colloidal stability at higher charge ratio Z . Remarkably the hydrodynamic radii show no large scattering at higher Z values, which means that the surfactant also stabilises the particle morphology.

To get a better understanding of this particle collapse, zeta potential measurements were performed as shown in Figure 8.3b). Here, the zeta potential of AAA-50 particles is plotted as a function of the charge ratio Z at the same concentration as it was done for the hydrodynamic radius measurements. The

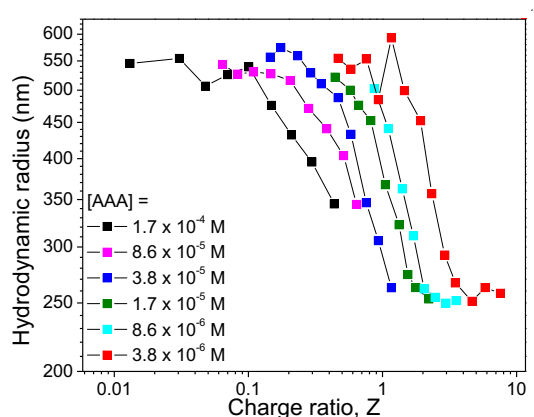


Figure 8.4: The hydrodynamic radius of AAA-50 particles as a function of charge ratio Z at different AAA concentrations. The measurements were performed at 20 °C. Data points of precipitation range were removed.

AAA-50 particles exhibit a zeta potential of -40mV at low Z ratios, due to the negatively charged co-monomer AAA. A steady increase in the positively charged surfactant concentration causes an increase in the zeta potential. A zeta potential of 0 mV is reached at $Z=1.8$ for a microgel concentration of $3.8 \cdot 10^{-5}$ M, while the neutral zeta potential for a microgel concentration of $3.8 \cdot 10^{-6}$ M is located at $Z=10$. These results perfectly match with to the precipitation range obtained from the light scattering experiments. Further increase in the surfactant content leads to both colloidal stability of the particles and a positive zeta potential.

The results obtained from light scattering measurements as well as from zeta potential measurements confirm that the formation of the microgel/ surfactant complex occurs in several steps. The first step can be described as the surfactant binding to the microgel. The surface charge of the microgel will be gradually compensated by the positively charged surfactant, which creates an increase in the zeta potential but has no effect on the particle size. Further increase in the charge ratio leads to a progressive charge compensation within the microgel, which results in the particle contraction. The microgel/surfactant complex precipitates, if the positively charged surfactant compensates the complete negative microgel charge leading to a neutral zeta potential. At higher Z ratio, the particles regain their colloidal stability via the surfactant uptake within the particle as well as the binding of the positively charged surfactant on the particle surface, which leads to a positive zeta potential at high Z ratios.

Figure 8.4 shows the hydrodynamic radius for different microgel concen-

trations as a function of the charge ratio Z . The hydrodynamic radius of the particles decreases by more than half of its initial size during the formation of the microgel/surfactant complex. The contraction range shifts to higher charge ratios with decreasing the microgel concentration due to the different concentration ratio between microgel and surfactant. At low microgel concentration, the surfactant concentration is lowered within the microgels. Hence, more surfactant (higher charge ratio) is needed to initialise the particle contraction. Whereas at higher microgel concentration, low charge ratio affects a high surfactant concentration within the microgel leading to microgel contraction.

8.2.2 Light induced particle collapse

As mentioned previously, the azobenzene containing surfactant can be switched between its hydrophobic *trans*-conformation, which is thermodynamically more stable, and its hydrophilic *cis*-conformation, which is thermodynamically unfavoured, simply by UV-VIS irradiation. The switching from *trans*- to *cis*-conformation can be realised by UV light, while the switching from the *cis*- to the *trans*-state can be done by blue light. Figure 8.5 shows the hydrodynamic radius of the particle as a function of the irradiation step. The AAA-50 particles exhibit a particle size of about 600 nm. The irradiation with blue light causes a decrease in the particle size of about 350 nm. Again, the collapsed particles have been irradiated with UV light resulting in a particle reswelling leading to a particle size of about 600 nm. This procedure can be repeated several times to cause a particle collapse with blue light and a particle reswelling with UV light.

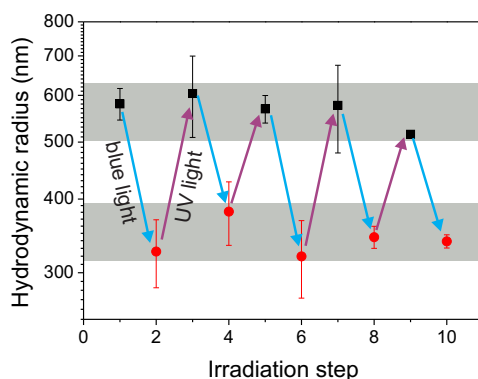


Figure 8.5: The hydrodynamic radius after the irradiation with blue and UV light. The measurements were performed at 20 °C.

The particle collapse and the particle reswelling is related to the binding ability of the surfactant in its different conformation states. The *trans*-conformation of the surfactant is generated by blue light irradiation. The surfactant in its *trans*-conformation binds to the microgel leading to a particle collapse. The formation of the microgel/surfactant complex is driven by the electrostatic interaction between the negatively charged particles and the positively charged surfactant. Additionally, the hydrophobic interaction between the surfactant and the particles favours the binding of the *trans*-conformation to the particles.

The irradiation with UV light leads to a switching in the surfactant conformation from *trans*- to *cis*-state and the unbinding from the particles. Thus, the repulsive interaction in the particles increases, leading to a particle reswelling. Consequently, the *cis*-conformation shows a lower binding ability to the particles.

The swelling and deswelling process of the particle initialised by the UV-VIS irradiation is clearly driven by the charge compensation of the microgel/surfactant complex. Additionally, hydrophobic interaction between the surfactant in the hydrophobic *trans*-state and the particles enhances the surfactant binding.

8.2.3 Influence of co-monomer concentration on the particle contraction

Two microgels with different co-monomer concentrations were investigated to study the effect of the co-monomer content on the particle contraction process. AAA-25 particles and the before well studied AAA-50 particles were chosen for this purpose. The incorporation of AAA was determined via titration with 2.5 mM. The titration of AAA-25 and AAA-50 particle yields an incorporation of 3.8 % AAA and 9 % AAA, respectively. The co-monomer concentration was fixed to $1 \cdot 10^5$ M for both particle types. It should be noted that the particle number for AAA-25 particles is 2.4 times higher than for AAA-50 particles but the effective co-monomer concentration is the same for both AAA-25 and AAA-50 particles.

Figure 8.6 shows the change in the particle size as a function of the charge ratio Z for both AAA-25 and AAA-50 particles. AAA-25 as well as AAA-50 particles exhibit nearly the same particle size of about 580 nm at a low charge ratio Z . The increase in the surfactant concentration causes a particle contraction for both particle types. The AAA-25 particles start to shrink at $Z=1$ until

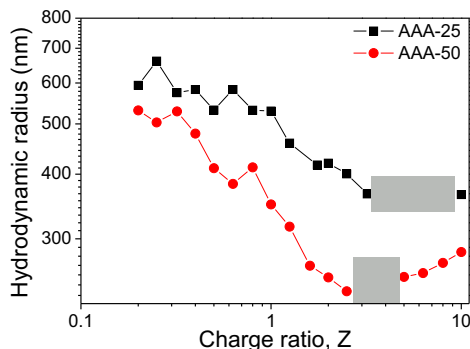


Figure 8.6: Particle radius of AAA-25 (black squares) and AAA-50 particles (red dots) as a function of surfactant concentration. The particle radius without surfactant is 730 nm for AAA-25 and 791 nm for AAA-50. Concentration of the microgels: 10^{-5} . The grey bars indicate the corresponding precipitation range. The measurements were performed at 20 °C.

Z=2. The contraction range for AAA-50 particles starts at $Z=0.6$ and ends at $Z=2$. Consequently, both AAA-25 particles and AAA-50 particles contract in nearly the same Z ratio interval. Further increase in the charge ratio results in a precipitation of the microgel/surfactant complex. AAA-25 particles precipitate between a charge ratio of $Z=4$ and $Z=6$, while the precipitation range for AAA-50 particles shifts to slightly lower Z values. AAA-50 complexes start to precipitate at $Z=2$ and end at $Z=3$. As mentioned above, the particles regain their colloidal stability at higher charge ratios. Thereby, it can be observed that both particles differ in size. With a similar particle size for AAA-25 and AAA-50 particles at low Z ratio, the microgel/surfactant complex of AAA-50 particles shrink to a size of 250 nm, while the microgel/surfactant complex of AAA-25 particles exhibits a size 400 nm after regaining their colloidal stability at high Z ratios.

The obtained results indicate a highly similar behaviour for both particle types. The particle contraction, which is nearly in the same Z ratio range for both particle types, is mainly driven by the charge compensation of the particles and is independent of the particle composition. In contrast, the precipitation range of AAA-25 shifts slightly to larger Z values compared to AAA-50, that might be connected to the different sizes of contracted particles and/or the corresponding differences in the surface charge densities of both microgels.

The shrinking process of AAA-50 particles is stronger compared to the one of AAA-25 particles. AAA-50 particles shrink from 580 nm to about 250 nm,

while AAA-25 particles collapse from 600 nm to about 400 nm. For the understanding of this shrinking behaviour, the particle morphology has to be taken into consideration. As shown in chapter 5, the incorporation of AAA into the particles increases the particle hydrophobicity due to the longer alkyl chain. The increased hydrophobicity and additionally the higher charge density within AAA-50 particles favours an increased surfactant binding via hydrophobic and electrostatic interactions leading to a higher surfactant concentration within AAA-50 compared to AAA-25 particles. Hence, the AAA-50 particle becomes even more hydrophobic due to the higher surfactant concentration within the particle leading to a less hydrated and therefore stronger contracted particle.

8.3 Microgel/surfactant complex in different buffer solutions

8.3.1 Phase diagram of AAA-50 particles in buffer solutions

As shown above, the formation of microgel/surfactant complexes and the resulting possibility to cause particle swelling/contraction by UV-VIS irradiation offer new application field.

From the obtained results arise the question of the microgel/surfactant complex behaviour in buffer solutions to use such systems in biological applications. The complex formation was studied in three different buffers (phosphate, Tris and phthalate) with a concentration of 1 mM. The AAA-50 concentration was $1 \cdot 10^{-5}$ M, which is two orders of magnitude lower than the buffer concentration. The difference in both concentrations was used to ensure a stable pH during the addition of the surfactant.

Figure 8.7 shows the phase diagram of AAA-50 particles dissolved in different buffer solutions at different pH values as function of the charge ratio Z . The charge ratio Z is plotted in log scale. The grey area represents the precipitation area of the microgel/surfactant complex in phosphate buffer from pH=6 to pH=8, while the precipitation range for Tris and phthalate buffers are illustrated by the two grey bars at a fixed pH of 7.

As discussed above, the formation of the microgel/surfactant complex occurs in several steps. At first, the surfactant binds to the microgel, which leads to a particle contraction. Further increase in the charge ratio results in a complete charge compensation of the negatively charged microgel. The microgel/surfactant complex regains its colloidal stability in the third step.

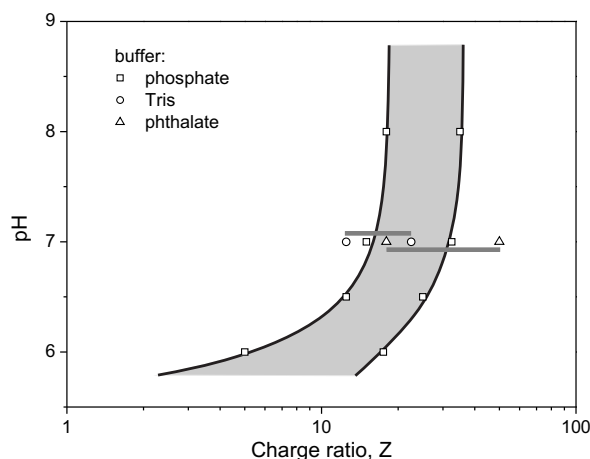


Figure 8.7: Phase diagram of the AAA-50/surfactant complex in different buffer solutions¹⁵². The buffer concentration was 10^{-3} M. The measurements were performed at 20 °C.

From the obtained results it can be seen that the precipitation range can be adjusted by the pH of the solution. At pH=6, the co-monomer units are not fully deprotonated and necessitate less surfactant for a complete charge compensation. Therefore, the microgel/surfactant complex precipitates at $Z=5$ and regains its colloidal stability at $Z=12$. With increasing pH the AAA deprotonation elevates resulting in a higher charge density in the particle. Consequently, the precipitation range shifts to higher Z ratios for higher pH values. At a certain pH, all AAA groups are deprotonated leading to a constant precipitation range. Changing the buffer system at pH=7 causes a slight shift in the precipitation range to lower Z values for Tris buffer and to higher Z values for phthalate buffer. The differences in the precipitation range are related to the chemical nature of the buffer system. Tris contains an amino group, which can interact with the AAA leading to a shift to lower Z ratios. In contrast, the phthalate buffer dissociates to phthalate anions, which can interact with the positively charged surfactant resulting in a shift to higher Z ratios.

8.3.2 Contraction process of AAA-50 particles in buffer solution

To understand the role of the buffer in the particle contraction, the microgel/surfactant complex were studied at different pH values in phosphate buffer.

Figure 8.8 shows the particle radius of AAA-50 in phosphate buffer at different pH values as a function of the charge ratio Z . At low charge ratios,

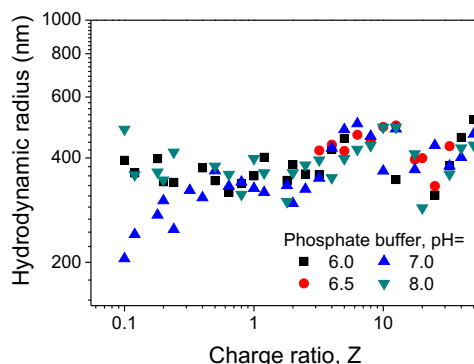


Figure 8.8: The hydrodynamic radius of AAA-50 particles in phosphate buffer at different pH as a function of charge ratio Z . The ionic strength of phosphate buffer was 10^{-3} M. The measurements were performed at 20 °C.

the particles size is about 400 nm. The discrepancy in the particle size at low charge ratios results from the flexible polymer network and leads to a large variation in the particle size. With increasing in the charge ratio Z no particle contraction can be observed as for the microgel/surfactant complex formation in pure water.

Reference measurements were performed to investigate the disappearance of the particle contraction during the microgel/surfactant formation in the buffer solution. Figure 8.9 shows the particle radius as well as the zeta potential of AAA-50 particles without surfactant in different buffer systems as a function of pH. Neither the particle radius nor the zeta potential of the particle change significantly. As shown above, the particle size of AAA-50 particles was found to be about 550 nm and decreases to 330 nm in buffer solution. Furthermore, the zeta potential in pure water was determined to a value of -40 mV and increases to -25 mV in buffer solution.

The result obtained from the reference measurements clarifies the missing particle contraction during the formation of the microgel/surfactant complex in buffer solution. The mixing of the microgel in buffer solution leads to charge screening of the negatively charged AAA-50 particles by the positively charged counterions resulting in a decrease in the particles size from 550 nm in pure water to 330 nm in buffer solution¹⁵³. These counterions screen the binding sites of the negatively charged particles for the positively charged surfactant. Therefore, the surfactant cannot attain in the polymer network nor trigger the particle contraction. A similar effect was observed for PNIPAM-co-AAc microgels/lysozyme complexes¹⁵⁴. Thus, only the particle surface provides the possibility for the surfactant binding. Precipitation of

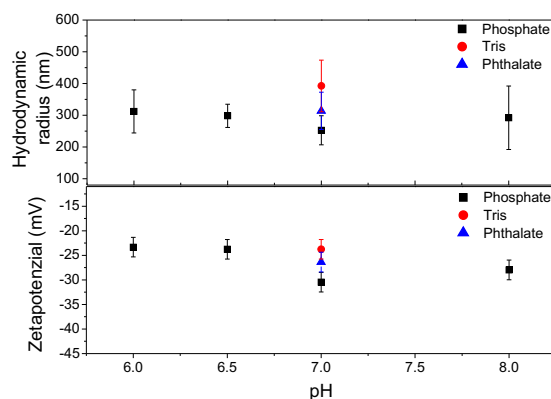


Figure 8.9: The hydrodynamic radius (top) and zeta potential (bottom) of AAA-50 particles in different buffer systems as a function of pH. The ionic strength of all buffer solutions was 10^{-3} M. The measurements were performed at 20 °C.

the microgel/surfactant complex takes places, if the negatively charged surface is completely compensated by the positively charged surfactant as shown in Figure 8.7.

8.4 Conclusion

The binding process between a azobenzene containing surfactant, which is positively charged, and a negatively charged microgel is studied intensively. The surfactant can be switched between the *trans*- and *cis*-conformation, due to UV-VIS irradiation. PNIPAM-based particles containing different AAA co-monomer contents are used as microgels.

The formation of the microgel/surfactant complex has been performed in pure water and different buffer systems. The complex formation in pure water can be separated in four states. The first state is the surfactant binding to the microgel, particle contraction takes place in the second state, due to the charge compensation. The third state is the complete charge compensation of the microgel and the resulting precipitation of the microgel/surfactant complex. In the fourth state, the formed microgel/surfactant complex regains its colloidal stability. The contraction range as well as the precipitation range depends on the microgel concentration. Furthermore, the particle contraction shows significant differences between microgels with low and high co-monomer content. Particles with higher co-monomer content show a higher degree of contraction than particles containing less co-monomer.

The particle contraction during the complex formation disappears in buffer

solution. The buffer counterions screen the co-monomer charges and hinder the interaction between the microgel and the surfactant. Only the precipitation of the microgel/surfactant complex takes place meaning that the surfactant binding occurs at the microgel surface.

The *cis-trans* isomerism of the azobenzene containing surfactant has been utilised to manipulate the particle size by UV-VIS irradiation. Blue light generates the *trans* state, which is able to bind to the microgel leading to a particle collapse. The *cis* state can be realised by UV irradiation. The *cis* conformation unbinds from the microgel leading to a particle reswelling.

8.5 Outlook

The behaviour of such microgel/surfactant complexes is intensively studied in bulk. The next experiments should deal with the behaviour of such complexes at the interfaces, which offers great potential in sensor applications. The experiments should focus on the change in the particle size as a function of the surfactant concentration. The thermo-responsive behaviour of these complexes should also be studied. One should also address the question of the particle stiffness and the size manipulation via UV-VIS irradiation.

Chapter 9

In situ particle degradation of PG-based microgels by AFM

This chapter contains parts of the paper: Visualization of real time degradation of polyglycerol via Atomic force microscopy, accepted for publication in *Macromolecular Rapid Communication*.

9.1 Introduction

Not only PNIPAM based microgels raise interest in research but also microgels based on other monomers^{115,155}. Polyglycerol (PG) based microgels are promising candidates for drug delivery and protein carriers, due to their high biocompatibility^{156–160}. These polymers can be synthesised with various architectures¹⁶¹. For instance, particle can contain a hyperbranched or a subparticle architecture. Hyperbranched particles are synthesised by mini-emulsion techniques and provide a high molecular weight as well as a dendritic polymer network^{112,162}. However, in microgels with subparticles, the small particles are connected via linear cross-linkers leading to a larger particle¹⁶³. In particular microgels containing subparticles provide huge potential in drug delivery, due to the possibility of double drug incorporation into the polymer network. Drug loading into the polymer matrix can be realised by two strategies. One strategy is based on diffusion of the guest molecule into the polymer matrix¹⁵⁹. Disadvantages in this method are the low entrapment and the possible inactivation of the guest molecule. A better method to afford a drug delivery system is achieved by encapsulation of the drug during polymer synthesis. This method provides high encapsulation rates and a uniform guest molecule distribution within the polymer matrix.

A promising method is particle degradation triggered by biological stimuli to ensure a controlled and homogeneous drug release¹⁶². Thereby, chemical bonds, which can easily be broken, e.g. acetal¹⁶⁴, ketal^{165,166} or phosphate esters¹⁶⁷, can be incorporated in the particles. Hence, particle degradation is initialised as a response to biological media like pH or reducing agents¹⁶⁸. Particle residues may easily be cleared by the kidneys, thus avoiding or reducing damage to the body due to toxic components¹⁵⁶. Compared to other particle degradation mechanisms, such as enzymatic cleavage, hydrolysis of acid labile bonds provides two benefits. First, fast diffusion of the protons ensures rapid particle degradation without steric hindrance and second, the acid environment of tumour cells does not need no additional protons to initialise the degradation process^{169,170}. However, particle degradation is not fully understood up to now. South and Lyon showed N-isopropylmethacrylamide (PNIPMAN) particle degradation via AFM¹⁷¹. Therefore, they removed the wafer with deposited PNIPMAM particles after certain time points from the incubation solution. The AFM scans were carried out in ambient conditions. However, an in situ study of the degradation process is still missing, which is essential for the knowledge of the degradation kinetics in biomedical application. For this purpose AFM in particular is a suitable method to observe the degradation process in lateral and vertical dimension as well as the surface topology of the particle in short time.

This chapter discusses the particle degradation of pH-responsive microgels (IPG-dPG microgels) based on linear(IPG) and dendritic (dPG) polyglycerol with an acid labile acetal bond, to get a better understanding of the degradation process on the molecular scale. The acetal cleavage within the IPG-dPG microgels can be understood as a "decross-linking" step back to the starting macromonomers. It has been shown that the particle height decreases exponentially, while the particle width exhibits less impact on the particle degradation. Furthermore, the Young's modulus has been also studied during degradation process. The experiments have been performed via AFM. The particles were obtained from the Haag group at the Freie Universität Berlin and were synthesised by Dirk Steinhilber.

9.2 Results

9.2.1 Microgel degradation at the surface

The microgels were spin coated on a gold coated silicon wafer for 300 s at 2000 rpm. At first, IPG-dPG microgels were imaged in pH 9 solution to determine particle size and shape in the swollen and stable state. Afterwards, the pH 9 solution was removed, while a pH 4 solution was injected to initialise the degradation process.

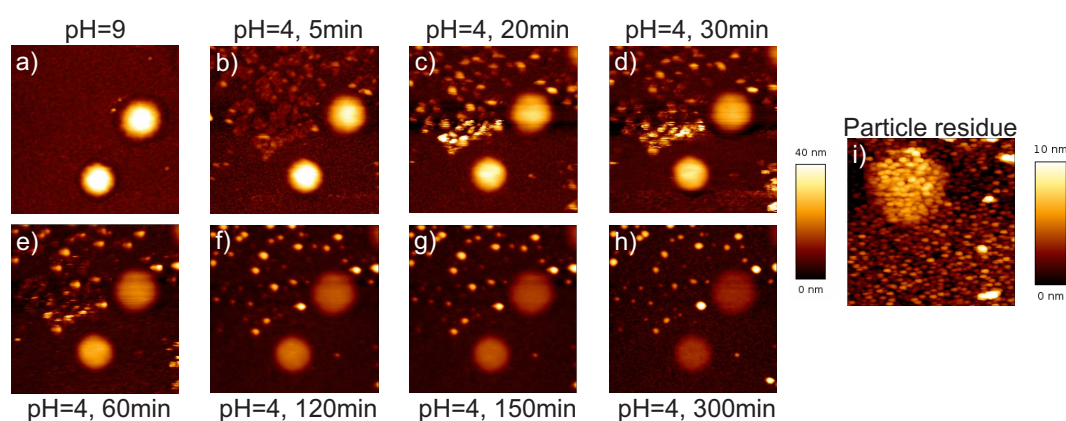


Figure 9.1: AFM images of the IPG-dPG microgel at pH 9 and pH 4 as a function of time. Scan size: $5 \times 5 \mu\text{m}$; Particle residue was taken under ambient conditions with a scan size of $2 \times 2 \mu\text{m}$.

Figure 9.1 shows the AFM images for the particle degradation at pH 9 and pH 4 as a function of time. It should be noted that the top row shows AFM images at small time intervals, while the bottom row shows AFM images over a larger time scale. Figure 9.2 depicts the particle volume in pH 9 and pH 4 solution as a function of time. The large particles volume in the stable state at pH 9 decreases tremendously with the exposure at acid solution to pH 4. In particular, the first 30 minutes seem to be important for particle degradation, since the particle volume decreases about 2.5 times of its initial volume at pH=9. However, the particle volume reaches a plateau after 180 minutes and does not change significantly. From AFM images and calculated particle volume, it is possible to gain information on the time scale of the degradation process. However, information on the mechanism of the degradation process are not accessible. In order to get a better understanding of this process particle cross section (Figure 9.3), particle height (Figure 9.4a), and particle width (Figure 9.4b) were plotted to study the particle degrad-

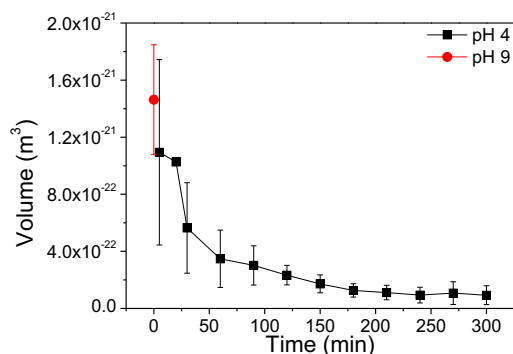


Figure 9.2: Particle volume of IPG-dPG microgels as a function of time at pH 9 and pH 4.

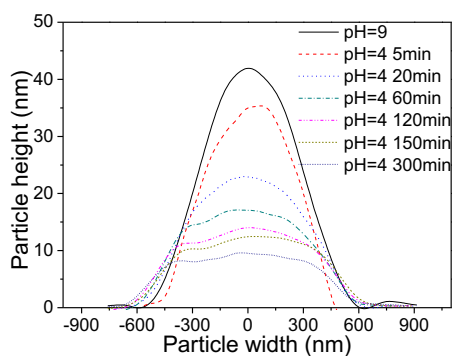


Figure 9.3: The corresponding particle cross sections of the AFM images as a function of time at pH 9 and pH 4.

ation in lateral and vertical dimension. Particle cross section and particle height show a decrease in vertical direction from about 40 nm to about 15 nm within 60 minutes, which is more than half of the initial particle height at pH=9. The particle erosion decelerates between 60 minutes until a plateau is reached at 180 minutes. As shown in Figure 9.4a), the particle height can be fitted with an exponential function which reveals a degradation rate of $k = 1/t = 0.02 \text{ min}^{-1}$. Interestingly, the particle shape changes from a smooth shape at pH=9 to a crater-like shape after exposure to pH=4 solution for 120 minutes. Note that the differences in the values between particle cross section and particle height arise from data treatment. The cross section represents only one particle, while the particle height is an average over three particles. In contrast to the particle height, the particle width increases from about 1000 nm to 1200 nm within 60 minutes. Further progress shows again a decrease in the particle to its initial lateral dimension. The particle apparently degrades from the outer particle surface to the particle inner structure.

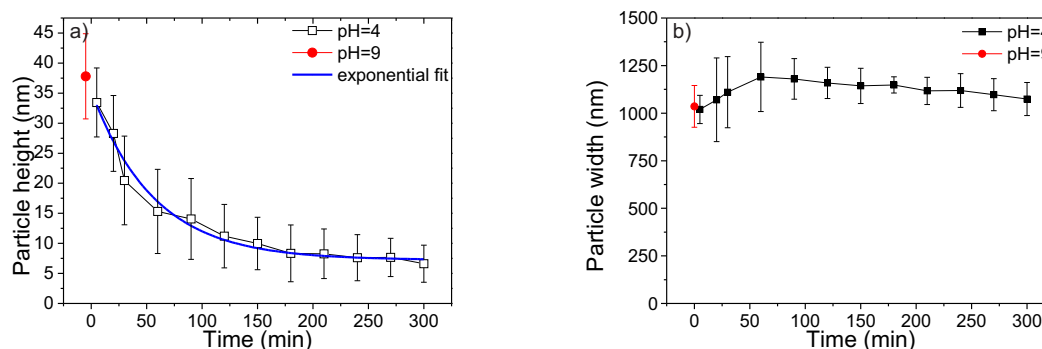


Figure 9.4: Particle height (a) and particle width (b) of IPG-dPG microgels as a function of time at pH 9 and pH 4.

After particle degradation was finished the particle residue was imaged at ambient conditions to understand the complete degradation process. To avoid any desorption of the particle residue, the solution was allowed to evaporate. Figure 9.1i) shows particle residues under ambient conditions. The pattern of a degraded particle exhibits a height of about 6 nm and indicates degradation of the particle back to their starting macromonomers.

9.2.2 Force measurements during particle degradation

To understand the inner morphology of particle during the particle degradation, force measurements were performed on three individual wafers and the Young's modulus was averaged over three particles. Figure 9.5 shows the Young's modulus as a function of time at pH 9 and pH 4. The particles show their lowest stiffness at pH 9. Their stiffness increased from about 380 kPa to 580 kPa with decreasing pH. Subsequently, a dramatic increase in particle stiffness is observed after 30 minutes. Afterwards particle stiffness decreases to about 580 kPa. The Young's modulus of the particles was only recorded and analysed up to 150 minutes of particle degradation, due to small particle sizes after 150 minutes.

9.2.3 Real time particle degradation via constant force mode

The *in-situ* particle degradation cannot only be studied by imaging the particles but also by measuring the particle height evolution in the constant force mode. In this mode the applied force is kept constant, while the height is readjusted by the piezo element. Figure A.18 shows the real time scan during particle degradation. The particle height is plotted against the time at pH 4. In an

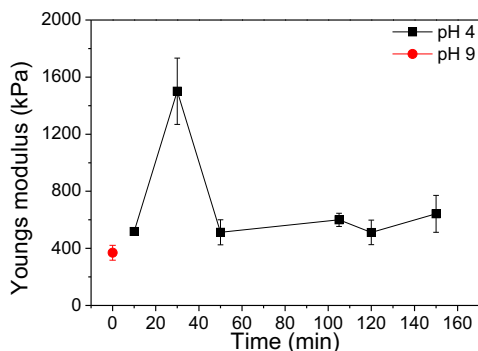


Figure 9.5: The Young's modulus of the IPG-dPG microgels as a function of time at pH 9 and pH 4.

acidic environment, the particle height decreases with time. No exponential decay is observed. However, a linear decay takes place at the beginning of particle degradation. After one hour the curve exhibits a slight exponential decay. The linear decay in the beginning of the experiment could result from the thermal drift of the piezo in z-direction (see inset Figure A.18)

9.3 Discussion

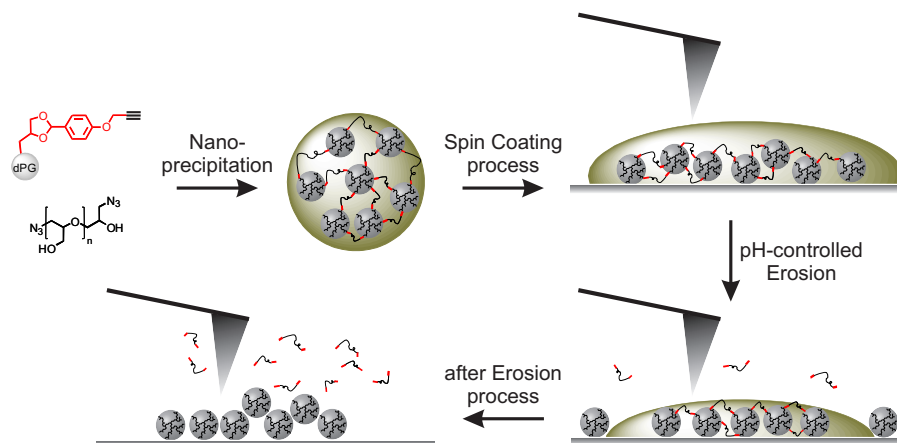


Figure 9.6: Synthesis and degradation mechanism of PG particles.

The particle degradation of IPG-dPG microgels can be induced by changing the pH from basic to acidic medium. The IPG-dPG microgels studied are highly swollen at pH 9. This leads to the largest particle volume observed, due to the stable nature of the acetal bond in basic medium and the favoured

interactions between the polymer network and the solvent⁹. The decrease in particle volume is related to the weak acetal bonds in acid conditions thus causing an acetal cleavage and consequently starting the particle degradation. Most of the acetal cleavage and the resulting particle degradation take places within the first 30 minutes. The process is indicated by an exponential decay of the particle volume. This was expected, due to the high particle volume and the high amount of acetal bonds in the beginning of the degradation process.

Obviously, the degradation is clearly driven by the particle height. This effect is directly related to the particle morphology. The particles consist of small subparticles, which are connected to each other via linear and flexible cross-linkers¹⁶³. These subparticles rearrange in adsorbed particles as shown in Figure 9.6 leading to strong particle flattening and therefore larger particle surface. The large particle surface enhances the acetal cleavage in vertical direction resulting in a rapid decrease in the particle height. The acetal cleavage can be understood as a "decross-linking" step into the starting macromonomers. The smaller cross-linker (IPG) resolves in the surrounding solution, while the heavier dPG subparticles remain at the surface. The "crater-like" structure in the particle cross section and the increase in particle width during the degradation process confirm the adsorption of heavier subparticles on top and at the periphery of the particles as shown in Figure 9.6. If the "decross-linking" step takes place, one would expect a particle shape pattern of the subparticles after the degradation process. This is indeed the case. AFM measurements under ambient conditions show a particles shape pattern with a height of around 6 nm indicating a bilayer of the dPG subparticles, which have a size of around 3 nm¹⁷².

Results obtained from force measurements match the results from imaging experiments. The lower particle stiffness at pH 9 is related to the highly swollen state of the particle and the uninfluenced acetal bonds in the basic environment. Thus, the particle remains flexible leading to a soft polymer network. The acid environment affects a collapse of the particle morphology leading to particle stiffening. The large increase in particle stiffness after 30 minutes is related to a fast degradation rate of the particle, which takes place between 20 and 40 minutes. Hence, this fast particle degradation within this time interval leads to particle contraction and particle stiffening. Afterwards, the particle degradation slows down and the polymer network of the particle relaxes. This results in a particle softening to 580 kPa.

Results from imaging experiments and real time force measurements are complementary and perfectly match. On the one hand, AFM images record

the changes on the particle surface meaning that the whole particle shape is analysed. On the other hand, in the constant force mode the tip penetrates and records the differences in the particle interior. In other words, the degradation at the particle surface proceeds in a non-uniform manner, while the particle degradation in the particle interior is very homogeneous. However, the result from the real time force measurement should be handle with care, since a thermal drift of the piezo in z-direction could take place.

9.4 Conclusion

This chapter discusses *in-situ* particle degradation of IPG-dPG microgels, which were obtained from the Haag group at the Freie Unisversität Berlin, via AFM technique and thus a detailed understanding of this process is provided. The IPG-dPG microgels, which are stable under basic conditions, show fast particle erosion in acidic environment. Studying the degradation by AFM provides simultaneous information about change in height and width. The particle height decreases exponentially as a function of time, which is mainly affected by the particle height. While the particle height decreases, the particle width increases in the beginning of the particle erosion. Furthermore, the particle cross-section indicates a crater-like structure. This indicates that particles undergo a "decross-linking" step into their starting macromonomers (cross-linker (IPG) and dPG sub-compartments). The lighter cross-linker (IPG) resolves in the solution, while the heavier dPG sub-compartments remain at the surface. Measurements under ambient conditions support this "decross-linking" step indicating a particle shape pattern.

The increasing Young's modulus during particle degradation is a direct result of acetal scission, due to the "decross-linking" of the IPG-dPG microgels into their smaller and stiffer starting macromonomers.

Furthermore, a real time scan of the degradation process in the constant force mode was performed. As expected the particle height decreases with time at pH 4. It was shown that the particle height decreases linearly and not exponentially as in the imaging experiments. This can be explained by uniform degradation in the particle interior.

9.5 Outlook

With the knowledge of the mechanism of particle degradation, the release of drugs could be study in detail. A fundamental understanding of the drug dis-

tribution within the particle could be accessible. Further experiments could be performed with other chemical labile functional groups. For instance basic labile bonds could be incorporated to fabricate drug delivery systems for desired applications.

Following the degradation at different temperatures could also be an interesting experiment to use such systems for biological applications. Furthermore, the particle degradation can be triggered by different external parameters such as light exposure and one should thoroughly investigate this effect.

Chapter 10

Conclusion and Outlook

10.1 Conclusion

This PhD gives a detailed insight into the surface behaviour of responsive microgels in terms of their particle composition and external stimuli. Due to the high impact of those materials for application such as sensors and drug delivery, the understanding and improvement of the particle properties is still of importance. This work focuses on PNIPAM-based microgels, which have been synthesised with different co-monomers. The hydrophilic acrylic acid (AAc) and the amphiphilic allyl acetic acid (AAA) have been chosen in terms of their different hydrophobicity. Pure PNIPAM microgels serve as reference sample to differentiate in the microgel properties. The characterization of the synthesised microgels was performed mainly with AFM for studies at an interface and DLS for studies in bulk.

The synthesised microgels increases their particle size with increasing the co-monomer content. This finding is in good agreement with the literature. However, with increasing the hydrophobicity of the used co-monomer, the particle behaviour changes tremendously. Particles containing the amphiphilic AAA co-monomer show only *one*, while AAc particle show two volume phase transition temperatures (VPTT) in bulk. Both particle types show an increase in the VPTT towards higher temperatures. With increasing the AAA content, force indentation measurements reveal an increase in the particle stiffness above the VPTT, while their AAc counterparts show a steady decrease in the particle stiffness.

Bulk and adsorbed AAc microgels are mainly driven by electrostatic repulsion within the particles. However, AAA microgels show a more complex behaviour. The particle behaviour is strongly influenced by an interplay

between hydrophobic effects and electrostatic repulsion within the particles. The electrostatic repulsion are attributed to the co-monomer charges, while the hydrophobic effects arise from the longer alkyl chain of the co-monomer. Due to a long-chained co-monomer, two features for PNIPAM-co-AAA microgels are accessible. The particle properties below the VPTT are mainly dominated by electrostatic repulsion, while the hydrophobic attraction between the co-monomer and the polymer backbone influences the particle behaviour above the VPTT.

Another part of this thesis was the impact of the solvent quality on the particle behaviour. The bulk behaviour was object in various publications. However, there is a poor understanding of particle behaviour in response to the solvent quality. The particle behaviour of pure PNIPAM particle and particles containing AAA depending on the solvent quality has been investigated in terms of the solvent polarity and their impact on applications. The particles show a pronounced co-non-solvency effect in bulk as well as at an interface. The minimum in the particle size appears at solvent content of 10-20 % in bulk, while the particle size minimum shifts to a solvent content of 40-50 % at the interface. The shift in the particle size minimum at the interface can be related to the reswelling process. The water content within the particle increases faster compared to the organic solvent content during the reswelling process, due to the high water affinity of the particles. Hence, a higher organic solvent content in the water/organic solvent mixture is needed to reach the particle size minimum. Furthermore, it has been shown, that the particles show a pronounced deswelling behaviour in vertical direction, while the deswelling ability in the lateral direction is restricted, due to the interaction between the particle and interface. The particles show a complete different behaviour at ambient conditions. It has been shown, that both particle types, pure PNIPAM and AAc containing particles, experience an increase in the particle volume with increasing the organic solvent content in the water/organic solvent mixture. This can be explained by organic solvent entrapment within the polymer network during the spin coating process. The swift removal of the surrounding water/organic solvent solution and the particle collapse from the particle periphery to the particle interior afford the organic solvent entrapment. The increase in the particle volume depends considerably on the organic solvent polarity as well as the cross-linking degree of the particle. The swelling ability from ambient conditions to the liquid state shows a dependency to electrostatic nature of the particle and the solvent quality. Particles with a high charge density exhibit a stronger swelling

behaviour than lower charged particles. This difference in the swelling capability is driven by the electrostatic repulsions within the particles, which set in during the swelling process. Furthermore, the swelling ability decreases with increasing the organic solvent content in the water/organic solvent mixture, due to the initialisation and domination of the co-non-solvency effect.

Furthermore, the swelling ability of AAA microgels on different surface coatings has been studied during several heating/cooling cycles. The investigations reveal, that the swelling ability of the particle depends strongly on the chemical nature of the polyelectrolyte and layer thickness.

Particles spin coated on thinner layers show a pronounced shrinking/swelling ability in lateral dimension, while a lateral and vertical shrinking/swelling is observed for particles spin coat on thicker multilayers. The behaviour of particles spin coated on thinner layers is of electrostatic nature due to the small penetration depth of the particles. The situation changes with increasing the layer thickness. Hence, the particles penetrate deeper into the multilayers leading to additional interactions. The interpenetration of the multilayers into the particles and the internal roughness of the multilayers lead to a restriction of the polymer network during the individual heating/cooling cycles resulting in a hysteresis behaviour of the particles in lateral and vertical dimension.

The hydrophobic nature of the particle containing AAA, which was observed in chapter 5, has been used to develop new light-responsive sensor systems. Therefore, a positively charged photo-sensitive azobenzene surfactant has been incorporated into the negatively charged particles leading to a microgel/surfactant complex. An increase in the surfactant concentration leads to a particle collapse and precipitation of the complex due to charge compensation. The particle contraction is more effective for particles containing higher co-monomer content compared to the ones containing less co-monomer. The particle size can not only be manipulated with the surfactant content but also by UV-VIS irradiation. Therefore, the ability of the surfactant to switch from its *trans*- to its *cis*- was used to change the particle size. The crucial point for this experiment is the different hydrophobicity of the two configurations, which leads either to binding and contraction or to a release and consequently reswelling of the microgel/surfactant complex.

In context of this PhD thesis, several particles obtained from other groups have been studied. Particles containing different polyethyleneglycol (PEG) content were obtained from the Prud'homme group. It has been shown, that the particle stiffness strongly depends on the PEG content. With increasing the PEG content the particle stiffness increases, which indicates a compact

polymer network. The incorporation of small nanoparticles at a constant PEG content has a minor effect on the particle stiffness.

Furthermore, particles containing polyethyleneglycerol obtained from the Haag group have been investigated. The results reveal that the particle stiffness not only depends on the co-monomer content but also on the chemical connection of the particle. The particles from the Haag group have been also used to perform the first *in situ* particle degradation by AFM. The particle volume decreases exponentially within the first 30 minutes. Afterwards the particle degradation slows down until an equilibrium is reached. Remarkably, the particle does not disappear moreover it is separated into their single polymer segments.

10.2 Outlook

The current work should focus on the improvement and advancement of the shown results to implement such materials to an application. The incorporation of co-monomers into PNIPAM particles impacts the microgels properties tremendously. The next step is the incorporation of longer chain carbon acids to study the interplay between charges and hydrophobicity intensively. Thus, an stronger increase in particle stiffness should be observed, while the VPTT of the particles should decrease to lower temperatures. One should think about new PNIPAM based microgels. Here the incorporation of adamantane molecule seems to be interesting. The adamantyl sidechain should have a huge impact on the swelling ability of the particle due to the restrict adamantane structure. Furthermore, the hydrophobicity and particle stiffness of such particles should change dramatically. Beside the adamantyl sidechain, the incorporation of crown ether into the particles are also promising to develop specific ion catcher.

The study of the co-non-solvency effect of adsorbed microgels should be continued, due to potentially high impact in sensor applications. Thus, an interesting point is to combine the thermo-sensitivity and co-non-solvency behaviour of the microgels. The question arises what happens if an already collapsed particle (by the co-non-solvency effect) is heated above their VPTT. Would the increase in temperature enhance the particle collapse? Is there a counter-effect due to the thermo-sensitivity and the co-non-solvency effect or is there a more pronounced particle collapse by these two external stimuli? This subject should be clarified. Besides the thermo-sensitivity of the microgels, the influence of the underlying multilayer plays also a crucial role

in the microgel behaviour. Therefore, it is interesting to study the co-non-solvency effect of microgels adsorbed on different multilayer systems. The multilayer systems restrict the shrinking performance of the microgels during the heating/cooling cycles. The question is if the particle shrinking induced by the co-non-solvency effect overcomes the particle restriction leading to a stronger deswelling of adsorbed particle compared to temperature-induced particle shrinking. The difficulty of this experiment is sensitivity of such multilayer systems to organic solvent leading to a challenging task.

The light-induced size manipulation of microgel/surfactant complexes was studied in this thesis, but research of such complexes offer much potential for application and has to be study in more detail. For instance, longer chained surfactant should be studied to get a better understanding of the interplay between the surfactant and the particle. Neutron scattering provides the possibility to gain information about the internal structure of the microgel/surfactant complex. Another interesting point is the switching behaviour of such microgel/surfactant complexes in their adsorbed state. Here, two strategies can be followed. First, the microgel/surfactant complexes is formed in the bulk phase and afterwards adsorbed onto the surface. Second, the microgels will be spin coated at the surface and then the surfactant is added to form the microgel/surfactant complex. The question arises if the light-induced particle shrinking of both strategies is different? Furthermore, one can perform a *in-situ* particle switch to determine the time scale of the particle shrinking. Once the switching ability for adsorbed particles is clarified, a Janus particle can be used to develop movable particles simply induced by light. Such Janus particles should consist of a surfactant-binding side and a side, which does not interact with the surfactant. But not only the physically bonded microgel/surfactant complexes are of interest, but also the chemically ones could offer huge impact. The incorporation of covalently bonded photo-sensitive surfactant could be interesting for further application.

The knowledge of the particle degradation is tremendously important of medical application. Further investigations should focus on the drug delivery. The drug should be incorporated into the particles. Afterwards, the degradation process can be initialised and drug concentration in the supernatant can be determined. Thus, the distribution of the drug within particle can be determined.

Chapter 11

Appendix

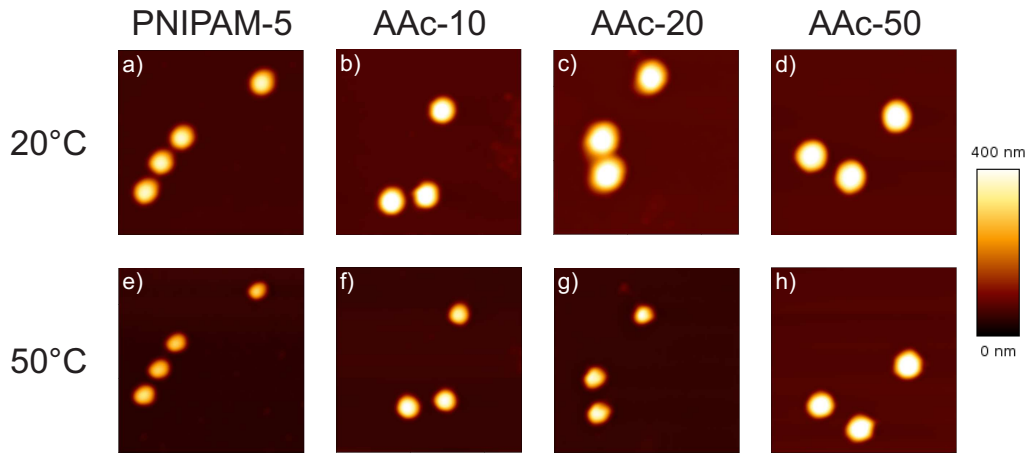


Figure A.1: AFM images of pure PNIPAM (a, e), AAc-10 (b, f), AAc-20 (c, g) and AAc-50 (d, h) at 20 °C (a,b, c, d) and 50 °C (e, f, g, h), respectively. Scan size: $5 \times 5 \mu\text{m}$

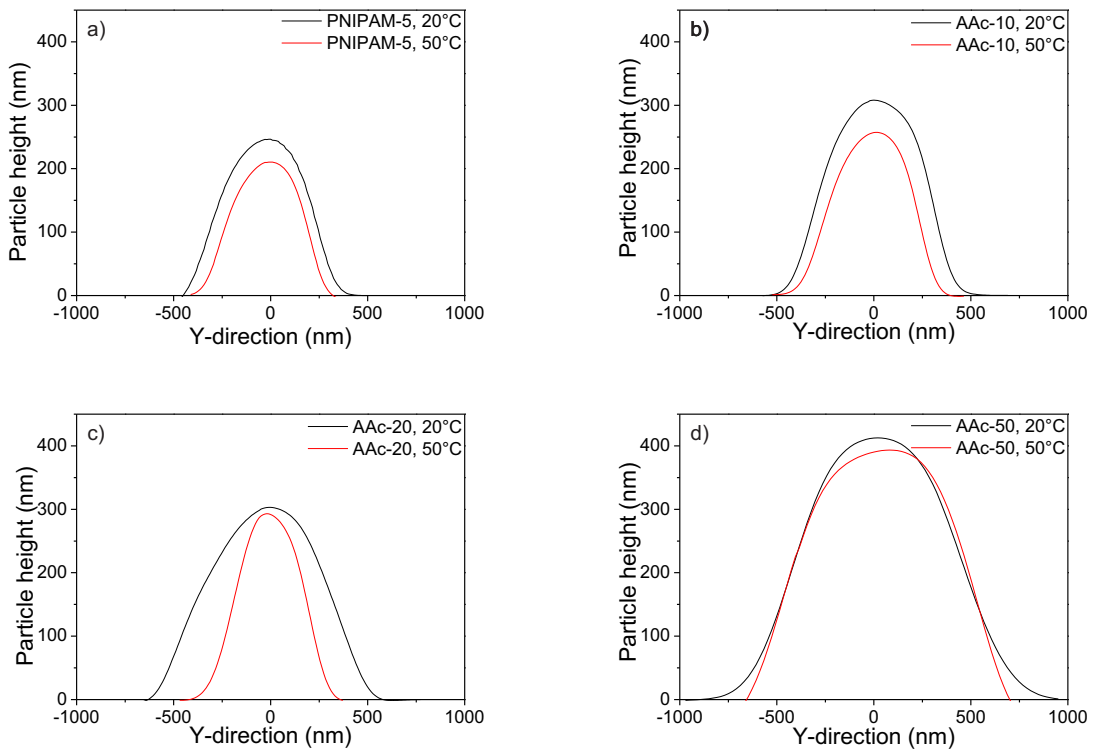


Figure A.2: Particle cross sections of PNIPAM-5 (a), AAc-10 (b), AAc-20 (c) and AAc-50 (d) at 20 °C and 50 °C, respectively.

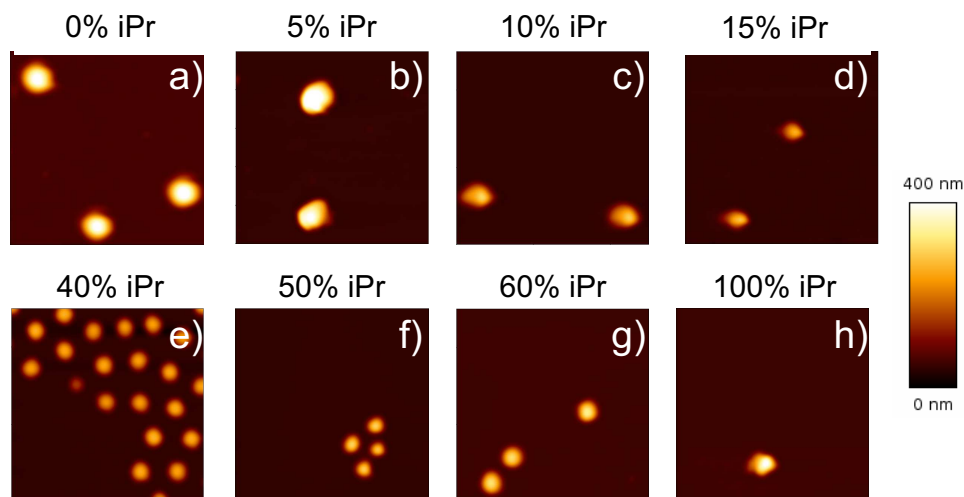


Figure A.3: AFM-images for PNIPAM-5 in liquid state at the surface for different water-iPr composition. Scan area: $5 \times 5 \mu\text{m}^2$.

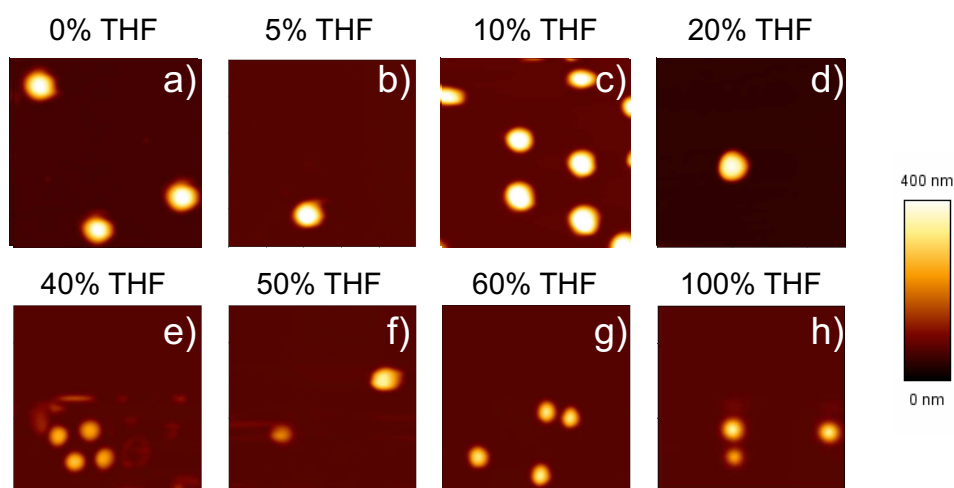


Figure A.4: AFM-images for PNIPAM-5 in liquid state at the surface for different water-THF composition. Scan area: $5 \times 5 \mu\text{m}^2$.

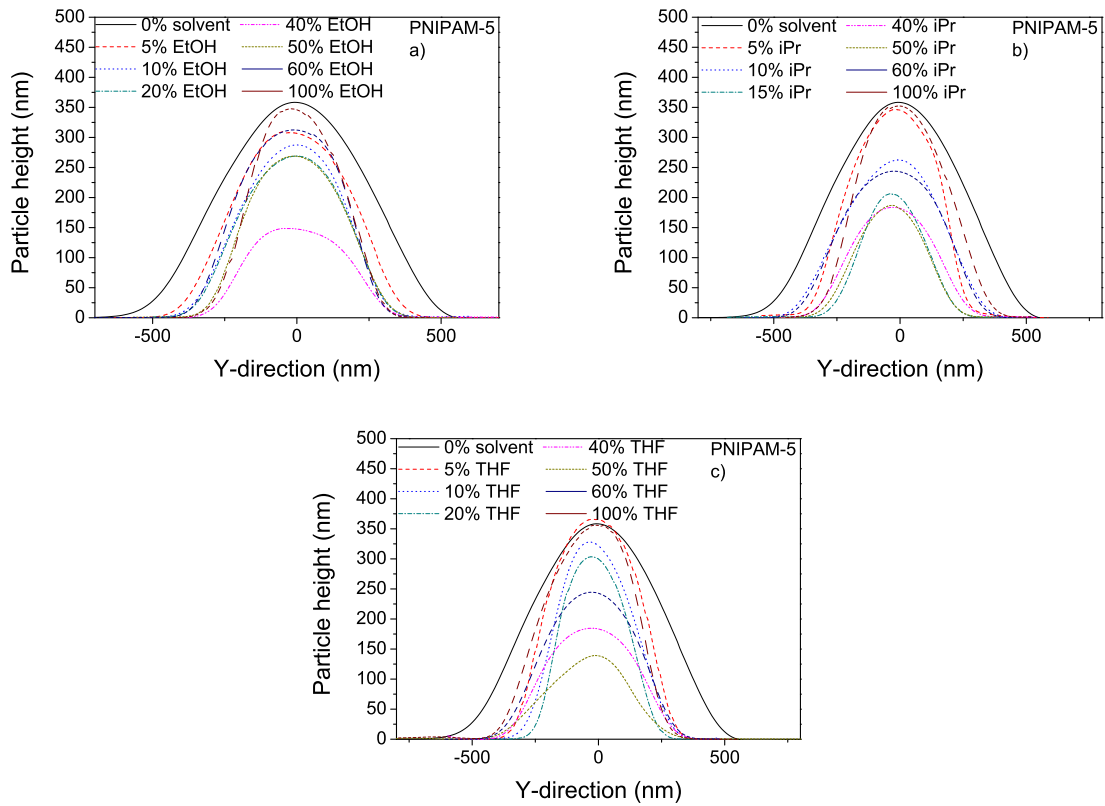


Figure A.5: Particle cross sections in a) EtOH b) iPr and c) THF mixtures of PNIPAM-5 spin coated from respective solvent mixture.

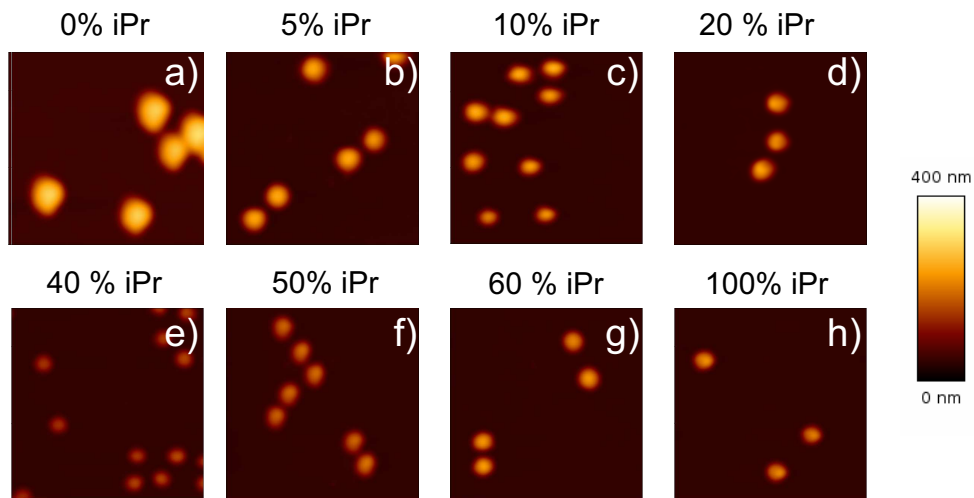


Figure A.6: AFM-images for AAA-5 in liquid state at the surface for different water-iPr composition. Scan area: $5 \times 5 \mu\text{m}^2$.

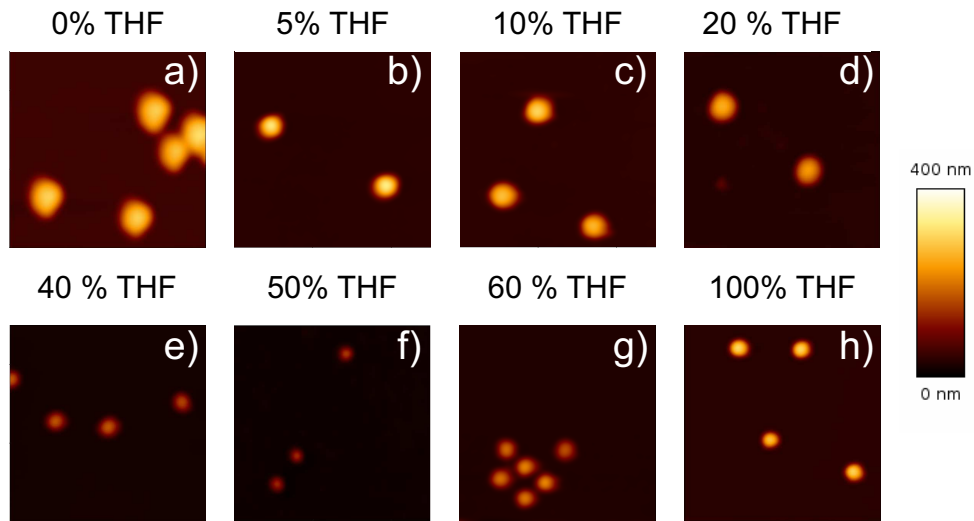


Figure A.7: AFM-images for AAA-5 in liquid state at the surface for different water-THF composition. Scan area: $5 \times 5 \mu\text{m}^2$.

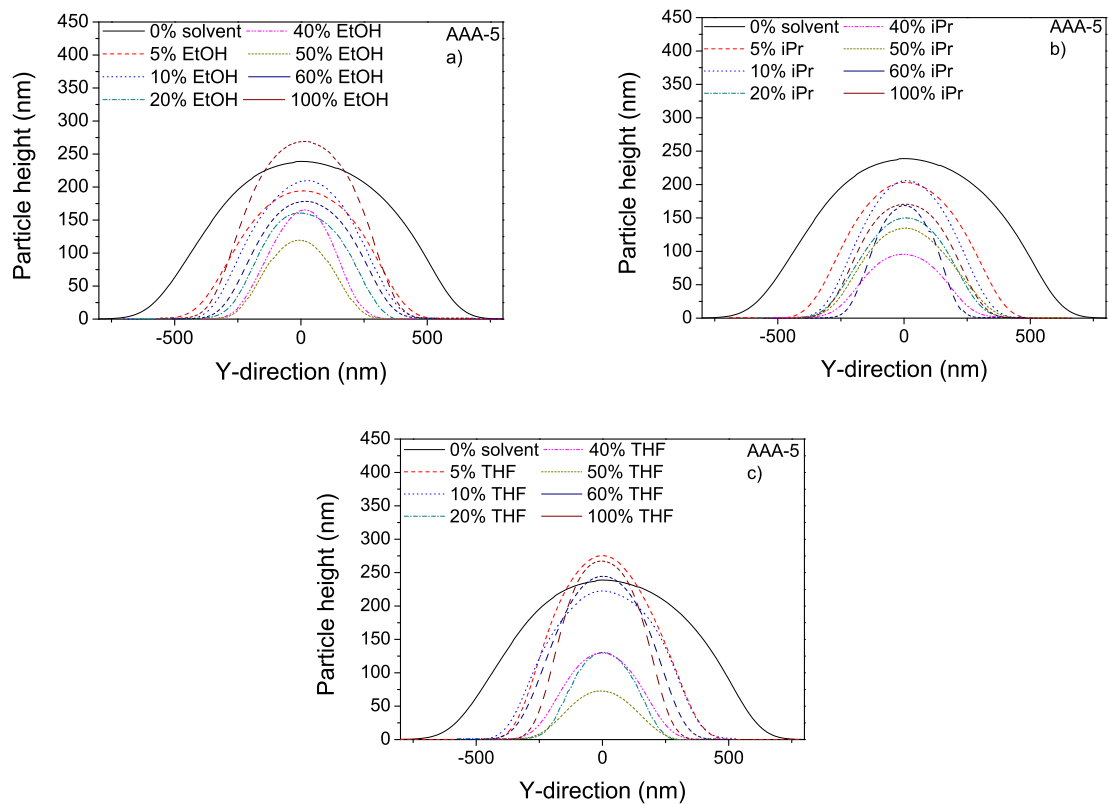


Figure A.8: Particle cross section of AAA-5 spin coated from different a) water-EtOH b) water-iPr and c) water-THF mixtures, respectively.

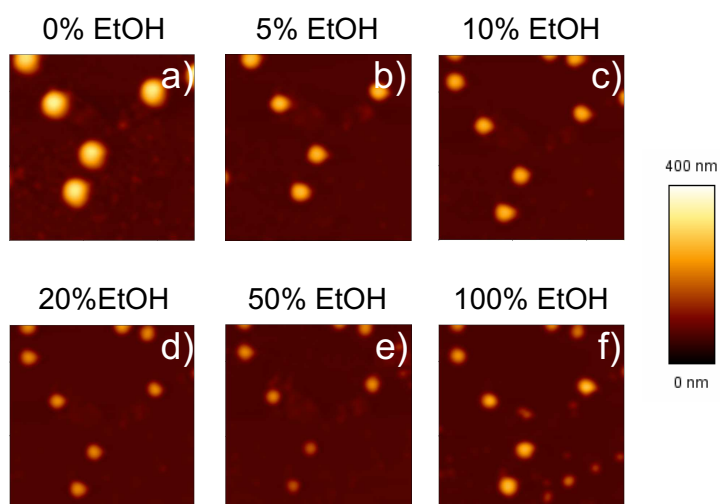


Figure A.9: AFM-images for AAA-5 spin coated from pure water in liquid state at the surface for different water-EtOH composition. Scan area: $5 \times 5 \mu\text{m}^2$.

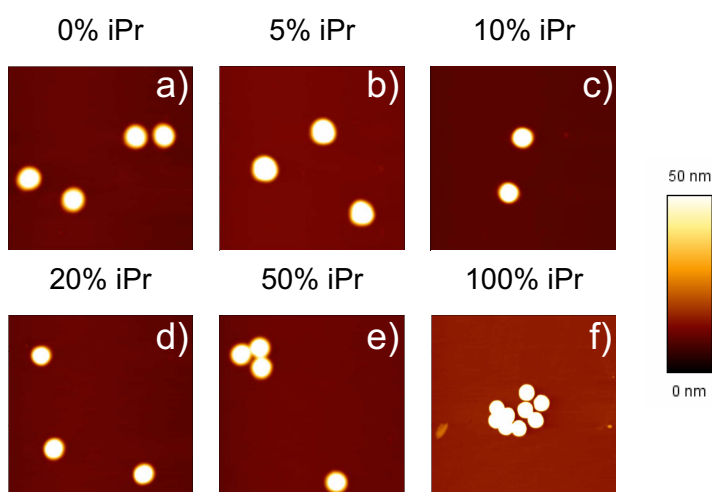


Figure A.10: AFM images of PNIPAM-5 in ambient conditions spin coated from different water-iPr compositions. Scan area: $5 \times 5 \mu\text{m}^2$.

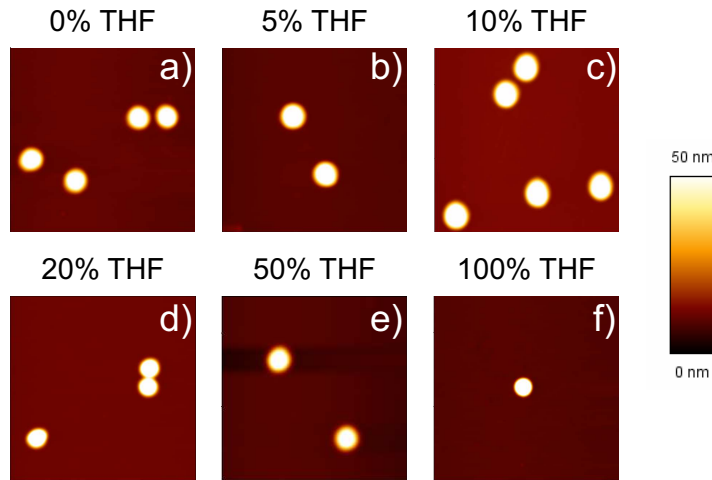


Figure A.11: AFM images of PNIPAM-5 in ambient conditions spin coated from different water-THF compositions. Scan area: $5 \times 5 \mu\text{m}^2$.

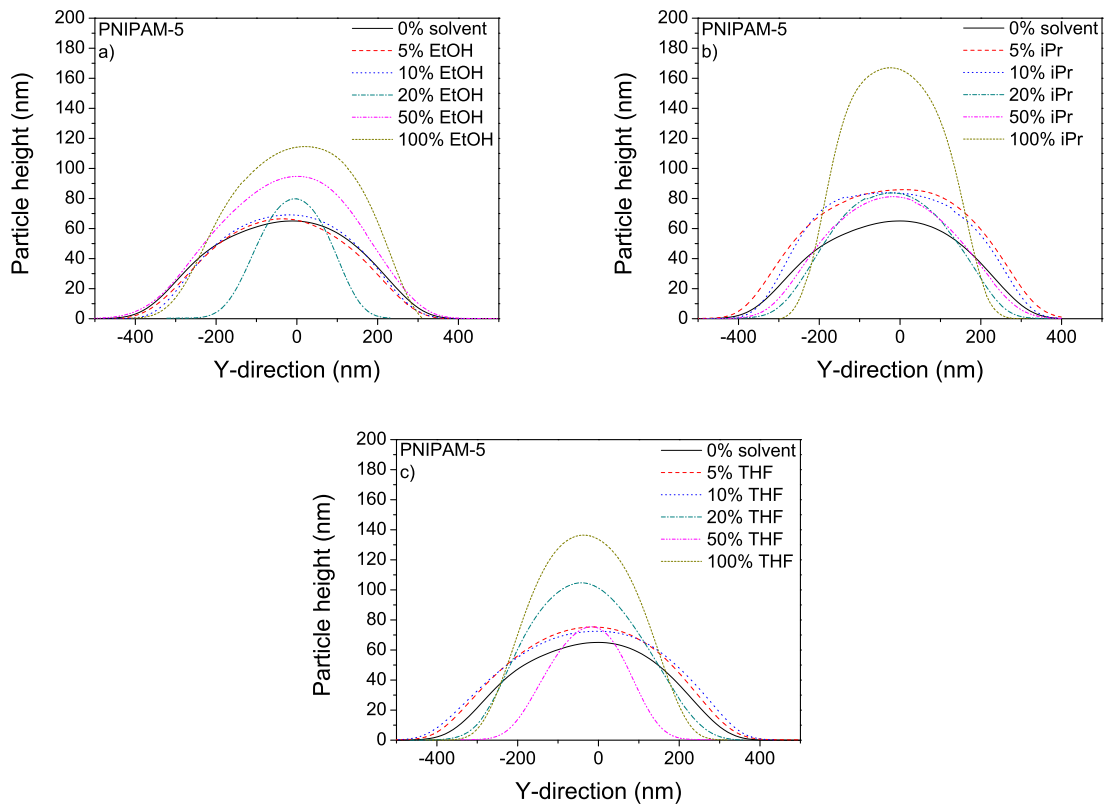


Figure A.12: Particle cross section of PNIPAM-5 in ambient conditions after spin coating from different a) water-EtOH b) water-iPr and c) water-THF mixtures, respectively.

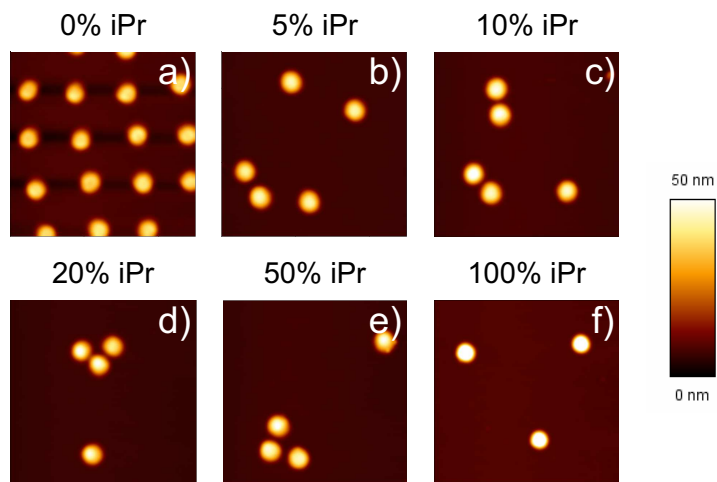


Figure A.13: AFM images for AAA-5 in ambient conditions spin coated from different water-iPr mixtures. Scan area: $5 \times 5 \mu\text{m}^2$.

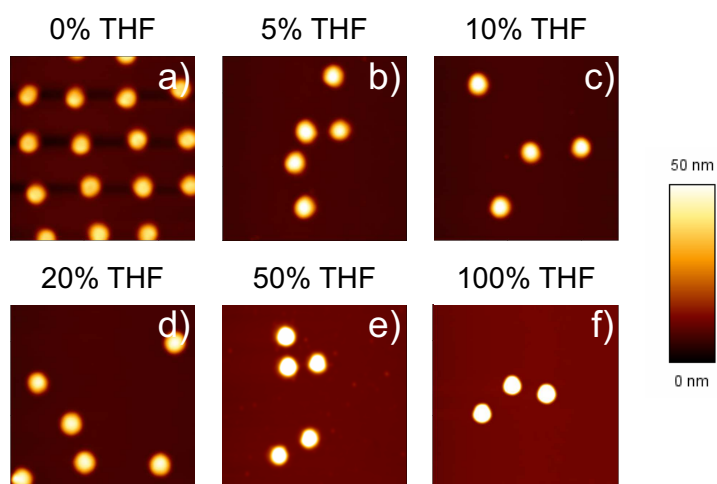


Figure A.14: AFM images for AAA-5 in ambient conditions spin coated from different water-THF mixtures. Scan area: $5 \times 5 \mu\text{m}^2$.

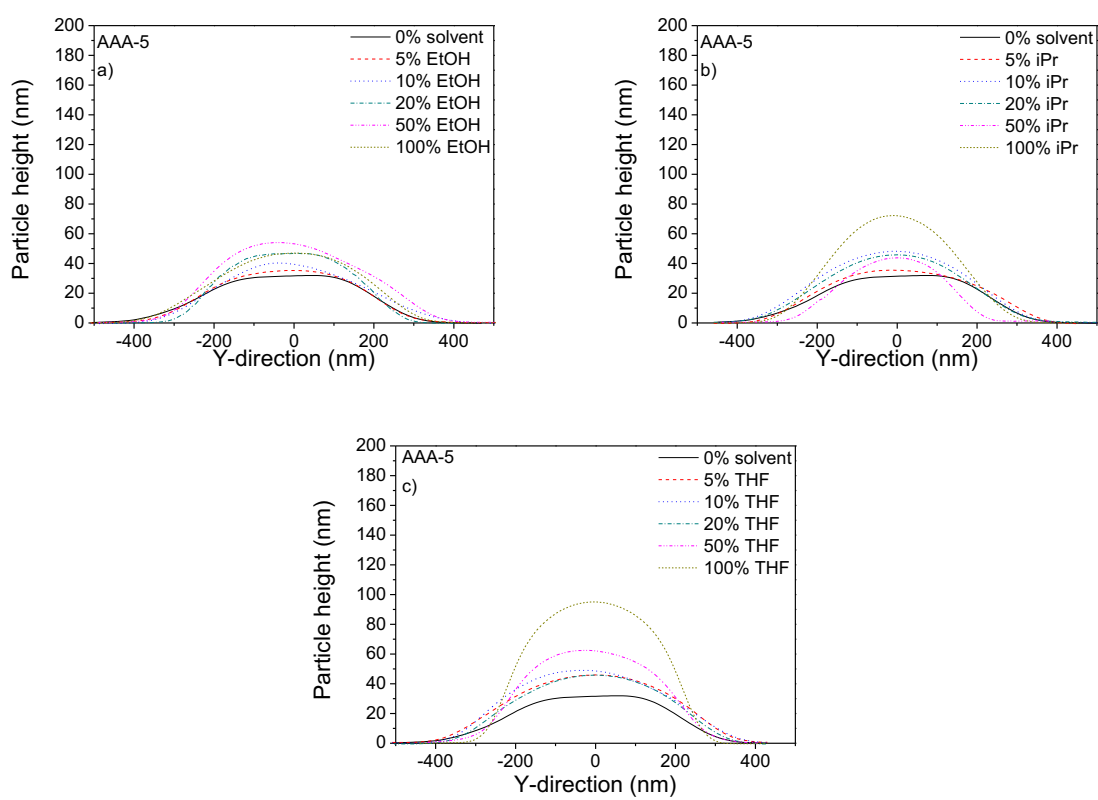


Figure A.15: Particle cross section of AAA-5 in ambient conditions spin coated from different a) water-EtOH b) water-iPr and c) water-THF mixtures, respectively.

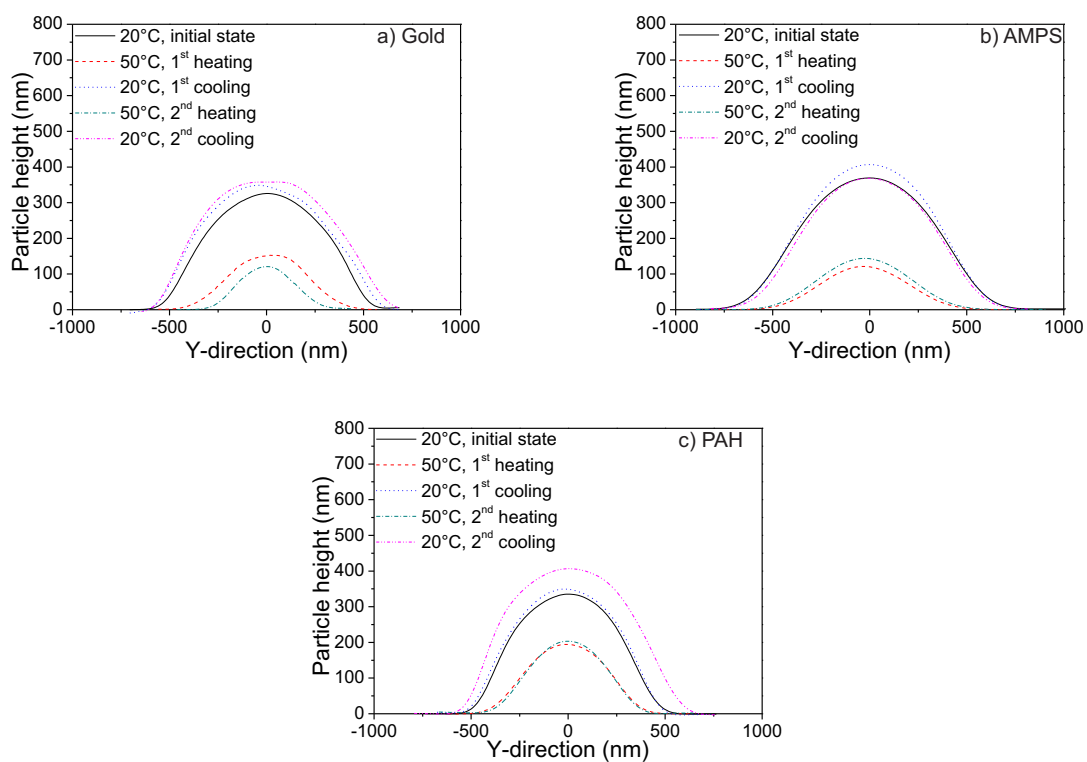


Figure A.16: Particle cross sections of P10 particles spin coated on (a) gold, (b) AMPS and (c) PAH layers during two heating/cooling cycles.

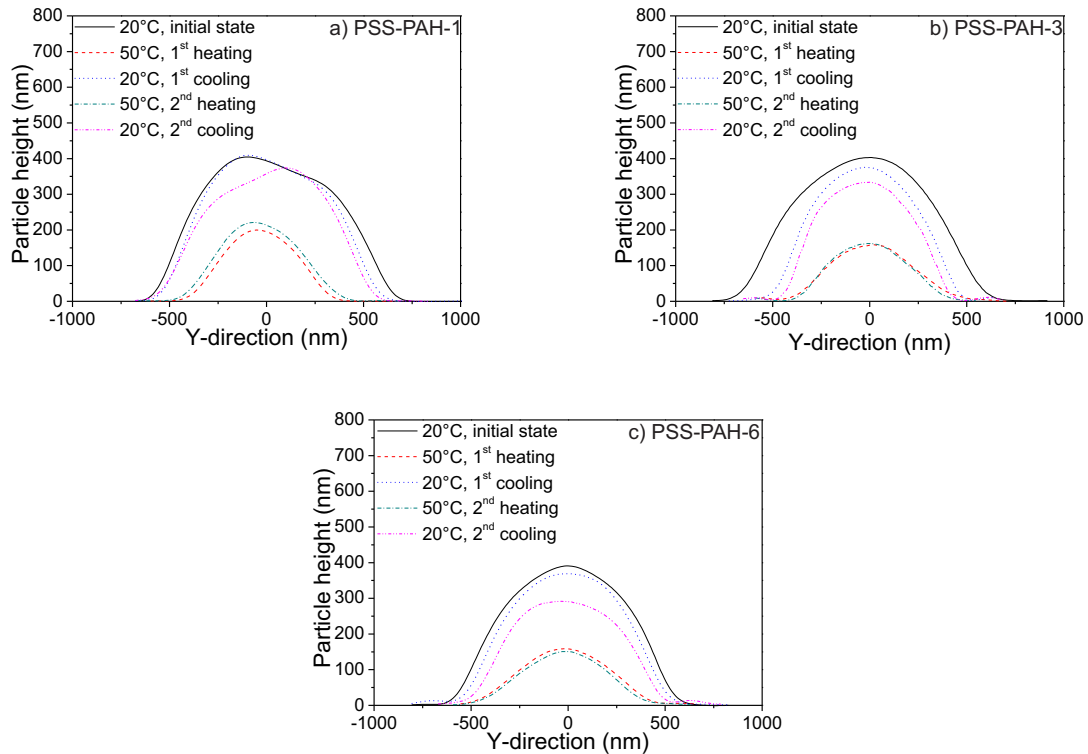


Figure A.17: Particle cross section of P10 particles spin coated on (a) PSS-PAH-1, (b) PSS-PAH-3 and (c) PSS-PAH-6 multilayers during two heating/cooling cycles.

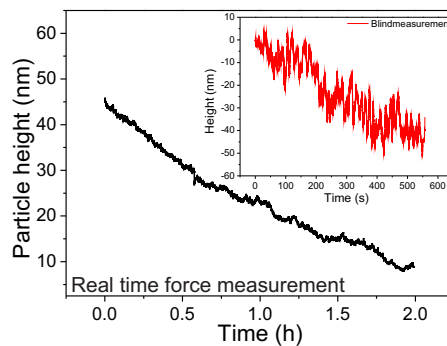


Figure A.18: Real time scan during particle degradation in constant force mode as a function of time. Inset shows the thermal drift in z-dimension of the AFM setup.

Abbreviations

$^{\circ}\text{C}$	degree Celsius
%	percent
\AA	angström
α	contact angle
α_w	deswelling ratio of particle width
α_h	deswelling ratio of particle height
α_v	deswelling ratio of particle volume
β	apparatus constant
χ	Flory-Huggin parameter
$\Delta\rho$	scattering contrast
ϵ_0	vacuum permittivity
ϵ_r	relative permittivity
η	dynamic viscosity
Γ	relaxation rate
κ	Debye length
λ	wave length
ϕ	volume fraction
Π	osmotic pressure
σ_s	surface energy
σ_{ls}	surface tension between liquid and surface
σ_l	surface tension of liquid
τ	correlation time
θ	scattering angle
ξ	correlation length
ζ	zeta potential
AAA	allyl acetic acid
AAA-5	particles with 5% allyl acetic acid
AAA-10	particles with 10% allyl acetic acid
AAA-20	particles with 20% allyl acetic acid
AAA-25	particles with 25% allyl acetic acid
AAA-50	particles with 50% allyl acetic acid
AAc	acrylic acid
AAc-10	particles with 10% acrylic acid
AAc-20	particles with 20% acrylic acid
AAc-50	particles with 50% acrylic acid
AMPS	3-aminopropyltrimethoxysilane

\vec{B}	magnetic field
BIS	N,N'-methyleneacrylamide
CMC	critical micelle concentration
D	diffusion coefficient
DLS	dynamic light scattering
\vec{E}	electric field
E	electric field
E	Young's modulus
EtOH	ethanol
<i>et al.</i>	et abtera
F	force
F	free energy
f_h	swelling ratio of particle height
f_v	swelling ratio of particle volume
f_w	swelling ratio of particle width
g^1	field autocorrelation function
g^2	intensity time autocorrelation function
h	particle height
H	enthalpie
H-bond	hydrogen bond
I	intensity
iPr	iso-propanol
JCNS	Jülicher Zentrum für Forschung mit Neutronen
k	spring constant
\vec{k}	wave vector
k_B	Boltzmann constant
kPa	kilopascal
KPS	potassium persulfate
m	metre
M	molar
MeOH	methanol
mg	milligram
min	minute
μm	micrometre
mM	millimolar
<i>mol - %</i>	mole percent
mV	millivolt
n	refractive index

N	number of particles
nm	nanometre
N_c	chain number of the polymer
N_c	Avogadro constant
NIPAM	<i>N</i> -isopropylacrylamide
NP	nanoparticles
P10	particles with 10% allyl acetic acid
PNIPAM	poly- <i>N</i> -isopropylacrylamide
PNIPAM-5	particles with 5% cross-linker
$P(q)$	form factor
p.a.	per analyse
PAH	polyallylamine hydrochloride
PDI	polydispersity index
PEI	polyethylenimine
PEG	polyethyleneglycol
PG	polyglycerol
PSS	polystyrene sulfonate
q	scattering vector
R	indenter curvature
R_h	hydrodynamic radius
rpm	rotation per minute
s	second
S	entropie
$S(q)$	structure factor
SANS	small angle neutron scattering
SEM	scanning electron microscopy
Si	silicon
T	temperature
THF	tetrahydrofuran
TRIS	tris(hydroxymethyl)aminomethane
UV	ultra violett light
v	molare volume
V	particle volume
VIS	visible light
VPT	volume phase transition
VPTT	volume phase transition temperature
VPTT(imaging)	VPTT obtained from imaging experiments
VPTT(force)	VPTT obtained from force experiments

w	particle width
wt-%	weight percent
x	deflection
Z	charge ratio

List of publication

1. Marcel Richter, Melanie Hunnenmörder and Regine v. Klitzing, The impact of the co-non-solvency effect on PNIPAM microgels at interfaces, *Colloid and Polymer Science* 2014, 292, 2439-2452. (Chapter 6)
2. Marcel Richter, Dirk Steinhilber, Rainer Haag and Regine v. Klitzing. Visualization of real time degradation of polyglycerol via Atomic force microscopy, accepted for publication in *Molecular Rapid Communication*. (Chapter 9)
3. Marcel Richter, Yuriy Zakrevskyy, Michael Eisele, Nino Lomadze, Svetlana Santer and Regine von Klitzing. Effect of pH and co-monomer content on the swelling behaviour of microgel-photosensitive surfactant complex, accepted for publication in *Polymer*. (Chapter 8)
4. Anna Burmistrova, Marcel Richter, Cagri Uzum and Regine von Klitzing. Effect of cross-linker density of P(NIPAM-co-AAc) microgels at solid surfaces on the swelling/shrinking behaviour and the Young's modulus, *Colloid and Polymer Science*, 2012, 289(5-6), 613-624.
5. Anna Burmistrova, Marcel Richter, Michael Eisele, Cagri Üzüüm and Regine von Klitzing. The Effect of Co-Monomer Content on the Swelling/Shrinking and Mechanical Behaviour of Individually Adsorbed PNIPAM Microgel Particles, *Polymers* 2011, 3(4), 1575-1590.
6. Yuriy Zakrevskyy, Marcel Richter, Svitlana Zakrevska, Nino Lomadze, Regine von Klitzing and Svetlana Santer. Light-Controlled Reversible Manipulation of Microgel Particle Size Using Azobenzene-Containing Surfactant, *Advanced Functional Materials* 2012, 22(23), 5000-5009. (Chapter 8)
7. Haixia Zhou, Marcel Richter, Regine von Klitzing, and Rainer Haag. Multifunctional Dendritic Architectures: An Investigation of their Mechanical Properties, *Mater. Res. Soc. Symp. Proc.*, 2012, 1403, 195-200.
8. Stefan Wellert, Yvonne Hertle, Marcel Richter, Martin Medebach, David Magerl, Weinan Wang, Bruno Deme, Aurel Radulescu, Peter Müller-Buschbaum, Thomas Hellweg, and Regine von Klitzing, Internal structure of adsorbed ionic microgel films, *Langmuir* 2014, 30(24), 7168-7176.

9. Stefan Wellert, Marcel Richter, Thomas Hellweg, Regine v. Klitzing, Yvonne Hertle, Responsive Microgels at Surfaces and Interfaces, *Zeitschrift für Physikalische Chemie* DOI: 10.1515/zpch-2014-0568. (Chapter 2)

Bibliography

- [1] Klinger, D.; Landfester, K. *Polymer* 2012, *53*, 5209–5231.
- [2] Richtering, W.; Pich, A. *Soft Matter* 2012, *8*, 11423–11430.
- [3] Hamley, I. W. *Angewandte Chemie International Edition* 2003, *42*, 1692–1712.
- [4] Schild, H. G. *Progress in Polymer Science* 1992, *17*, 163–249.
- [5] Lyon, L. A.; Fernandez-Nieves, A. *Annual Review of Physical Chemistry* 2012, *63*, 25–43.
- [6] Senff, H.; Richtering, W. *Journal of Chemical Physics* 1999, *111*, 1705–1711.
- [7] Karg, M. *Colloid and Polymer Science* 2012, *290*, 673–688.
- [8] Liu, R.; Fraylich, M.; Saunders, B. R. *Colloid and Polymer Science* 2009, *287*, 627–643.
- [9] Nayak, S.; Lyon, L. A. *Angewandte Chemie International Edition* 2005, *44*, 7686–7708.
- [10] Hertle, Y.; Hellweg, T. *Journal of Materials Chemistry B* 2013, *1*, 5874–5885.
- [11] Karg, M.; Hellweg, T. *Current Opinion in Colloid & Interface Science* 2009, *14*, 438–450.
- [12] Chen, S.; Zhong, H.; Gu, B.; Wang, Y.; Li, X.; Cheng, Z.; Zhang, L.; Yao, C. *Materials Science and Engineering C* 2012, *32*, 2199–2204.
- [13] Peppas, N. A.; Huang, Y.; Torres-Lugo, M.; Ward, J. H.; Zhang, J. *Annual Review of Biomedical Engineering* 2000, *2*, 9–29.
- [14] Hoare, T. R.; Kohane, D. S. *Polymer* 2008, *49*, 1993–2007.

- [15] Kim, J.; Nayak, S.; Lyon, L. A. *Journal of American Chemical Society* 2005, *127*, 9588–9592.
- [16] Kim, J.; Serpe, M. J.; Lyon, L. A. *Angewandte Chemie International Edition* 2005, *117*, 1357–1360.
- [17] Ohashi, H.; Abe, T.; Tamaki, T.; Yamaguchi, T. *Macromolecules* 2012, *45*, 9742–9750.
- [18] Hu, L.; Sarker, A. K.; Islam, M. R.; Li, X.; Lu, Z.; Serpe, M. J. *Journal of Polymer Science, Part A: Polymer Chemistry* 2013, *51*, 3004–3020.
- [19] Song, S.; Hu, N. *Journal of Physical Chemistry B* 2010, *114*, 5940–5945.
- [20] Erel, I.; Zhu, Z.; Zhuk, A.; Sukhishvili, S. A. *Journal of Colloid and Interface Science* 2011, *355*, 61–69.
- [21] Liu, X.-W.; Zhu, S.; Wu, S.-R.; Wang, P.; Han, G.-Z. *Colloids and Surfaces A: Physicochem. Eng. Aspects* 2013, *417*, 140–145.
- [22] Nolan, C. M.; Serpe, M. J.; Lyon, L. A. *Biomacromolecules* 2004, *5*, 1940–1946.
- [23] Ito, T.; Sato, Y.; Yamaguchi, T.; Nakao, S. *Macromolecules* 2004, *37*, 3407–3414.
- [24] Daly, E.; Saunders, B. R. *Langmuir* 2000, *16*, 5546–5552.
- [25] Karg, M.; Pastoriza-Santos, I.; Rodriguez-Gonzalez, B.; von Klitzing, R.; Wellert, S.; Hellweg, T. *Langmuir* 2008, *24*, 6300–6306.
- [26] Costa, E.; Lloyd, M. M.; Chopko, C.; Aguiar-Ricardo, A.; Hammond, P. T. *Langmuir* 2012, *28*, 10082–10090.
- [27] Kratz, K.; Hellweg, T.; Eimer, W. *Colloids and Surfaces A: Physicochemical and Engineering Aspects* 2000, *170*, 137–149.
- [28] Snowden, M. J.; Chowdhry, B. Z.; Vincent, B.; Morris, G. E. *Journal of Chemical Society, Faraday Transactions* 1996, *92*, 5013–5016.
- [29] Zakrevskyy, Y.; Richter, M.; Zakrevska, S.; Lomadze, N.; von Klitzing, R.; Santer, S. *Advanced Functional Materials* 2012, *22*, 5000–5009.
- [30] Chen, Y.; Chen, Y.; Nan, J.; Wang, C.; Chu, F. *Journal of Applied Polymer Science* 2012, *124*, 4678–4685.

- [31] Garcia-Salinas, M. J.; Donald, A. M. *Journal of Colloid and Interface Science* 2010, *342*, 629–635.
- [32] Mohanty, P. S.; Richtering, W. *Journal of Physical Chemistry B* 2008, *112*, 14692–14697.
- [33] Li, Z.; Ngai, T. *Colloid and Polymer Science* 2011, *289*, 489–496.
- [34] Kleinen, J.; Klee, A.; Richtering, W. *Langmuir* 2010, *26*, 11258–11265.
- [35] Burmistrova, A.; Richter, M.; Eisele, M.; Üzüüm, C.; von Klitzing, R. *Polymers* 2011, *3*, 1575–1590.
- [36] Burmistrova, A.; Richter, M.; Üzüüm, C.; v. Klitzing, R. *Colloid and Polymer Science* 2011, *289*, 613–624.
- [37] Matzelle, T.; Ivanov, D.; Landwehr, D.; Heinrich, L.; Herkt-Bruns, C.; Reichelt, R.; Kruse, N. *Journal of Physical Chemistry B* 2002, *106*, 2861–2866.
- [38] Winnik, F. M.; Ringsdorf, H.; Venzmer, J. *Macromolecules* 1990, *23*, 2415–2416.
- [39] Scherzinger, C.; Lindner, P.; Keerl, M.; Richtering, W. *Macromolecules* 2010, *43*, 6829–6833.
- [40] Walter, J.; Sehr, J.; Vrabec, J.; Hasse, H. *Journal of Physical Chemistry B* 2012, *116*, 5251–5259.
- [41] Scherzinger, C.; Holderer, O.; Richter, D.; Richtering, W. *Physical Chemistry Chemical Physics* 2012, *14*, 2762–2768.
- [42] Scherzinger, C.; Schwarz, A.; Bardow, A.; Leonhard, K.; Richtering, W. *Current Opinion in Colloid & Interface Science* 2014, *19*, 84–94.
- [43] Heppner, I. N.; Islam, M. R.; Serpe, M. J. *Macromol Rapid Commun* 2013, *34*, 1708–1713.
- [44] Decher, G. *Science* 1997, *277*, 1232–1237.
- [45] Pelton, R. *Advances in Colloid and Interface Science* 2000, *85*, 1–33.
- [46] da Silva, R.; de Oliveira, M. G. *Polymer* 2007, *48*, 4114–4122.
- [47] Senff, H.; Richtering, W. *Colloid and Polymer Science* 2000, *278*, 830–840.

- [48] Karg, M.; Lu, Y.; Carbo-Argibay, E.; Pastoriza-Santos, I.; Perez-Juste, J.; Liz-Marzan, L. M.; Hellweg, T. *Langmuir* 2009, *25*, 3163–3167.
- [49] Deng, Y.; Pelton, R. *Macromolecules* 1995, *28*, 4617–4621.
- [50] Imran, A. B.; Seki, T.; Takeoka, Y. *Polymer Journal* 2010, *42*, 839–851.
- [51] Flory, P. J.; Rehner, J. *The Journal of Chemical Physics* 1943, *11*, 512–520.
- [52] Tanaka, T.; Fillmore, D.; Sun, S.; Nishio, I.; Swislow, G.; Shah, A. *Physical Review Letters* 1980, *45*, 1636–1639.
- [53] Kim, J.; Serpe, M. J.; Lyon, L. A. *Journal of American Chemical Society* 2004, *126*, 9512–9513.
- [54] South, A. B.; Whitmire, R. E.; Garcia, A. J.; Lyon, L. A. *Applied Materials and Interfaces* 2009, *12*, 2747–2754.
- [55] Burmistrova, A.; von Klitzing, R. *Journal of Materials Chemistry* 2010, *20*, 3502–3507.
- [56] Höfl, S.; Zitzler, L.; Hellweg, T.; Herminghaus, S.; Mugele, F. *Polymer* 2007, *48*, 245–254.
- [57] Clarke, K. C.; Lyon, L. A. *Langmuir* 2013, *29*, 12852–12857.
- [58] Schmidt, S.; Motschmann, H.; Hellweg, T.; von Klitzing, R. *Polymer* 2008, *49*, 749–756.
- [59] Nerapusri, V.; Keddie, J. L.; Vincent, B.; ; Bushnak, I. A. *Langmuir* 2006, *22*, 5036–5041.
- [60] Noskov, S. Y.; Lamoureux, G.; Roux, B. *Journal of Physical Chemistry B* 2005, *109*, 6705–6713.
- [61] Tanaka, F.; Koga, T.; Winnik, F. M. *Progress in Colloid and Polymer Science* 2009, *136*, 1–8.
- [62] Hao, J.; Cheng, H.; Butler, P.; Zhang, L.; Han, C. C. *The Journal of Chemical Physics* 2010, *132*, 154902.
- [63] Saunders, B. R.; Crowther, H. M.; Vincent, B. *Macromolecules* 1997, *30*, 482–487.

- [64] Kiritoshi, Y.; Ishihara, K. *Science and Technology of Advanced Materials* 2003, *4*, 93–98.
- [65] Panayiotou, M.; Garret-Flaudya, F.; Freitag, R. *Polymer* 2004, *45*, 3055–3061.
- [66] Wang, N.; Ru, G.; Wang, L.; Feng, J. *Langmuir* 2009, *25*, 5898–5902.
- [67] Matzelle, T. R.; Geuskens, G.; Kruse, N. *Macromolecules* 2003, *36*, 2926–2931.
- [68] Schmidt, S.; Zeiser, M.; Hellweg, T.; Duschl, C.; Fery, A.; Möhwald, H. *Advanced Functional Materials* 2010, *20*, 3235–3243.
- [69] Schmidt, S.; Hellweg, T.; von Klitzing, R. *Langmuir* 2008, *24*, 12595–12602.
- [70] Burmistrova, A.; Steitz, R.; von Klitzing, R. *ChemPhysChem* 2010, *11*, 3571–3579.
- [71] Zavgorodnya, O.; Serpe, M. J. *Colloid and Polymer Science* 2011, *289*, 591–602.
- [72] Islam, M. R.; Serpe, M. J. *Macromolecules* 2013, *46*, 1599–1606.
- [73] Tagit, O.; Tomczak, N.; Vancso, G. J. *Small* 2008, *4*, 119–126.
- [74] Hu, L.; Serpe, M. J. *Applied Materials and Interfaces* 2013, *5*, 11977–11983.
- [75] Serpe, M. J.; Kim, J.; Lyon, L. A. *Advanced Materials* 2004, *16*, 184–187.
- [76] Sorrell, C. D.; Lyon, L. A. *Langmuir* 2008, *24*, 7216–7222.
- [77] Quint, S. B.; Pacholski, C. *Soft Matter* 2011, *7*, 3735–3738.
- [78] Lyer, A. S. J.; Lyon, L. A. *Angewandte Chemie International Edition* 2009, *48*, 4562–4566.
- [79] Carter, M. C. D.; Sorrell, C. D.; Serpe, M. J. *Journal of Physical Chemistry B* 2011, *115*, 14359–14368.
- [80] Horecha, M.; Senkovskyy, V.; Schneider, K.; Kiriy, A.; Stamm, M. *Colloid and Polymer Science* 2011, *289*, 603–612.

- [81] Tsai, H.-Y.; Vats, K.; Yates, M. Z.; Benoit, D. S. W. *Langmuir* 2013, *29*, 12183–12193.
- [82] Lin, X.; Tang, D.; Yu, Z.; Feng, Q. *Journal of Materials Chemistry B* 2014, *2*, 651–658.
- [83] Binnig, G.; Quate, C. F.; Gerber, C. *Physical Review Letters* 1986, *56*, 930–933.
- [84] Radmacher, M.; Tillmann, R. W.; Fritz, M.; Gaub, H. E. *Science* 1992, *257*, 1900–1905.
- [85] Shimizu, T.; Ohnishi, S.; Kogiso, M. *Angewandte Chemie* 1998, *110*, 3509–3511.
- [86] Gross, L.; Mohn, F.; Moll, N.; Liljeroth, P.; Meyer, G. *Science* 2009, *325*, 1110–1114.
- [87] Weisenhorn, A. L.; Maivald, P.; Butt, H.-J.; Hansma, P. K. *Physical Review B* 1992, *45*, 11226–11232.
- [88] Giessibl, F. J. *Reviews of Modern Physics* 2003, *75*, 949–983.
- [89] Butt, H.-J.; Cappella, B.; Kappl, M. *Surface Science Reports* 2005, *59*, 1–152.
- [90] Üzümlü, C.; Makuska, R.; von Klitzing, R. *Macromolecules* 2012, *45*, 3168–3176.
- [91] A-Hassan, E.; Heinz, W. F.; Antonik, M. D.; D’Costa, N. P.; Nageswaran, S.; Schoenenberger, C.-A.; Hoh, J. H. *Biophysical Journal* 1998, *74*, 1564–1578.
- [92] Domke, J.; Radmacher, M. *Langmuir* 1998, *14*, 3320–3325.
- [93] Andrews, J. W.; Bowen, J.; Cheneler, D. *Soft Matter* 2013, *9*, 5581–5593.
- [94] Dimitriadis, E. K.; Horkay, F.; Maresca, J.; Kachar, B.; Chadwick, R. S. *Biophysical Journal* 2002, *82*, 2798–2810.
- [95] Motschmann, H.; Teppner, R. *Max-Planck-Institut für Grenzflächenforschung, Golm*
- [96] Provencher, S. W. *Makromolekulare Chemie* 1979, *180*, 201–209.

- [97] Lyon, L. A.; Meng, Z.; Singh, N.; Sorrell, C. D.; John, A. S. *Chemical Society Reviews* 2009, 38, 865–874.
- [98] Hoare, T.; Pelton, R. *Langmuir* 2004, 20, 2123–2133.
- [99] Jones, C. D.; Lyon, L. A. *Langmuir* 2003, 19, 4544–4547.
- [100] Sivakumaran, D.; Maitland, D.; Hoare, T. *Biomacromolecules* 2011, 12, 4112–4120.
- [101] Gawlitza, K.; Wu, C.; Georgieva, R.; Ansorge-Schumacher, M.; von Klitzing, R. *Zeitschrift für Physikalische Chemie* 2012, 226, 749–759.
- [102] Gawlitza, K.; Wu, C.; Georgieva, R.; Wang, D.; Ansorge-Schumacher, M. B.; von Klitzing, R. *Physical Chemistry Chemical Physics* 2012, 14, 9594–9600.
- [103] Wellert, S.; Hertle, Y.; Richter, M.; Medebach, M.; Magerl, D.; Wang, W.; Deme, B.; Radulescu, A.; Müller-Buschbaum, P.; Hellweg, T.; von Klitzing, R. *Langmuir* 2014, 30, 7168–7176.
- [104] Richter, M.; Steinhilber, D.; Haag, R.; von Klitzing, R. *Macromol. Rapid Commun.* 2014, accepted.
- [105] Xue, W.; Hamley, I. W. *Polymer* 2002, 43, 3069–3077.
- [106] Fan, K.; Bradley, M.; Vincent, B.; Faul, C. F. J. *Langmuir* 2011, 27, 4362–4370.
- [107] Segal, E.; Perelman, L. A.; Cunin, F.; Renzo, F. D.; Devoisselle, J.-M.; Li, Y. Y.; Sailor, M. J. *Adv. Funct. Mater.* 2007, 17, 1153–1162.
- [108] Krusic, M. K.; Velickovi, S. J.; Griffiths, P. C.; Filipovi, J. *Polym. Int.* 2010, 59, 256–262.
- [109] Fan, K.; Bradley, M.; Vincent, B. *Journal of Colloid and Interface Science* 2012, 368, 287–291.
- [110] Daly, E.; Saunders, B. R. *Physical Chemistry Chemical Physics* 2000, 2, 3187–3193.
- [111] Varga, I.; Gilanyi, T.; Meszaros, R.; Filipcsei, G.; Zrinyi, M. *Journal of Physical Chemistry B* 2001, 105, 9071–9076.

- [112] Zhou, H.; Richter, M.; von Klitzing, R.; Haag, R. *Materials Research Society Symposium Proceedings* 2012, *1403*, 195–200.
- [113] Cheng, H.; Shen, L.; Wu, C. *Macromolecules* 2006, *39*, 2325–2329.
- [114] Chirra, H. D.; Desai, T. A. *Advanced Drug Delivery Reviews* 2012, *64*, 1569–1578.
- [115] Knop, K.; Hoogenboom, R.; Fischer, D.; Schubert, U. S. *Angewandte Chemie International Edition* 2010, *49*, 6288–6308.
- [116] Kojima, H.; Tanaka, F. *Soft Matter* 2012, *8*, 3010–3020.
- [117] Mukae, K.; Sakurai, M.; Sawamura, S.; Makino, K.; Kim, S. W.; Ueda, I.; Shirahama, K. *Journal of Physical Chemistry* 1993, *97*, 737–741.
- [118] Saunders, B. R.; Crowther, H. M.; Morris, G. E.; Mears, S. J.; Cosgrove, T.; Vincent, B. *Colloids and Surfaces A: Physicochemical and Engineering Aspects* 1999, *149*, 57–64.
- [119] Miki, H.; Yagihara, S.; Mukai, S.; Tokita, M. *Progress in Colloid and Polymer Science* 2009, *136*, 101–106.
- [120] Gawlitza, K.; Turner, S. T.; Polzer, F.; Wellert, S.; Karg, M.; Mulvaney, P.; v. Klitzing, R. *Physical Chemistry Chemical Physics* 2013, DOI: 10.1039/C3CP51578H.
- [121] v. Klitzing, R. *Physical Chemistry Chemical Physics* 2006, *8*, 5012–5033.
- [122] Hariri, H. H.; Lehaf, A. M.; Schlenoff, J. B. *Macromolecules* 2012, *45*, 9364–9372.
- [123] Hodge, R. M.; Bastow, T. J.; Edward, G. H.; Simon, G. P.; Hill, A. J. *Macromolecules* 1996, *29*, 8137–8143.
- [124] Blasi, P.; D’Souza, S. S.; Selminc, F.; DeLuca, P. P. *Journal of Controlled Release* 2005, *108*, 1–9.
- [125] Poptoshev, E.; Schoeler, B.; ; Caruso, F. *Langmuir* 2004, *20*, 829–834.
- [126] Purkayastha, D. D.; Madhurima, V. *Journal of Molecular Liquids* 2013, *187*, 54–57.
- [127] Lu, Y.; Drechsler, M. *Langmuir* 2009, *25*, 13100–13105.

- [128] Horigome, K.; Suzuki, D. *Langmuir* 2012, 28, 12962–12970.
- [129] FitzGerald, P. A.; Amalvy, J. I.; Armes, S. P.; Wanless, E. J. *Langmuir* 2008, 24, 10228–10234.
- [130] Iyer, A. S. J.; Lyon, L. A. *Angewandte Chemie International Edition* 2009, 48, 4562–4566.
- [131] Heinz, P.; Bretagnol, F.; Mannelli, I.; Sirghi, L.; Valsesia, A.; Ceccone, G.; Gilliland, D.; Landfester, K.; Rauscher, H.; Rossi, F. *Langmuir* 2008, 24, 6166–6175.
- [132] Banquy, X.; Suarez, F.; Argaw, A.; Rabanel, J.-M.; Grutter, P.; Bouchard, J.-F.; Hildgen, P.; Giasson, S. *Soft Matter* 2009, 5, 3984–3991.
- [133] Kharlampieva, E.; Kozlovskaya, V.; Sukhishvili, S. A. *Advanced Materials* 2009, 21, 3053–3065.
- [134] Wang, J.; Sutti, A.; Wang, X.; Lin, T. *Journal of Colloid and Interface Science* 2012, 369, 231–237.
- [135] Radmacher, M.; Fritz, M.; Hansma, P. K. *Biophysical Journal* 1995, 69, 264–270.
- [136] Schönhoff, M.; Ball, V.; Bausch, A. R.; Dejugnat, C.; Delorme, N.; Glinel, K.; v. Klitzing, R.; Steitz, R. *Colloids and Surfaces A: Physicochemical Engineering Aspects* 2007, 303, 14–29.
- [137] Wong, J. E.; Zastrow, H.; Jaeger, W.; von Klitzing, R. *Langmuir* 2009, 25, 14061–14070.
- [138] Nazaran, P.; Bosio, V.; Jaeger, W.; Anghel, D. F.; v. Klitzing, R. *Journal of Physical Chemistry B* 2007, 111, 8572–8581.
- [139] Lösche, M.; Schmitt, J.; Decher, G.; Bouwman, W. G.; Kjaer, K. *Macromolecules* 1998, 31, 8893–8906.
- [140] Schlenoff, J. B.; Dubas, S. T. *Macromolecules* 2001, 34, 592–598.
- [141] Kellogg, G. J.; Mayes, A. M.; Stockton, W. B.; Ferreira, M.; Rubner, M. F. *Langmuir* 1996, 12, 5109–5113.
- [142] Zeng, Y.; von Klitzing, R. *Langmuir* 2012, 28, 6313–6321.

- [143] Richter, A.; Paschew, G.; Klatt, S.; Lienig, J.; Arndt, K.-F.; Adler, H.-J. P. *Sensors* 2008, 8, 561–581.
- [144] Hu, L.; Serpe, M. J. *Polymers* 2012, 4, 134–149.
- [145] Fernández-Barbero, A.; Suárez, I. J.; Sierra-Martín, B.; Fernández-Nieves, A.; de las Nieves, F. J.; Marquez, M.; Rubio-Retama, J.; López-Cabarcos, E. *Advances in Colloid and Interface Science* 2009, 147-148, 88–108.
- [146] Cuenot, S.; Radji, S.; Alem, H.; Demoustier-Champagne, S.; Jonas, A. M. *Small* 2012, 8, 2978–2985.
- [147] Matsumura, Y.; Iwai, K. *Polymer* 2005, 46, 10027–10034.
- [148] Kleinen, J.; Richtering, W. *Macromolecules* 2008, 41, 1785–1790.
- [149] Karg, M.; Pastoriza-Santos, I.; Prez-Juste, J.; Hellweg, T.; Liz-Marzan, L. M. *Small* 2007, 3, 1222–1229.
- [150] Govorova, A. O.; Richardson, H. H. *Nano Today* 2007, 2, 30–38.
- [151] Satarkar, N. S.; Biswal, D.; Hilt, J. Z. *Soft Matter* 2010, 6, 2364–2371.
- [152] Richter, M.; Zakrevskyy, Y.; Eisele, M.; Lomadze, N.; Santer, S.; v. Klitzing, R. *Polymer* 2014, accepted.
- [153] Dalmont, H.; Pinprayoon, O.; Saunders, B. R. *Langmuir* 2008, 24, 2834–2840.
- [154] Johansson, C.; Gernandt, J.; Bradley, M.; Vincent, B.; Hansson, P. *Journal of Colloid and Interface Science* 2010, 347, 241–251.
- [155] Oh, J. K.; Drumrighta, R.; Siegwartb, D. J.; Matyjaszewski, K. *Progress Polymer Science* 2008, 33, 448–477.
- [156] Haag, R.; Kratz, F. *Angewandte Chemie International Edition* 2006, 45, 1198–1215.
- [157] Sisson, A. L.; Steinhilber, D.; Rossow, T.; Welker, P.; Licha, K.; Haag, R. *Angewandte Chemie International Edition* 2009, 48, 7540–7545.
- [158] Vermonden, T.; Censi, R.; Hennink, W. E. *Chemical Reviews* 2012, 112, 2853–2888.

- [159] Censia, R.; Martino, P. D.; Vermonden, T.; Hennink, W. E. *Journal of Controlled Release* 2012, *161*, 680–692.
- [160] Uhrich, K. E.; Cannizzaro, S. M.; Langer, R. S.; Shakesheff, K. M. *Chemical Reviews* 1999, *99*, 3181–3198.
- [161] Kabanov, A. V.; Vinogradov, S. V. *Angewandte Chemie International Edition* 2009, *48*, 5418–5429.
- [162] Steinhilber, D.; Sisson, A. L.; Mangoldt, D.; Welker, P.; Licha, K.; Haag, R. *Advanced Functional Materials* 2010, *20*, 4133–4138.
- [163] Tomalia, D. A. *Progress in Polymer Science* 2005, *30*, 294–324.
- [164] Paramonov, S. E.; Bachelder, E. M.; Beaudette, T. T.; Standley, S. M.; Lee, C. C.; Dashe, J.; Fréchet, J. M. J. *Bioconjugate Chemistry* 2008, *19*, 911–919.
- [165] Zhang, J.; Jia, Y.; Li, X.; Hu, Y.; Li, X. *Advanced Materials* 2011, *23*, 3035–3040.
- [166] Shenoi, R. A.; Lai, B. F. L.; Kizhakkedathu, J. N. *Biomacromolecules* 2012, *13*, 3018–3030.
- [167] Yuan, Y.-Y.; Du, J.-Z.; Song, W.-J.; Wang, F.; Yang, X.-Z.; Xiong, M.-H.; Wang, J. *Journal of Materials Chemistry* 2012, *22*, 9322–9329.
- [168] Fleige, E.; Quadir, M. A.; Haag, R. *Advanced Drug Delivery Reviews* 2012, *64*, 866–884.
- [169] Sasportas, L. S.; Kasmieh, R.; Wakimoto, H.; Hingtgen, S.; van de Water, J. A. J. M.; Mohapatra, G.; Figueiredo, J. L.; Martuza, R. L.; Weissleder, R.; Shah, K. *Proceedings of the National Academy Sciences* 2009, *106*, 4822–4827.
- [170] Kauer, T.; Figueiredo, J. J.; Hingtgen, S.; Shah, K. *Nature Neuroscience* 2012, *15*, 197–204.
- [171] South, A. B.; Lyon, L. A. *Chemistry of Materials* 2010, *22*, 3300–3306.
- [172] Kainthan, R. K.; Muliawan, E. B.; Hatzikiriakos, S. G.; Brooks, D. E. *Macromolecules* 2006, *39*, 7708–7717.